ENGINEERING APPROACHES FOR NEUROBIOLOGY

by

Richard Martin Stoner

BS in Bioengineering,

University of Pittsburgh, 2005

Submitted to the Graduate Faculty of

the Swanson School of Engineering in partial fulfillment

of the requirements for the degree of

Doctor of Philosophy

University of Pittsburgh

2010

UNIVERSITY OF PITTSBURGH

SWANSON SCHOOL OF ENGINEERING

This dissertation was presented

by

Richard Martin Stoner

It was defended on

December 3rd, 2009

and approved by

Henry Zeringue, Assistant Professor,

Department of Bioengineering, Swanson School of Engineering, University of Pittsburgh

Aaron Batista, Assistant Professor,

Department of Bioengineering, Swanson School of Engineering, University of Pittsburgh

Marina Kameneva, Professor,

Department of Bioengineering, Swanson School of Engineering, University of Pittsburgh

Phillip J. Leduc, Associate Professor,

Department of Mechanical Engineering, Carnegie Mellon University

Dissertation Director: Henry Zeringue, Assistant Professor,

Department of Bioengineering, Swanson School of Engineering, University of Pittsburgh

ENGINEERING APPROACHES FOR NEUROBIOLOGY

Richard Martin Stoner, PhD

University of Pittsburgh, 2010

Neurobiological systems span a wide dimensional range. I will present three examples of scale-driven methodological development in biological systems to demonstrate the utility of applied engineering approaches for neurobiological applications and provide direction for future study. Concepts in computational modeling, microfluidic cell culture platforms, and MRI phantoms are examined - from the scale of a single synapse to long distance cortical connections.

A single synapse model was developed using a Monte Carlo simulation environment to study biophysically realistic mechanisms of spike timing dependent plasticity (STDP). A deterministic model of spatiotemporal intracellular calcium detection was extended to include subunit-specific receptor kinetics. Using STDP-based stimulus protocols, global and local molecular time courses were then produced for NR2A and NR2B knockout models.

To study network-level oscillatory activity, a model of spatially-constrained networks was created based on cyclic geometry to look at the effects of circumference and track-width on spontaneous network activity. Transverse wave activity was demonstrated and characterization methods were established based around wave velocity and origin.

Microfluidic technology provides an experimental means to study network organization and activity *in vitro*. I will present work towards an integrated microfluidic control platform combining multiple design strategies to address the intrinsic spatiotemporal resolution of neurons. Microfluidic devices fabricated using multilayer soft-lithography with internal valves to direct multiple laminar fluid flows were controlled with a dynamic pressure platform to create targeted hydrodynamic streams. Devices were characterized for arbitrary profile generation, repeatability, flow rate stability, and lid-driven flow using multimodal sensory feedback and analysis.

Finally, I will present a microfluidic application for cortical connectivity measures. A microfluidic phantom for diffusion-weighted magnetic resonance imaging was developed for validation studies of long-distance cortical white matter connections. The diffusion phantom provides a reliable physical structure with which high-resolution fiber tractography algorithms can be tested against. The diffusion phantom was fabricated using conventional photolithographic techniques with an internal channel network that mimics white matter fiber tracts and crossings. I show preliminary mapped tracts to the features inside of the phantom via post-processing of diffusion-weighted images.

TABLE OF CONTENTS

LIST OF FIGURES

PREFACE

I would like to acknowledge my friends for keeping me sane, my family for keeping me motivated, my lab mates for providing an intellectual challenge, my advisor Henry Zeringue for creating a rich environment to grow academically, Jonathan Rubin for mathematical guidance, my committee members for constructive criticism, and my colleagues within the Department of Bioengineering and the Center for the Neural Basis for Cognition at the University of Pittsburgh and Carnegie Mellon for sharing their passion for neuroscience and intellectual curiosities over the past five years. It was fun.

1.0 INTRODUCTION

I will describe three current applications in bioengineering directed toward the understanding of neurobiological systems. From cortex-wide systems of connectivity to the molecular interactions at a single synapse, the reach of neurobiology covers many levels of detail. Proper understanding of defining phenomena at each level of scale is necessary to design effective experimental approaches.

1.1 SCALE IN MODELING

Synaptic plasticity is an excellent example to demonstrate the interaction between phenomena across different levels of scale. Synaptic plasticity refers to the continuous adjustment of synaptic transmission efficiency dependent upon upon multiple spatial and temporal input parameters. Bidirectional modulation of synaptic strength occurs through changes in both pre-synaptic (transmitting) and post-synaptic (receiving) regions of a single synapse. When a pair of neurons are stimulated using a series of high-frequency pulses (10Hz), synapses between the pair will increase in physical size and receptor count, resulting in an increase in the magnitude of the response to any subsequent stimuli. A low frequency (1 Hz) pulse will produce the opposite effect. The biophysical mechanisms responsible for this modulation manifest over time at each synapse through a complex series of molecular interactions involving voltaged-gated ion channels, ligand-gated receptors, and intracellular signaling mechanisms. These systems operate within a physiological balance that provides robust signal transmission with constant modulation of the signal strength.

By stepping out of the molecular context it becomes clear that while synaptic function is furnished by a large set of components, the outcome can be approximated with a state-based model that is only concerned with mapping significant inputs to their output. This approximation is known to as a "black box" model, wherein the inputs and outputs of a system are known, but little to no understanding of the underlying operations is utilized. Black box models focus on defining the map between input-output relationships exclusively, bypassing any biological or physical constraints that may be present within the system itself. As a result, such models have the potential to greatly reduce the degree of model complexity found in most biological systems. This enables researchers to generate useful simulated data from models that are computationally tractable. To maximize the utility of black box models, one must identify significant inputs and non-trivial outputs from the larger set of available variables

before any reduction is made. Too many inputs will increase the computational load and can result in over-defined relationships.

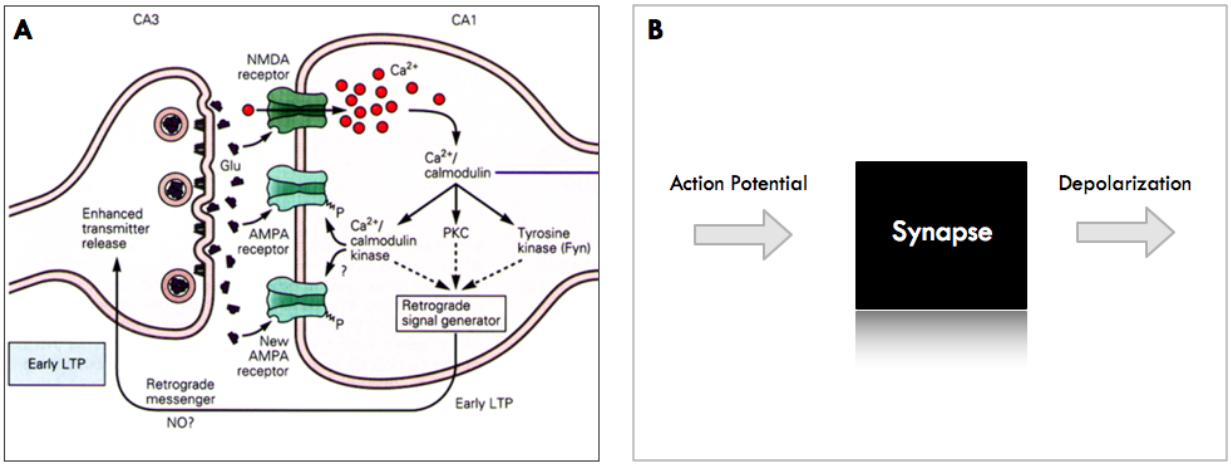

Figure 1.1: **Models of synaptic plasticity.** A) Schematic representation of the molecular pathways responsible for changing synaptic weights. Signaling through intracellular calcium concentrations and binding molecules is translated into a series of physiological changes, including greater receptor density, a more organized postsynaptic density, and increased spine volume. (Modified from Kandel, 2000 [49]) B) A black box model of synaptic plasticity. Here the precise mechanisms responsible for changing synaptic weights are masked from any further implementation. No additional information is necessary so long as a complete mapping exists between input and output. Such mapping may take the form of a look-up table or a formal mathematical description.

The black box model definition covers both time-independent and time-varying systems. The models of linear time-invariant systems are well described and provides a pre-existing formal toolbox for researchers to define input-output relationships from. Extending to time-varying systems requires the use of more involved analysis techniques that address a range of possible solutions. Dynamical systems approaches using analytical or numerical solutions for a set of differential equations may be used are commonly used for such systems. These internal descriptions imbue a state-based memory to the black box model, producing valuable, deterministic responses.

Returning to the example of synaptic plasticity, inputs to the synapse model would take the form of arriving action potentials, with model outputs defined by the magnitude of the evoked postsynaptic current. Synaptic plasticity in this context becomes an abstracted variable, synaptic weight, maintained within the black box that codes for the magnitude of the output response for each input received. Understanding how the synaptic black box adjusts the weight variable according to various spatial and temporal inputs is still an active area of research and is revisited in Chapter 2 with spike timing dependent plasticity (STDP).

The application of scale-dependent analysis and appropriate model selection persists throughout this thesis and becomes the overarching theme as explored across three different neurobiological areas: synapses, networks, and long-distance white matter connections.

1.2 SCOPE

The scope of this thesis is broad due to the diversity of projects pursued during my time spent in neural engineering. The topics are organized in a bottom-up perspective starting with the atomic component of a nervous system, the synapse. Through fate or fortune, this approach enabled for efficient self-organization of the topics to be covered into three categorial fields within neural engineering: Computational simulations, microfluidic cell culture devices, and magnetic resonance imaging. Coverage of each topic is selective and serves as an starting point to address future scientific questions in neurobiology with applied engineering concepts.

To begin, I will focus on one of the smallest domains of nervous system function: excitatory synaptic transmission and plasticity. Characteristic dimensions underlying these phenomena exist at nanometer length scales and microsecond time periods, principally determined by passive molecular diffusion coefficients and reaction kinetics. At this scale, I will describe a form of synaptic plasticity referred to as spike-timing dependent plasticity (STDP) that is mediated by the relative timing between neurotransmitter release and dendritic depolarization. A computational model was developed using a Monte Carlo reaction-diffusion simulation environment (MCell) to describe in detail the molecular signaling pathways responsible for reconciling complex activation patterns observed in previously published experimental data.

I will jump over single-neuron simulations and look at local network models of neural activity. Local network models are neural networks populated with typically tens to hundreds of neurons with, at the most basic representation, a connectivity map describing synaptic relationships between each neuron. At this level of detail the overall activity of the neuronal ensemble is more important than an individual neuron's physiology.

Extending these approximations up to a single neuron level of analysis, it is possible to define relatively complex neurophysiology with a pair of solvable differential equations. Different neuron classes, categorized by their activity, are represented by non-physiological model coefficients. From these steps, investment in single neuron function is minimized to better explore how neuron-neuron connectivity and spatial distribution affects small-scale neural activities such as burst initiation and wave propagation velocities. I will describe a computational model that was developed to evaluate potential relationships between spatial dimensions of a physical network and quantitative measures of neural activity within.

Remaining at the network level of analysis, I will describe the development of a microfluidic platform for creating small networks with definable spatial parameters. Rather than use experimental values from literature to develop a computational model of behavior, I will describe concepts of using known chemotaxic responses to diffusible and membrane-bound ligands in order to direct cell growth and neurite guidance. Guidance pathways via molecular signaling cues in neurons are highly regulated during development by precisely-timed presentations of specific cues to produce the organized cortical maps found in an adult animal. Developing the technology to take advantage of these pre-existing pathways will enable future forward-engineering approaches.

The motivation to create and define in-vitro small-scale neuronal networks should be intuitive. With a known connectivity map, it is possible to validate computational models developed to understand the basic modes of

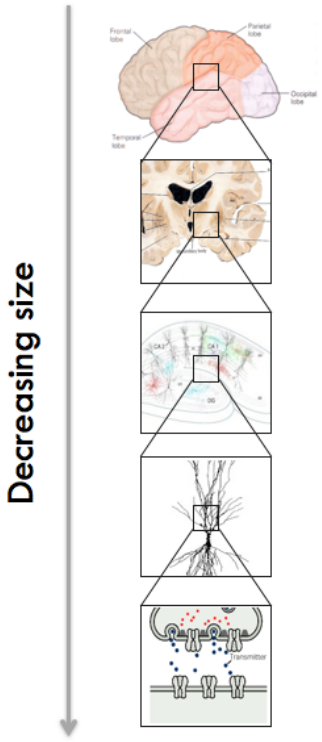

Cortex	**10^{-1} m - 10^{-2} m**
Functional Anatomy	**10^{-2} m - 10^{-3} m**
Local Networks	**10^{-3} m - 10^{-4} m**
Neuron Physiology	**10^{-4} m - 10^{-6} m**
Synaptic Function	**10^{-6} m - 10^{-9} m**

Figure 1.2: **Multiscale approaches in neurobiology.** The hierarchical organization of the nervous system spans across a broad dimensional range. Biological phenomena unique to the nervous system are found at the nanometer scale in single-molecule kinetics, protein folding, and ligand-receptor interactions. Speculation has been made with regard to phenomena below his scale, including quantum effects within microtubules [85], but the bulk of neuroscience is bounded at the resolution of a single molecule. Synaptic transmission and associated neurophysiology are the product of well-connected and temporally-concerted single molecule interactions. Neuron function is the sum of synaptic and cellular physiology. Local network activity is the result of individual neuron processing placed into a spatial context with defined connectivity maps and physical locations. Collections of local networks produce areas of the brain that carry out specific cognitive tasks, delineated functionally. Finally, different functional areas are linked via global white matter connections to produce the behaviors that most of us take for granted. Means of transmission, synchronization, and plasticity can be found in within each scale. (Modified from Kandel, 2000 [49])

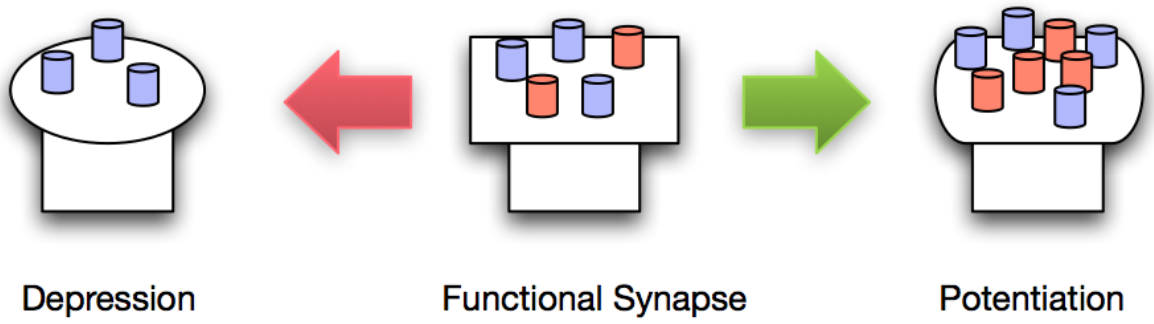

Figure 1.3: **Synaptic plasticity.** Bidirectional modification of synaptic weights occurs by mediating the rates of receptor insertion and removal via input-specific pathways. Potentiation on a first-order approximation consists of an increase in receptor number and overall spine size while depression results in a net loss of receptors and reduction in spine size.

activity found within small groups of neurons. The ability to study multi-synaptic integration, multi-neuron oscillation, and changes in synaptic plasticity will greatly increase should such a system exist. However, as Chapter 3 will show, the creation of a capable system able to control a cell culture environment with sufficient precision without impending neuronal growth is a difficult task. The need for precision and neural compatibility for such a system will take us into the development of microfluidic devices for cell culture applications. Relying on predictable flow phenomena and governing equations, I have designed a complete microfluidic platform including control software and hardware to begin down the long road of controlled production of arbitrary neural networks in-vitro. System characterization was performed on the platform using general performance metrics to demonstrate the capabilities of a dynamic pressure system for chemical stimulus creation.

The last level of analysis covered is that of cortex-wide white matter connections between hemispheres and distinct functional areas. These connections, often referred to as the circuitry or cables of the brain, act primarily to transmit neural information from one processing region to another. Complete maps of connectivity in the brain, often referred to as a connectome, are being developed using a non-invasive magnetic resonance imaging modality referred to as diffusion-weighted imaging (DWI). Diffusion weighted imaging relies upon the preferred diffusion direction of water molecules along and within myelin sheaths, the insulation of the cables, to identify principal fiber directions. Recent advances in the types of post-processing algorithms available and ever improving MRI technology have greatly increased the ability to resolve small fibers with multiple intersections.

Diffusion-weighted imaging is a non-invasive imaging modality with identified features that are implicitly inferred rather than explicitly defined. Therefore, a strong degree of confidence is placed in the post-processing techniques that they will produce actual fibers and crossings rather than artifacts. Evaluation of different tracking techniques is performed against micro-dissection results and MRI phantoms - physical structures with known

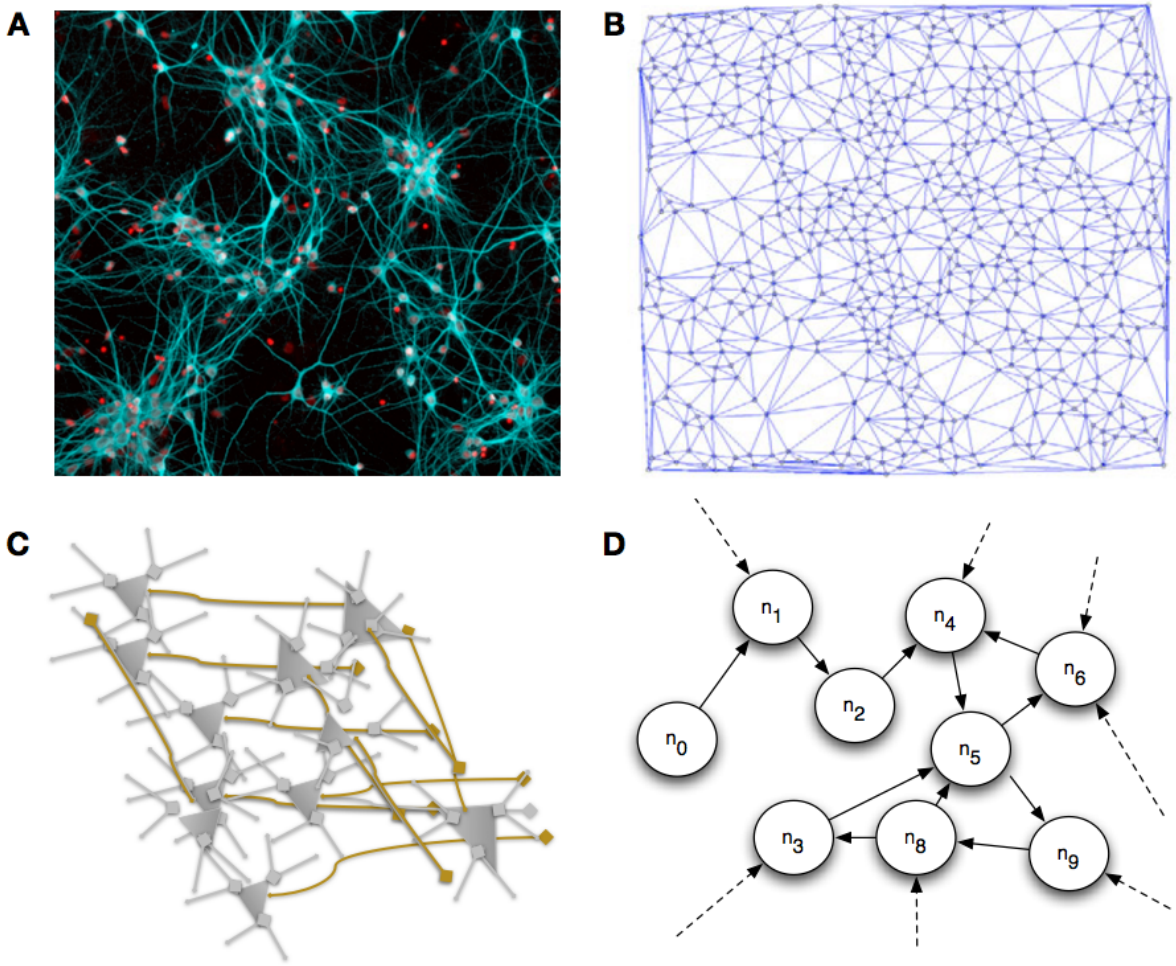

Figure 1.4: **Creating realistic neural network models.** The complexity of signaling in small networks is great due to the high levels of interconnectivity and heterogeneity of cell types. Many-to-many connectivity produces a large number of modal responses, reminiscent of a black box model with state-based memory, making proper characterization difficult and mathematically intensive. Computer models that simplify across a single neuron model provide a tractable approach toward characterizing the types of activity found in these small networks. Previous work has shown the benefit of these models for elucidating potential mechanisms that underly these behaviors [106, 107] A) False-color fluorescent image of dissociated neurons in culture. (Image provided by A. Vishwanathan, University of Pittsburgh, 2009) B) Connectivity map produced by manual tracing [107]. C) Single neuron model representation containing first-order approximations of cell morphology. D) Node-based model from connectivity data.

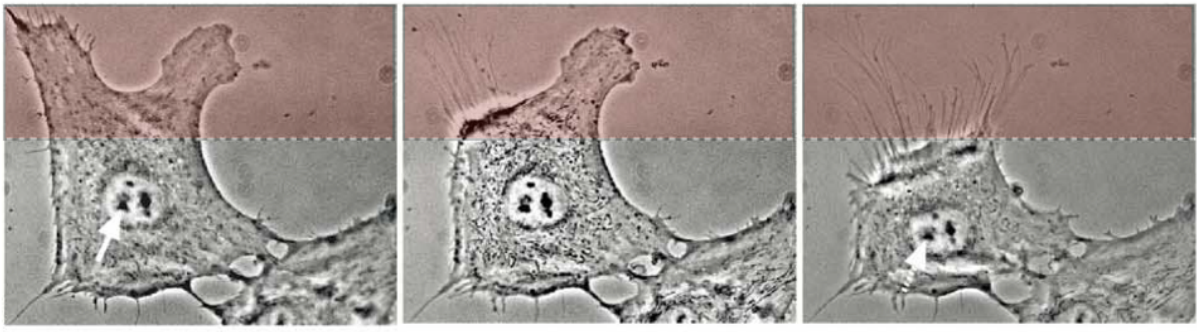

Figure 1.5: **Microfluidic cell culture.** Using micrometer-scale features and experimental cues, microfluidic cell culture devices are capable of producing environments and perturbations with greater precision than conventional *in vitro* methods. Focused exposure to trypsin, as pictured above, will cause the targeted region of the cell to disconnect from the culture surface. [97]

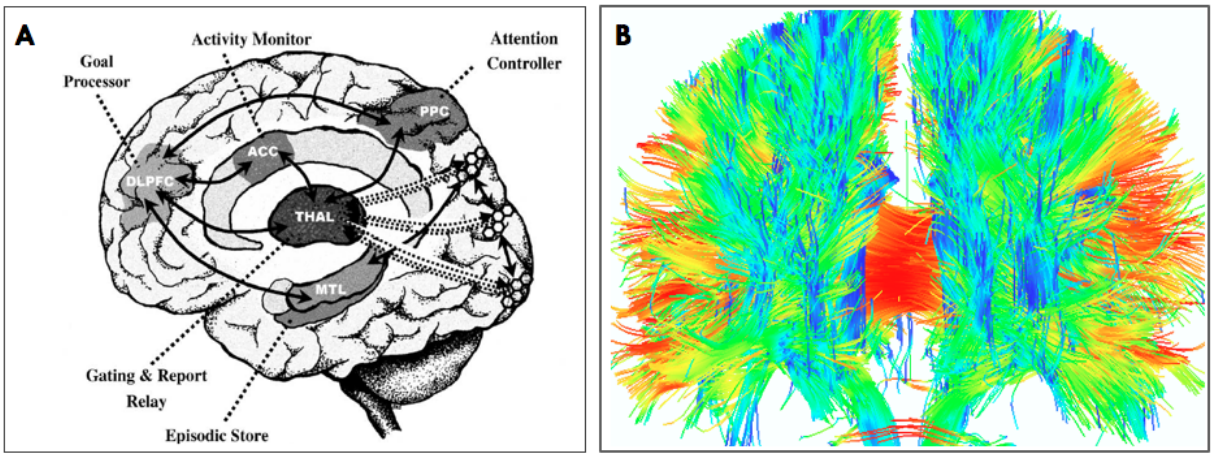

Figure 1.6: **Mapping cortical connections.** Cognition results from the organized activity of many functionally distinct regions of the brain. White matter acts as conduit for information transmission from one region to another. Modern MRI methods can be used to map white matter tracts, producing a large scale map of cortical connectivity referred to as a connectome. (Images provided by W. Schneider, University of Pittsburgh, 2009)

features that are then scanned and processed. While phantoms exist for large-scale DWI measures, the increased resolution capable of the new techniques requires a smaller, more complex phantom able to recreate arbitrary micrometer-scale structures analogous to the physical tracts found in the brain. Using the fabrication techniques initially described for microfluidic cell culture applications, I will describe a microchannel phantom to with sufficient resolution to validate modern high resolution post-processing techniques.

2.0 COMPUTATIONAL MODELS OF NEURAL ACTIVITY

Computational models of biological systems have enabled researchers to ask questions beyond the scope of conventional bench-based experimental approaches. Neurosciences, in particular, have integrated computational models of biological function into standard experimental workflows with great success. Models are used to study mechanisms underlying normal physiological systems as well as the flow of information within.

The approaches presented here focus on the basic concept of identifying the minimal feature of a model to properly describe the neural activity of interest. The first topic, spike timing dependent plasticity (STDP), is a synaptic-scale phenomenal event that expands the Hebbian theory of "Fire together, wire together" by introducing a precise temporal regulator of plasticity [38]. The second topic covers spontaneous neural activity within a small network and the effect that spatial constraints on the character of the activity itself.

2.1 SPATIOTEMPORAL CALCIUM SIGNALING IN STDP

2.1.1 Biological basis of synaptic plasticity

Synaptic plasticity refers to the change in strength between the connections through which neurons communicate. Long-term changes through synaptic plasticity are thought to be the basis for learning and memory [61]. Many of the basic components underlying the molecular and structural changes that occur within a single synapse have been identified and characterized [68]. Models built from a subset of the components available have been created to reconcile *in vitro* experimental results with observed changes found in electrophysiology, protein localization, and long-term regulation of protein expression [68].

The canonical forms of stable synaptic plasticity, known as long-term potentiation (LTP) and long-term depression(LTD) [12], were first described by Bliss and Lomo [13]. The early work demonstrated changes in plasticity as a function of different input firing rates. High frequency pulse trains yielded potentiation while low frequency pulse trains resulted in depression of the synapse. Potentiation and depression in this context were used describe the amount of inward current produced following neurotransmitter release on the presynaptic side of the synapse. Over the past 40 years, the study of synaptic plasticity has grown to include almost every model system available, including work with humans [12].

One key discovery that shaped the current understanding of synaptic plasticity was the formation of a link between the levels of intracellular calcium within a synapse and the resultant change in synaptic weight. This result was not completely unexpected as intracellular calcium was known to play an important role in many cell signaling processes, including but not limited to cardiac and somatic muscle contraction, apoptosis, vesicle exocytosis, and various G-protein mediated pathways (http://www.genome.jp/kegg/). The utility of using calcium as a robust messenger originates from an extremely low basal concentration 800 nM in cytoplasm. A small increase in number of free calcium ions within the small volume of a single synapse corresponds to a many-fold increase in the intracellular concentration. The presence of multiple calcium-binding proteins ensures that the downstream effects occur rapidly.

The first descriptions of intracellular calcium as the primary biophysical mechanism for the detection and implementation of the input-based changes were presented by Lisman et. al. [61]. Early results demonstrated a clear link between the levels of intracellular calcium on the post-synapse and the subsequent change in efficacy. High levels of intracellular [Ca^{++}] were correlated with an increase in the invoked post-synaptic current (PSC) while lower intracellular [Ca^{++}] levels yielded a decrease in PSCs. It would be later demonstrated how short term changes mediated by intracellular calcium could initiate a kinase-mediated molecular cascade producing the stable LTP and LTD seen experimentally [68]. Variations around this model would persist and become known as the calcium control hypothesis [62, 93]. As experimental techniques advanced, new and interesting phenomena were uncovered that forced a review of the existing models.

2.1.2 Spike timing dependent plasticity

Using multi-patch clamp experiments to induce plasticity, a time-dependent component of plasticity was first observed by Markram et. al. [69]. Markam observed with a paired-pulse stimulation protocol that the sign and magnitude of the plasticity change could be adjusted by controlling the relative arrival time between pre-synaptic neurotransmitter release and post-synaptic membrane depolarization. This phenomena was better characterized in the work by Bi & Poo that mapped these changes across the full range of relative arrival times to produce the characteristic response curve seen in Figure 2.1[10]. When pre-synaptic release occurred prior to post-synaptic depolarization, potentiation occurred at the synapse. Depression was seen when this timing was reversed, with the pre-synaptic release occurring after the post-synaptic depolarization.

The initial paired pulsed experiments that evaluated STDP across different time windows were found to agree with the peak calcium hypothesis. When biologically-relevant stimuli were introduced, the predictions from the calcium control hypothesis failed to predict the changes observed. From triplet protocols using combinations of pre-post-pre and post-pre-post patterns of activation it became clear that the mechanisms responsible for STDP-based modifications detected more than just peak intracellular calcium within the post-synapse (Figure 2.1D).

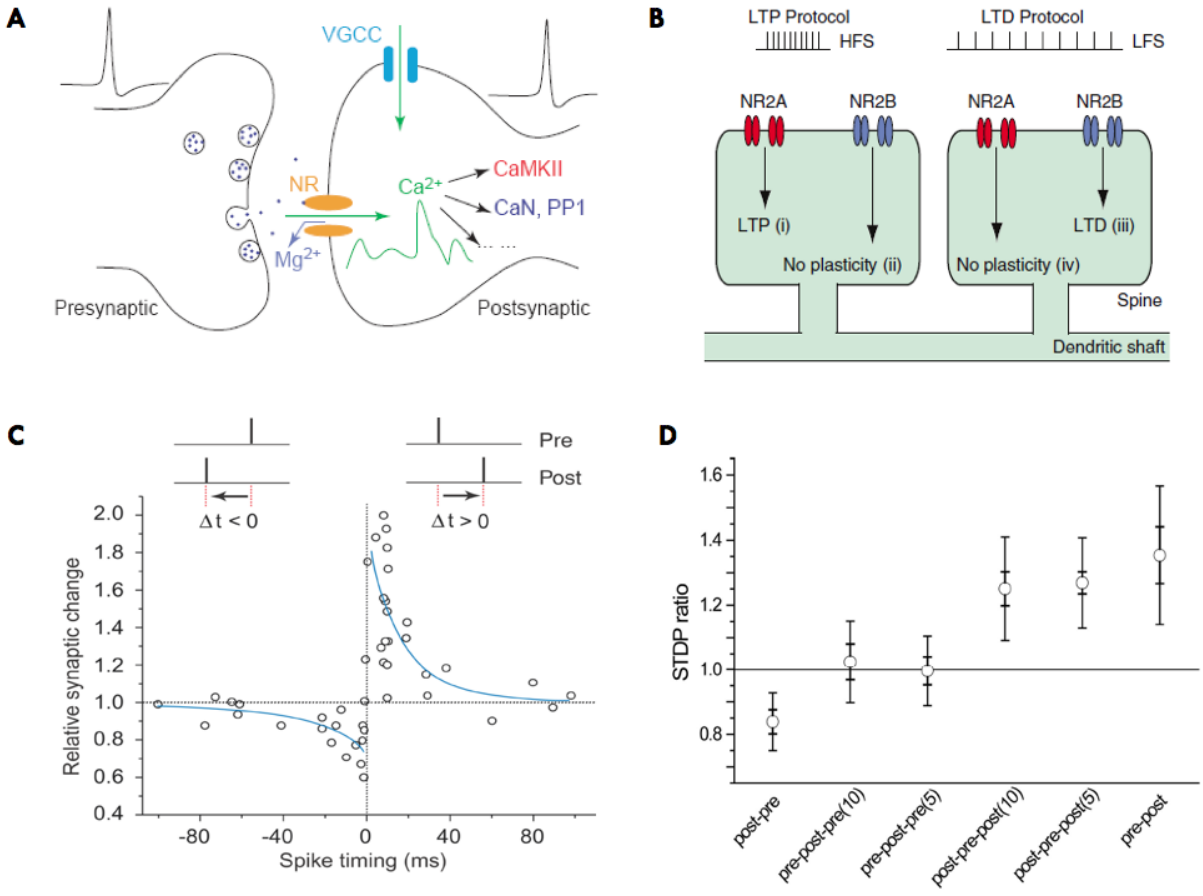

Figure 2.1: **Overview of calcium-mediated synaptic plasticity.** A) Calcium mediated synaptic plasticity is found both pre- and post-synaptically. In the presynapse, calcium-mediated pathways govern synaptic vesicle release thresholds and pool size. In the postsynapse, calcium-mediated pathways govern the activation of downstream kinases such and phosphotases such as CaMKII and PP1, respectively (Modified from Rubin 2005 [88]). B) Canonical forms of plasticity (LTP and LTD) and the postsynaptic receptors thought to facilitate the specific induction (Modified from Naoki 2005 [76]). C) Timing window for STDP. Post-pre timing results in depression while pre-post timing produces potentiation. A sharp transition between potentiation and depression is observed at the 0 ms offset. D) Triplet results from STDP unreconcilable with the calcium control hypothesis.

2.2 BIOPHYSICAL MODELS OF STDP

A variety of past computational works have simulated temporal dynamics of postsynaptic calcium signals and signal detection associated with spike timing dependent plasticity (STDP). We will present a single synapse model that we developed using the MCell simulation environment and applied to study spatiotemporal calcium signaling through biophysically realistic mechanisms relevant to STDP. This model represents a major extension of an earlier differential equation model to include spatial and stochastic effects as well as subunit-specific NMDA receptor kinetics and distributions. Using stimuli based on experimental STDP protocols global and local molecular time courses were compared across normal and NR2A or NR2B knockout models. First we present a brief review some recent experimental results, including NMDA subunit-specific findings, that point to the importance of including spatial effects and stochasticity in such computational models.

In many settings, synaptic inputs lead to the appearance of calcium signals in a postsynaptic neuron. In 2002, a thorough and well-reasoned review article by Franks and Sejnowski, entitled "Complexity of calcium signaling in synaptic spines", appeared in *BioEssays* [28]. In that work, the authors summarized a biophysical rationale for the idea that qualitatively different calcium time courses lead to long-term potentiation (LTP) or long-term depression (LTD) of synapses and described experimental findings supporting this idea. Furthermore, they presented results suggesting that calcium signals induced by plasticity-evoking events are not spatially uniform, with important implications for plasticity. Specifically, experiments had shown that signaling related to plasticity can be driven by calcium dynamics within spatially localized regions, in ways that must depend on the spatial organization of molecules involved in the relevant pathways. Finally, the authors described Monte Carlo simulation methods and presented illuminating results from their own simulations, showing calcium time courses and resulting calmodulin (CaM) activation induced by back-propagating action potentials or by an excitatory postsynaptic potential, which they referred to as initial steps toward a biologically comprehensive simulation of spatiotemporal postsynaptic signaling associated with plasticity.

Since the publication of that article, experimental developments have provided new support for the existence of separate LTP and LTD signaling pathways, or modules, and new details about elements that participate in determining plasticity outcomes. Together with recent spatiotemporal simulation results, these findings have further strengthened the case that spatial aspects of signaling play critical roles in shaping synaptic plasticity outcomes. In this paper, we review some of these developments, with a focus on N-methyl-D-aspartate receptor (NMDAR) subtypes and spike timing-dependent plasticity (STDP) outcomes. Subsequently, we present practical details relating to our own use of a particular, convenient framework for simulating spatiotemporal dynamics of molecules in a postsynaptic density, similar to that used recently in the context of synaptic plasticity by Franks, Sejnowski, and a few other research groups, with the aim of making this resource more accessible to the research community.

2.2.1 Spatial specificity

A temporal pattern of presynaptic neurotransmitter release and postsynaptic spiking will lead to a postsynaptic calcium signal. Based on distributions of calcium sources, including synaptic channels and voltage-gated calcium channels, in and near the postsynaptic density (PSD), this signal will likely have a particular time course at each spatial location within the postsynaptic density and in other parts of the postsynaptic neuron. Moreover, concentrations of particular molecules within the postsynaptic neuron, including those which respond to changes in calcium, have their own spatial profiles, such that calcium entering the neuron at different locations has access to different signaling agents[66, 31, 28, 47, 79, 86, 45]. This chain of reasoning leads us to conclude that spatial aspects of postsynaptic signals are likely to be critical for synaptic plasticity outcomes, and a thorough mechanistic understanding of synaptic plasticity must take into account this spatial specificity.

Many of the recent developments in characterizing spatial specificity of postsynaptic signaling have related to NMDARs, which are critical for LTP and LTD [11, 5]. NMDARs consist of assemblies of subunits. Experiments focusing on hippocampal CA1 synapses examined how NMDARs including NR2A or NR2B subunits contribute to synaptic plasticity, and a striking difference in their roles was observed. Specifically, in slice experiments, blockade of NR2B-containing NMDARs eliminated LTD but not LTP, while inhibition of NMDARs with the NR2A subunit cancelled LTP but left LTD intact [64]. Similar roles for NR2A- and NR2B-containing NMDARs were found in adult perirhinal cortex slices [70]. In *ex vivo* hippocampal STDP experiments, the level of pre-post LTP correlated with the prevalence of NR2A subunits. The presence of NR2B subunits was not required for this LTP but was for post-pre LTD, which did not depend on NR2A [88]. Furthermore, pre-post LTP was eliminated, but not replaced by LTD, under a pharmacological CaMKII blockade. Similarly, LTD post-pre pairings no longer produced LTD in the presence of calcineurin (CaN) blockers, yet LTP did not result [110]. The simplest hypothesis that unifies these results is that NMDARs with NR2A subunits preferentially activate a kinase-dependent pathway that induces LTP, while NMDARs including NR2B subunits promote a phosphatase-dependent pathway that leads to LTD.

In the time since the original results of Liu et al. [64] and Massey et al. [70] on the roles of NMDAR subtypes in long-term synaptic plasticity emerged, additional studies have complicated the story, linking each subtype to both LTP and LTD under various conditions, as nicely summarized elsewhere [91]. What this complexity indicates is that a more detailed knowledge of the signaling effects induced by NMDARs with particular subunit compositions will be needed to elucidate their roles in synaptic plasticity. The natural first question in this vein of investigation is, how could different NMDAR subtypes activate different signaling pathways? One possibility is that specific NMDAR subtypes may activate particular signaling pathways, leading to associated plasticity outcomes, by shaping calcium signals. It has been established that an NMDAR's subunit type determines its kinetics and the kinetics of the currents it supports, with major differences arising between NR2A- and NR2B-containing NMDARs [24]. These differences cause very different calcium current time courses to result from different plasticity induction protocols [24]. Alternatively, while temporally distinct calcium signals could induce different effects on other molecules involved in synaptic plasticity, it is also likely that NMDARs containing different subunit types are themselves distributed differently in space, in different spatial relationships with relevant signaling agents [98, 94];

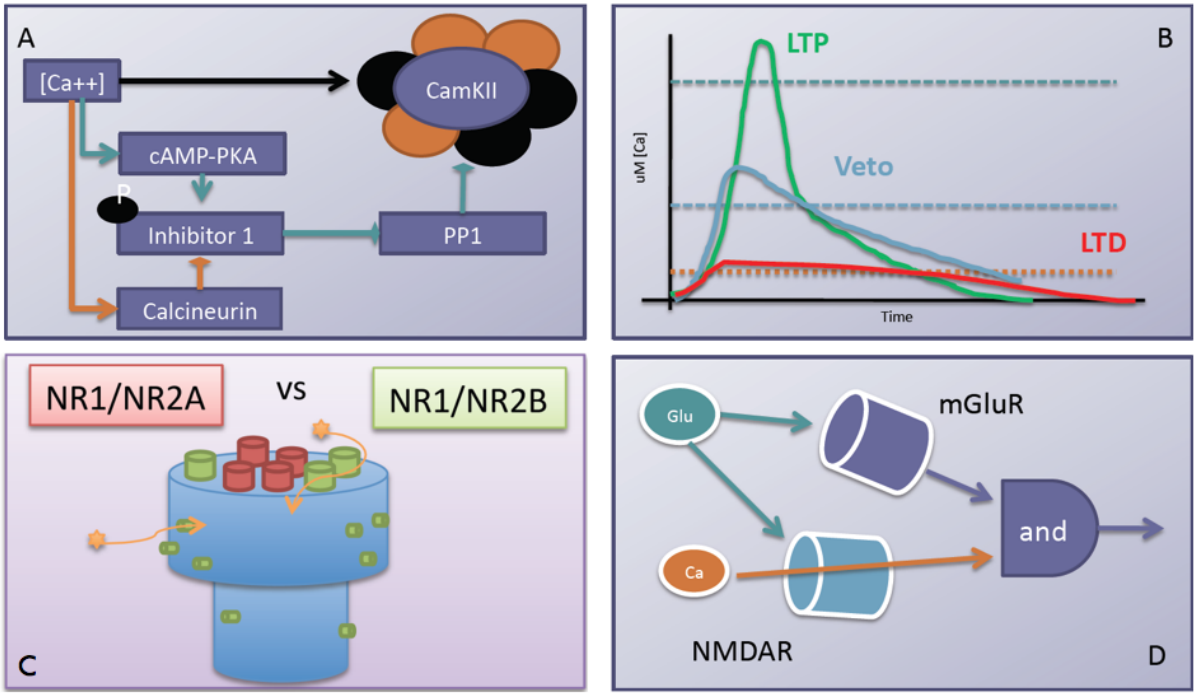

Figure 2.2: **Biophysical models of STDP.** Present theories consider many of the components present at and around the post-synaptic density: the precise molecular kinetics of CaMKII [34], the temporal time course of calcium [88], NMDAR subunit distribution [33], and the presence of multiple calcium coincidence detectors [77]. While many of the proposed concepts describe overlapping systems at the post synapse, there is still uncertainty due to the assumptions of the models employed.

certainly, experiments show that extrasynaptic NMDARs activate different signaling pathways than do synaptic NMDARs [45]. Thus, even similar calcium signals delivered through different types of NMDARs could induce different plasticity outcomes by activating different downstream events.

2.2.2 Recent simulations of spatiotemporal postsynaptic signaling in long-term plasticity

Experiments have established the centrality of calcium, NMDARs and their subtypes, and particular postsynaptic molecules in the pathway from pre- and postsynaptic spiking to synaptic plasticity. The knowledge in this area has advanced to the point where computational modeling can be most useful: enough details are known to constrain simulations, yet enough questions remain to warrant intense investigation. It is not a coincidence that there has been a recent surge in biophysical modeling of STDP. Developments in this area, focusing on calcium time courses and the pathways that they activate, have been reviewed elsewhere [32, 35]. In this section, we focus on recent computational works that incorporate spatial aspects of postsynaptic signaling in STDP.

In 2001, Franks et al. published simulation results tracking spatiotemporal features of calcium influx into a model dendritic spine, through voltage-gated calcium channels and NMDA channels, associated with paired EPSPs and back-propagating action potentials (BPAPs) [27]. By including CaM in the PSD of the spine, they demonstrated the dependence of CaM activation on the frequency with which the paired EPSPs and BPAPs were delivered, modulated by parameters associated with calcium binding proteins [27]. These simulations were performed using MCell, which utilizes Monte Carlo methods to track over time the positions of molecules evolving within a three-dimensional spatial environment as well as channel states and molecular interactions, as we describe in more detail in Section 2.2.3. The authors followed up on this work with MCell simulations of glutamate receptor activation by vesicle-driven neurotransmitter release [26, 29]. These works illustrate the potential of Monte Carlo simulations performed in the MCell environment for the investigation of key processes in synaptic transmission and plasticity at the molecular level. In particular, these simulations allowed for the manipulation of parameters, such as locations of presynaptic release sites or neurotransmitter concentrations within vesicles, that are not easily accessible experimentally, yielded estimates of molecule concentrations that may be difficult to measure experimentally and are free from intermediate dye effects, and led to novel predictions, such as the conjecture that postsynaptic responses to synaptic inputs will rise more rapidly with increases in synaptic receptor density within the PSD than with increases in synaptic area.

The computational study of spatiotemporal aspects of postsynaptic signaling in synaptic plasticity has been continued in more recent papers. Keller et al. advanced the earlier work on CaM activation due to paired presynaptic glutamate release and postsynaptic spikes [51]. They tracked calcium time courses at different depths within a dendritic spine, showing that peaks in calcium concentration could be much higher than predicted from fluorescence signals, and the resulting CaM activation levels, which exhibited a sensitivity to pre-post timing consistent with STDP. These simulations did not harness the full spatiotemporal capacity of the Monte Carlo approach, in the sense that they did not examine effects of spatial variations in calcium across the PSD or at other fixed spine depths, but they did examine differences in CaM activation between the case of uniform CaM

distribution within the spine and the case that CaM is restricted to the PSD.

The natural direction for the extension of this work is the incorporation of additional signaling molecules and biophysical details associated with the PSD, including information about baseline spatial profiles of relevant components. Urakubo et al. developed a model, which they simulated using GENESIS, that included CaMKII, CaN, protein kinase A, adenylyl cyclase 1/8, cyclic AMP, phosphorylated inhibitor-I, protein phosphatase 1 (PP1), and protein phosphatase 2A, in addition to calcium and CaM [104]. These agents were allowed to diffuse between postsynaptic cytosol and PSD compartments; however, unlike in MCell simulations, molecules within a compartment were assumed to be evenly distributed and to interact with each other via mass action kinetics. In their simulations, presynaptic stimulation events triggered presynaptic glutamate release probabilistically, leading to AMPAR and NMDAR activation on a multi-compartment Hodgkin-Huxley-type model postsynaptic cell. Calcium influx via voltage-gated calcium channels and NMDARs initiated signaling cascades, which could induce plasticity by affecting AMPAR trafficking in the PSD and hence synaptic conductance. Although plasticity outcomes consistent with experimental results were obtained under simulation of 1 Hz presynaptic stimulation together with postsynaptic membrane depolarization (LTP) or hyperpolarization (LTD), the LTD resulted from transient activation of CaN and PP1 and hence was itself transient. Moreover, simulated post-before-pre STDP experiments did not induce LTD until the model was amended to include allosteric kinetics of NMDARs. Specifically, the binding of Ca^{2+}-CaM to NMDARs has a suppressive effect assumed here to be critical to spike timing dependent LTD. STDP results consistent with experiments were found when Ca^{2+}-CaM binding to glutamate-unbound NMDARs, as arise in post-pre paradigms, was assumed to be fast, while binding to glutamate-bound NMDARs, as are present in pre-post paradigms, was assumed to be slow.

Thus, this work led to the central prediction that allosteric kinetics of NMDARs that depends on the binding of glutamate to NMDARs, and thereby on the timing of presynaptic release and postsynaptic spiking, is critical to STDP. This prediction builds off of the assumption that calcium levels below baseline are needed to trigger spike timing dependent LTD [30]. Although this hypothesis is at odds with certain hippocampal results [78], the authors could propose reasonable resolutions for these discrepancies, in part by including a Ca^{2+} indicator in their simulations. Perhaps the most important point here is the proof of principle that biophysically detailed simulations, taking into account specific calcium sources and PSD features, can be used to suggest detailed, mechanistic explanations for experimental outcomes and to generate novel predictions for subsequent experimental testing.

As noted in Section 2, different NMDAR subtypes may make specific contributions to plasticity outcomes, and it will be essential for future models to incorporate these subtypes, their spatial profiles, and the spatial aspects of associated signaling cascades. An impressive step in analyzing NMDAR subtypes' roles, and in explaining disparities across experimental findings, was taken recently by Santucci and Raghavachari [91]. They constructed a model incorporating glutamate release and diffusion, binding to NR2A- and NR2B-containing NMDARs (as well as triheteromeric NMDARs), NMDAR opening and closing, calcium influx, and CaMKII activation and simulated this model using Monte Carlo methods that incorporated spatial locations of model components. Importantly, spatial information was confirmed to be critical for their simulation outcomes. For example, the opening probability

for NR2B-type NMDARs in the model was found to depend strongly on the receptor location relative to the site of glutamate release. Moreover, the ability of NR2B-type NMDARs to evoke LTP, by driving CaMKII autophosphorylation, varied significantly with the number of these receptors influenced by glutamate release, offering a possible resolution for diverse experimental results on how NMDAR subtypes contribute to plasticity outcomes [6, 64, 112, 74, 53, 6, 4, 55].

As with the work of Urakubo et al. [104], Santucci and Raghavachari's paper [91] includes several specific, biophysically detailed predictions emerging from their simulations, the experimental testing of which will have significant implications for our mechanistic understanding of synaptic plasticity.

2.2.3 Materials and methods: A spatiotemporal postsynaptic signaling model in MCell

Clearly, models and simulations of pre- and postsynaptic cell interactions and postsynaptic signaling in synaptic plasticity paradigms have become relatively sophisticated. The numbers of components involved in these models and the need to include spatial information about them may seem daunting. The aim of this section is to describe the MCell three-dimensional Monte Carlo simulation environment, which greatly facilitates simulation of such models, as well as our particular use of this environment in the context of STDP. We suggest that MCell will be a useful tool for future computational efforts relevant to STDP, as many important modeling and simulation steps, such as incorporating specific spatial distributions of NMDAR subtypes and postsynaptic signaling molecules, remain to be performed as further experimental findings emerge.

The biophysical models for synaptic plasticity described previously differ across physiological scope and technical implementation. Most, however, share a common base established by intracellular calcium concentration and downstream molecular pathways of interest. Our modeling approach, summarized in Figure 2.3, incorporates important biological components thought to be required for calcium-mediated plasticity into a rich simulation environment. Our particular simulation efforts began with a deterministic, phenomenological calcium detector model that was originally developed to convert postsynaptic calcium time courses into STDP-like changes in synaptic weight [88]. The deterministic model, based loosely on downstream calcium-mediated molecular pathways, was able to capture the differential effects of complex STDP induction protocols tested experimentally. From this model, intracellular calcium concentrations and ionic currents were computed across a 80 millisecond window to produce baseline values as a benchmark for outputs obtained from simulations of our spatially extended model.

Selection of a simulation environment Selection of a suitable simulation environment was made with the goal of providing the highest level of detail possible within a computationally tractable framework. To address the question of local calcium signaling, the simulation environment needed to allow for the definition and tracking of local concentration differences within a volume scale on the order of a single synapse. At this single-synapse scale, standard concentration-dependent compartmental models lose their ability to describe single molecule interactions as the ionic concentration of a single compartment falls below a single ion equivalent. Conversely, attempting to model this phenomenon using a detailed molecular approach is infeasible. Not considering the dynamics of

a single CaM molecule, the number of potential calcium binding partners within a single synapse ranges into the tens of thousands. The MCell (http://www.mcell.psc.edu/) simulation environment is uniquely positioned at an intermediate scale between high-resolution intra- and inter-molecule interactions and concentration-based compartmental models, which is well suited to capture plasticity phenomena of interest.

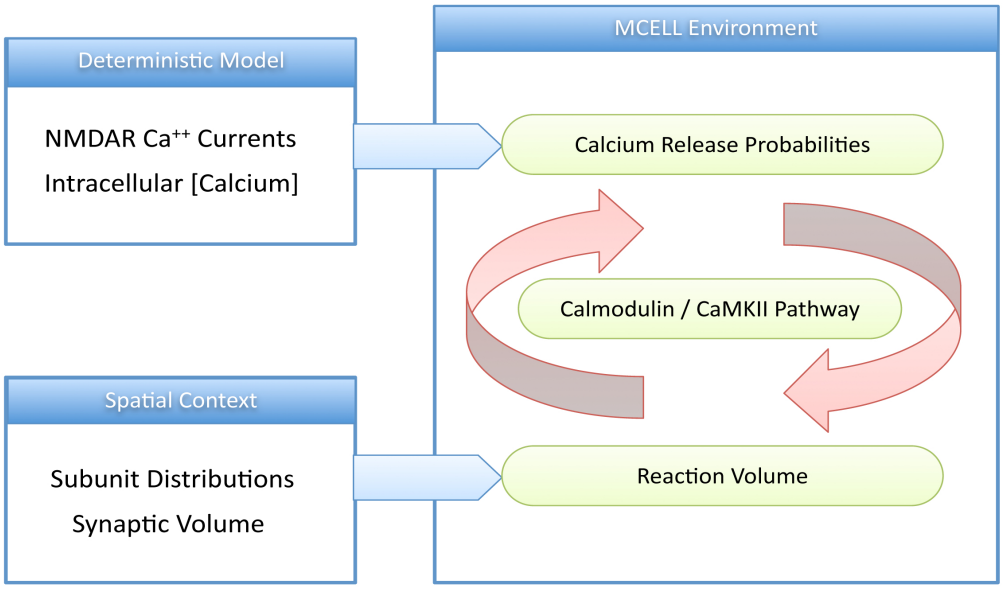

Figure 2.3: **Synapse model conceptual overview.** Our model builds on an earlier deterministic model [88] to incorporate subunit-specific channel kinetics into a spatial context. Calcium release profiles are calculated for NMDARs distributed on the postsynaptic density, based on deterministic calcium currents. Baseline intracellular calcium concentrations from the original model were used for validation.

The MCell environment is a heavily optimized reaction-diffusion Monte Carlo simulation tool that implements robust random number generation methods to create a stochastic simulation of reaction events within a realistic spatial context. As discussed in Section 3, MCell models have been used by multiple groups to simulate calcium-mediated signaling in dendritic spines. The extent of code required and job management is dependent upon the complexity of the system to be modeled. Basic models looking at molecular diffusion or simple reactions with known static inputs require little external code to implement. Supervised models that require either user- or script-based interaction during the simulation process are implemented by a checkpoint system furnished by the MCell environment. Using the checkpoint mechanism, it is possible to link an MCell simulation with other simulation environments (NEURON, GENESIS) to realize true multi-scale modeling. A recent chapter by Czech, Dittrich, and Stiles describes the complete step-by-step process of MCell model creation and further applications [17].

Model description Starting at the highest level of detail, the model is set within a cubic global reaction volume with 500nm side lengths (Figure 2.4). All volumes were defined by polygonal structures produced using the open source modeling software Blender (http://www.blender.org) or from transformed three dimensional primitives. The reaction volume corresponds to conventional dendritic spine head dimensions but differs from previous MCell models of synaptic plasticity in that all but the top face of the volume were semipermeable to free calcium and other ions. As a result, our model more closely resembles a spine-free dendritic synapse than a dendritic spine, such that it is relevant to neurons from young hippocampal cultures prior to initial spine formation. A postsynaptic density was defined by a thin cylindrical volume and placed just below the top face of the reaction volume. While the role of PSD proteins in inhibiting the free diffusion of molecules in a biological synapse is unclear, the PSD geometry in our model acts as a scaffold on which to distribute synaptic NMDARs. The PSD geometry was subdivided into four concentric synaptic regions: inner and outer active zones and inner and outer extra-synaptic zones. NMDA receptors were distributed on the surface of the synaptic regions based on normalized subunit-specific receptor localization profiles.

The NMDARs in our model were implemented as discrete, spatially defined calcium release sites. As our model environment lacks intrinsic electrophysiological activity, it is necessary to derive temporal calcium release profiles prior to the start of simulation. These release profiles are analogous to reaction kinetics of a conservative single-molecule decomposition reaction, NMDAR $\rightarrow$ NMDAR + Ca^{2+}, with an irreversible forward reaction coefficient.

To generate each release profile, the inward calcium current of the deterministic model was reproduced using NR2A- and NR2B-dominant subunit kinetics and channel conductances based on the experimental work of Erreger et al. in 2005 [24]. The updated model was subsequently validated against the original lumped model to demonstrate that our approach of introducing subunit-dependent release profiles could produce the same levels of global intracellular calcium as the original model. Each subunit-specific calcium current was converted from picoamperes into global subunit release probability according to an electrochemical charge balance equation. Single receptor release probabilities were produced by inversely scaling the global release by the number of NMDARs distributed on the PSD. This process was repeated to generate input profiles for pre-post and post-pre STDP conditions ranging across an 80 millisecond window. Single molecule parameters such as diffusivity and decay rate (via unspecified binding or transport) were assigned values from the literature. A baseline concentration of 800 nM was used as the target resting concentration of intracellular calcium. Diffusion coefficients for molecules in intermediary binding states (e.g. CaM bound to two calcium ions), which had not been experimentally characterized, were approximated based on unbound molecular weight of the base molecule. A 25 microsecond simulation time step was chosen based on the diffusivity of the most mobile ion, in our case Ca^{2+}, in accordance with the recommended step length from the random-walk approximation used by MCell.

The calcium detection pathway used in [88] was based on a reduced model of CaM binding and downstream activation. Calmodulin cooperatively binds up to four calcium ions to transition into what is referred to as its active state. To approximate this cooperativity, a 3-state system was implemented, incorporating unbound CaM, CaM bound to 2 calcium ions ($2Ca^{2+}$-CaM), and fully bound CaM (i.e., CaM bound to 4 calcium ions, $4Ca^{2+}$-

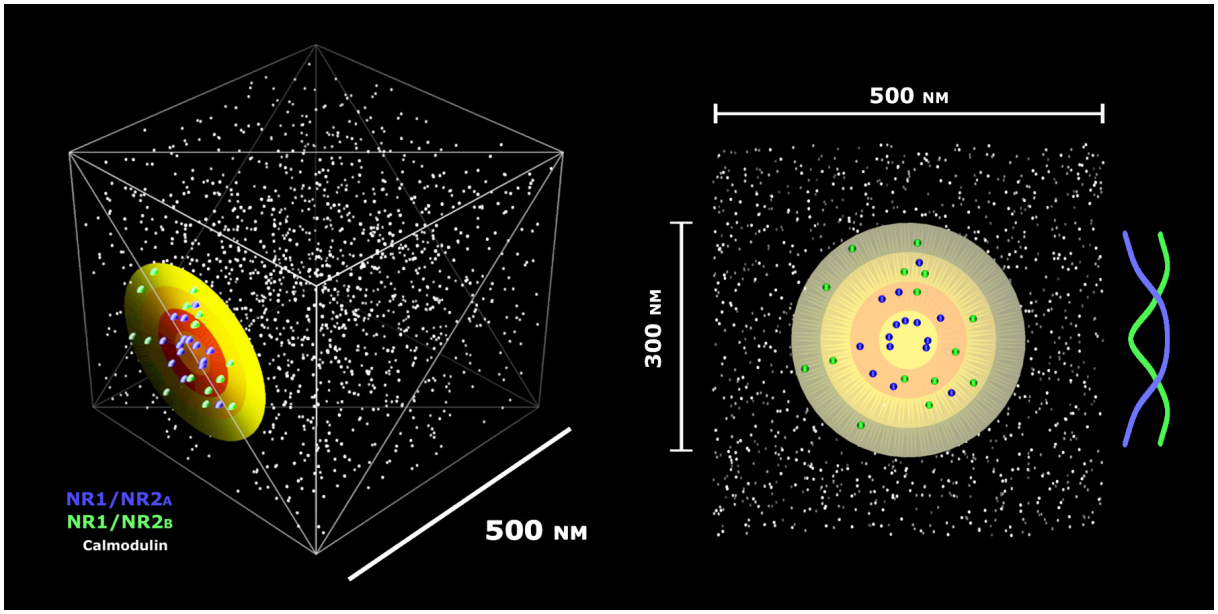

Figure 2.4: **Spatial postsynaptic model.** An isometric view of full reaction volume (left) and postsynaptic density region (right). White spheres represent individual calmodulin molecules. Receptors are placed radially within the PSD based on particular distributions (far right). Blue ellipsoids represent NMDARs that are equipped with NR2A channel kinetics while green ellipsoids represent NMDARs with NR2B channel kinetics. The four regions of the PSD are represented as colored bands.

CaM). To produce this approximation in a single-molecule environment such as MCell, forward reaction rates of Ca^{2+}-CaM + Ca^{2+} $\rightarrow$ 2Ca^{2+}-CaM were set so that all collisions between one- and three-Ca^{2+} bound CaM with a free Ca^{2+} ion would result in binding. Secondary interactions with CaMKII and CaN were based on a previously described kinetics of CaM-mediated activation [39]. Specifically, in our model, 4Ca^{2+}-CaM activates CaMKII and CaN. Physiologically, activation of CaMKII leads to autophosphorylation of CaMKII itself and additional kinase activity while CaN acts in an antagonistic fashion, activating phosphotases such as PP1 to dephosphorylate CaMKII [7, 39, 47, 63]. At this time, however, we focus on the state of Ca^{2+}-CaM binding, as others have done, while keeping in mind the eventual goal of studying differential CaMKII/CaN activation; preliminary versions of the downstream CaMKII/CaN interactions were implemented in our simulations, but these require additional refinement prior to use for the study of specific experimentally motivated questions.

2.2.4 Results

To quantify local signaling at different regions located within the synapse, sampling volumes were defined using particular location and size parameters. A variety of sampling geometries were implemented, namely a flattened sampling box following the work of Franks [51], an array of isometric cubes, a concentric set of cylindrical volumes, and a concentric set of half-spheres aligned with the subdivisions of the postsynaptic density. The parameters for each sampling array were set prior to simulation and used to generate indexed volumes. Total molecule count per sample volume over time is the primary yield of the simulation, from which comparisons of local signaling, across geometries and under various conditions, can be made.

The MCell model was calibrated to reproduce the peak global intracellular calcium concentrations obtained from the original deterministic model [88]. The calibration was performed with a parameter sweep of the initial resting concentration of bound CaM species. Figure 2.5 shows a comparison between deterministic global calcium time profile and three iterations of the MCell simulation. In theory, the probabilistic global concentration will converge to the intracellular calcium profile produced from the deterministic model as more simulation iterations are run.

An example of a simulation that we have run with this model appears in Figure 2.6. Calcium was measured by counting calcium ions in each of four concentric rings covering the PSD (Fig. 2.6, upper left) and converting the result to a concentration. The resulting calcium signal was temporally localized and was highest at the center of the PSD ($R = 0$), reflecting the distribution of NR2A-type NMDARs in the model (Fig. 2.4). Interestingly, the peak calcium level at the center of PSD (17 μM) was much greater than the global peak observed (8 μM). We repeated the experiment under simulated NR2A and NR2B knockout conditions, implemented in a straightforward way by eliminating NR2A-type and NR2B-type NMDARs, respectively, from the model. Under NR2A knockout conditions, the calcium signal became extremely weak, while NR2B knockout left the calcium signal almost changed (Fig. 2.4). Given that sufficiently elevated postsynaptic calcium is necessary and sufficient for LTP, these simulations are consistent with experimental results showing that NR2A knockout yields a significant loss of LTP while NR2B knockout leads to no significant change in LTP [64, 70].

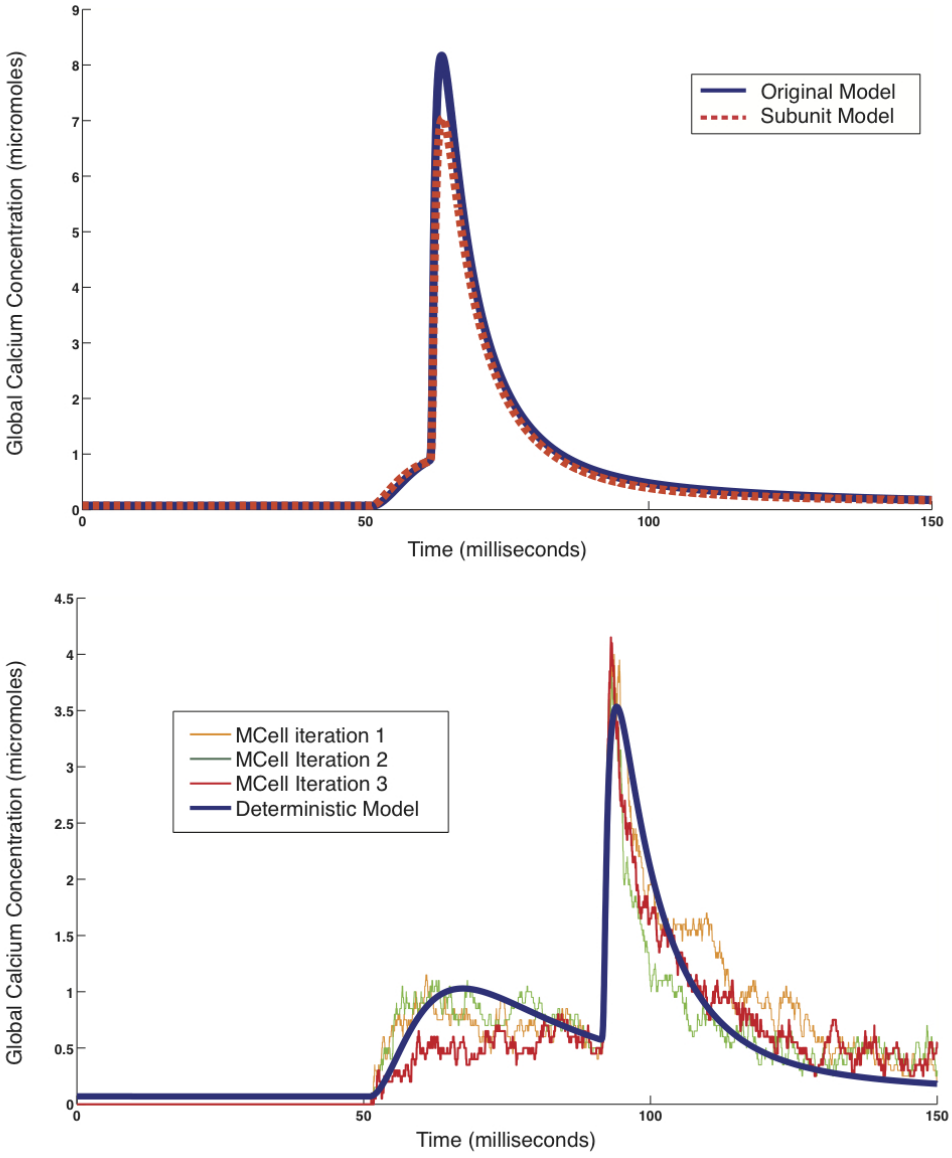

Figure 2.5: **Global calcium time course** Above: Postsynaptic calcium time courses generated by simulation of a stimulation protocol in which presynaptic stimulation precedes postsynaptic by 10 millisecond (pre-10-post) from the original deterministic model [88] and the expanded subunit-specific model. Below: A comparison between the deterministic global calcium time profile of a pre-40-post stimulus and three discrete trials of the MCell simulation. As more simulations are carried out, the probabilistic mean will converge to the deterministic profile.

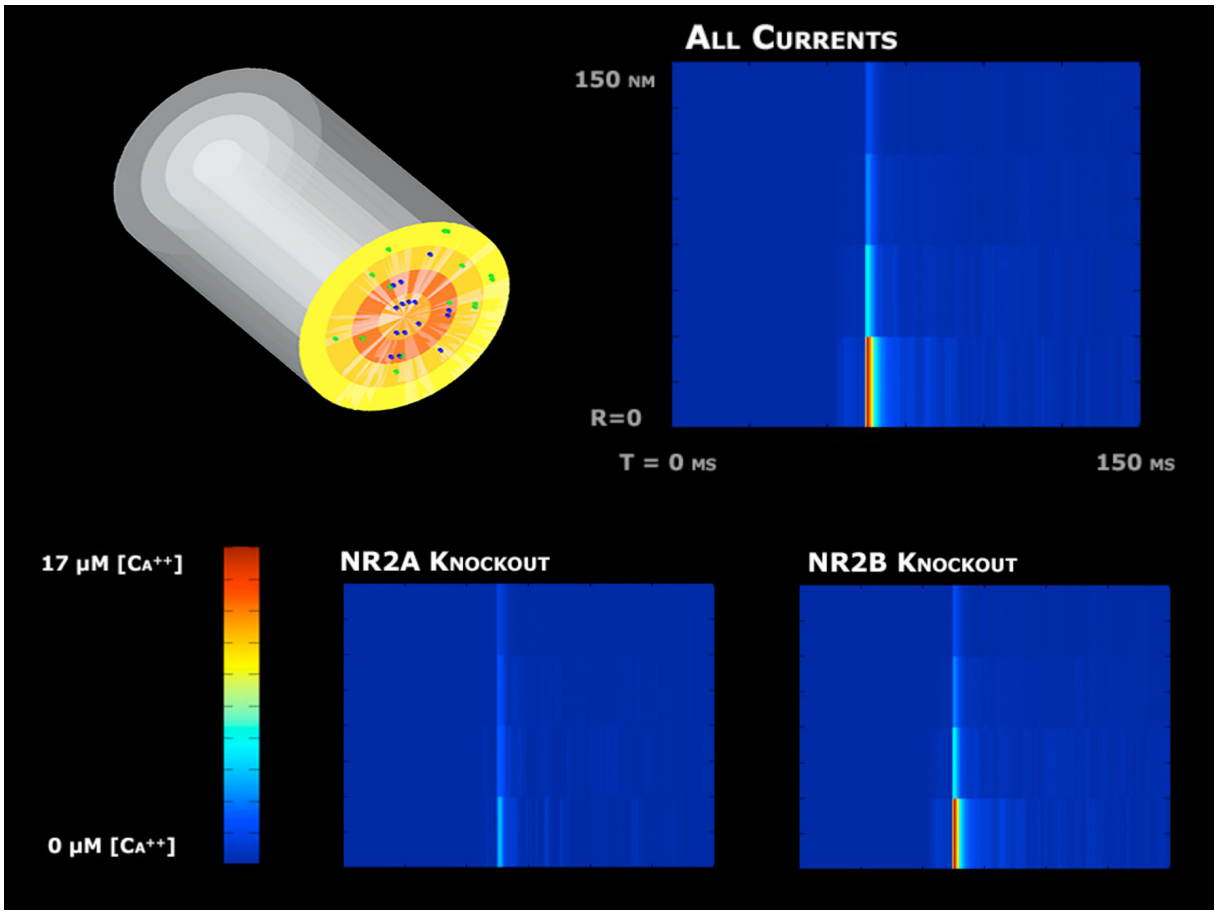

Figure 2.6: **Spatiotemporal calcium profiles for pre-10-post input conditions.** A pre-10-post stimulation induces a significant amount of NR2A-based calcium influx, presumably leading to potentiation. The spatiotemporal time course of intracellular calcium is plotted with the center of the PSD at R=0 on the vertical axis and the peripheral edge of the PSD at the top of the vertical axis. Results from simulation of an NR2A-dominant NMDA knockout show a pronounced decrease in the levels of intracellular calcium throughout the PSD, while an NR2B-dominant knockout shows minimal effect on the calcium influx due to the simulated protocol.

2.2.5 Discussion

Recent findings have suggested that potentiation and depression in STDP experiments depend on spatial aspects of signaling within the postsynaptic neuron, with different NMDAR subtypes playing particular roles in generating these signals and plasticity outcomes. We have described the preliminary steps of an application of the MCell modeling framework, which has previously proved useful for the study of synaptic plasticity [27, 51, 91], to introduce intracellular calcium time courses into a rich, spatially extended synaptic model. These represent a foundation from which efforts to address the contribution of spatial effects, including specific roles of NMDAR subtypes and their spatial distributions, could naturally progress, as further experimental data becomes available.

In one intriguing recent experimental development, for example, NMDAR subtype-specific lateral diffusion was demonstrated in hippocampal slices. A corresponding increase in the synaptic NR2B/NR2A ratio was linked to the conversion of an LTP protocol into a cause of LTD [117]. One could interpret this result as indicating that high NR2B levels favor LTD, regardless of their spatial location. Before making this assumption, however, it will be important to explore the details of the calcium time course induced by the classical paired-pulse plasticity protocol used in those experiments, its dependence on the NMDAR subunit ratio, its interaction with relevant molecules located postsynaptically, and how these characteristics compare with those induced by other plasticity protocols, such as those used in STDP. To address these questions and others that arise from them, modeling approaches such as the one described here will need to be adapted and extended to encompass the range of spatial and bimolecular complexities found in the physiological synapse.

There are three important areas that need to be addressed in this model development process. The first is establishing the proper description, at the appropriate scale, for the phenomena of interest. STDP is a robust outcome obtained across different synapse types and organisms; however, the presence of fine-grained single molecule dynamics or bimolecular interactions may be responsible for the sharp transition from potentiation to depression within the STDP window. priori hypotheses should serve as guidelines to define the scale, and the corresponding approximations and sampling methods, used for any model. The approach that we have described allows for simulations that incorporate features at a variety of scales. This breadth provides the opportunity for many avenues of exploration, such as the inclusion of allosteric inhibition, the incorporation of receptor lateral diffusion in the PSD, and the tracking of more granular intermediates in downstream molecular pathways, to be pursued in future spatial modeling efforts.

The second step entails setting up an appropriate simulation environment to explore the issues under study. The MCell framework allows consider flexibility for defining and sampling a rich spatial environment. For example, as mentioned in Section 3, in MCell models of calcium-buffer binding, a properly described environment enabled researchers to predict local signaling beyond the spatiotemporal resolution of current fluorescent reporters [51]. Our approach just scratches the surface of the demonstrated capabilities of MCell, which include incorporation of serial EM models of acetylcholine synapses [14], simulation of dynamic geometries for the study of exocytotic mechanisms [17] , and integration with multi-scale simulation environments such as NEURON [51]. However, the fate of a single ion in a synapse is complex. Electromagnetic field effects and porous structures that can restrict

diffusion may play a role in spatial signaling and are not currently captured in an MCell environment. Advances in the simulation capabilities will grow with researchers' ability to better describe and define the local reaction environment.

Finally, with phenomena of interest and model in hand, the issue that remains is the practical implementation and infrastructure requirements of the approach. The complexity of a model will increase with its richness, requiring a greater amount of overhead in both software and hardware. Fortunately, both areas have seen and will continue to see a large amount of development from researchers and technologists. On the hardware front, while raw CPU speed increases are slowing, the number of cores per CPU is steadily on the rise. This development has sparked the interest in parallel computing, which can be harnessed in MCell models and other large-scale simulation environments to take advantage of large numbers of cores and distributed memory resources. To make full use of this capacity, cluster management and workflow software has been developed that can handle model creation and job execution [82]. Our model code was developed following a minimal script configuration managed in Matlab (Mathworks, 2009), enabling the creation of model inputs as well as data analysis in the same platform. This approach utilized automated generation of MCell input profiles from a secondary model environment as well as procedural generation of sampling volumes within the reaction volume. It is important to consider the model implementation during specification as the type of inputs and analysis may differ depending on the workflow to be used. Open source options developed specifically for higher-order models exist that integrate multiple tools, such as NEURON or the R statistical environment, within the MCell framework. The Virtual Instrument [15], or more recently the Kepler project [65], are examples of scientific workflow systems that abstract the technical details of the simulator and focus on the scientific questions. Clearly, these and other computational advances set the stage for the future implementation of simulations of spatiotemporal signaling in synaptic plasticity, which will offer an immense potential for the exploration and generation of hypotheses about mechanisms underlying plasticity outcomes observed experimentally.

2.3 RECURRENT ACTIVITY IN CONSTRAINED NETWORK MODELS

2.3.1 Neural activity in small networks

Understanding neural activity within a small network context is often difficult due the high degree of variability inherent from the random self-organization found in most natural networks. The model of synapse formation followed by refinement is well established as a biological means for producing order from the chaos of the initial organization. However, most experimental preparations for the study of neural activity in small networks are time-limited or unguided in their development.

Experimental preparations developed from a mouse hippocampal slice are available to provide a conserved network macrostructure with consistent cell counts and distributions. Hippocampal slice preparations overcome organizational limitations by using preexisting network structures established during the normal course of animal development. Conserved synaptic pathways are readily accessible for studies of synaptic plasticity. Recently, waves of activity have been visualized traversing across a single slice using high resolution microelectrode array recording [43]. Slice preparations are amenable to perturbation using bath perfusion methods, making it possible for researchers to study underlying biophysical mechanisms responsible for producing different modes of neural activity. However, even the smallest networks within a slice preparation obfuscate activity at a local (10 to100 neuron) network scale.

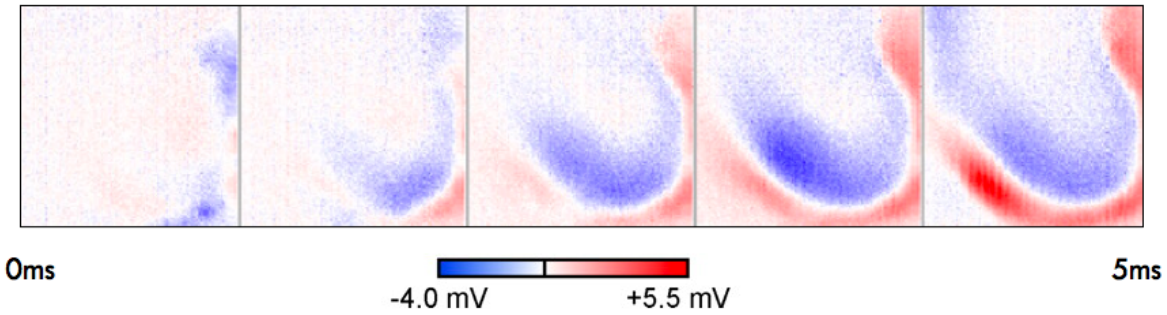

Figure 2.7: **Wave propagation in a hippocampal slice.** Local field potentials measured over 5ms with an $8\mu m$ resolution. (Modified from Hutzler, 2006 [43])

Dissociated networks of neurons *in vitro* provide a way to limit the number of cells within a network, therefore reducing the level of connectivity present. Dissociated networks however, are usually short-term preparations with no form of guidance to direct synapse formation or refinement. Some recent techniques utilizing microelectrode arrays to stimulate a small network neurons show promise for aiding in the refinement of the local connectivity [107]. Other approaches being developed focus on constraining the physical location of neurons *in vitro* to artificially limit the degree of interconnectivity within a network [106]. Of particular interest is the presence of oscillatory activity in these constrained networks. Volman et. al. implicate synaptic mechanisms for producing

and maintaining this activity and have developed a kinetic model that follows their experiment approach [106]. This approach, however, is still limited by a large degree of interconnectivity. Such interconnectivity produces waves of activity that propagate and collide on a two-dimensional plane, making proper characterization of single wave formation and termination difficult.

2.3.2 Research approach

A computational model was developed to explore the contribution of spatial constraints on oscillatory network activity described previously [107, 106]. Our model was developed with the premise of constrained neural adhesion producing differing degrees of interconnectivity. The model was built from real-world parameters with the eventual goal of *in vitro* reproducibility and characterization.

With the spatial constraint developed, it becomes possible to frame questions regarding spatial contributions to network activity in terms of geometric parameters. Using a rectangular pattern, these parameters would take the form of total surface area and aspect ratio. Consider a hypothetical comparison between the two classical rectangular shapes with equal areas: a narrow rectangle with an aspect ratio of 100:1 and a square with an aspect ratio of 1:1. While total surface area remains constant, the type and modes of activity present in a network cultured on each shape will be inherently different. Waves of activity may propagate from one end of the narrow culture surface to the other without colliding with another wave. Conversely, waves of activity within the square culture area may encounter transverse waves in addition to any parallel waves, resulting in activity patterns more analogous to fluid dynamics simulations than basic wave-based models.

This generalization, however, does not hold across all scales. As the size of the patterned region expands with respect to the static neuron size, effects from a constrained aspect-ratio are abolished. The presence of scale-dependent parameters often confounds the study of dissociated cell cultures but provides a useful interface to explore the effect of various spatial parameters on activity type. A second key component to come from the hypothetical comparison is the realization that pseudo-dimensionality reductions are possible from constrained geometric parameters. By extending this idea to a cyclic ring geometry, it is possible to compare patterns of recurrent activity found in fully-connected models [106] with patterns of activity only found in narrow rings structures. Here we pursue a second line of studym evaluating the site of wave origin, propagation velocity, and preferential direction of propagation in terms of ring diameter and track widths. Like the rectangular example, we are able to dissociate scale-varying from scale-invariant features of the network activity by scaling the overall network size.

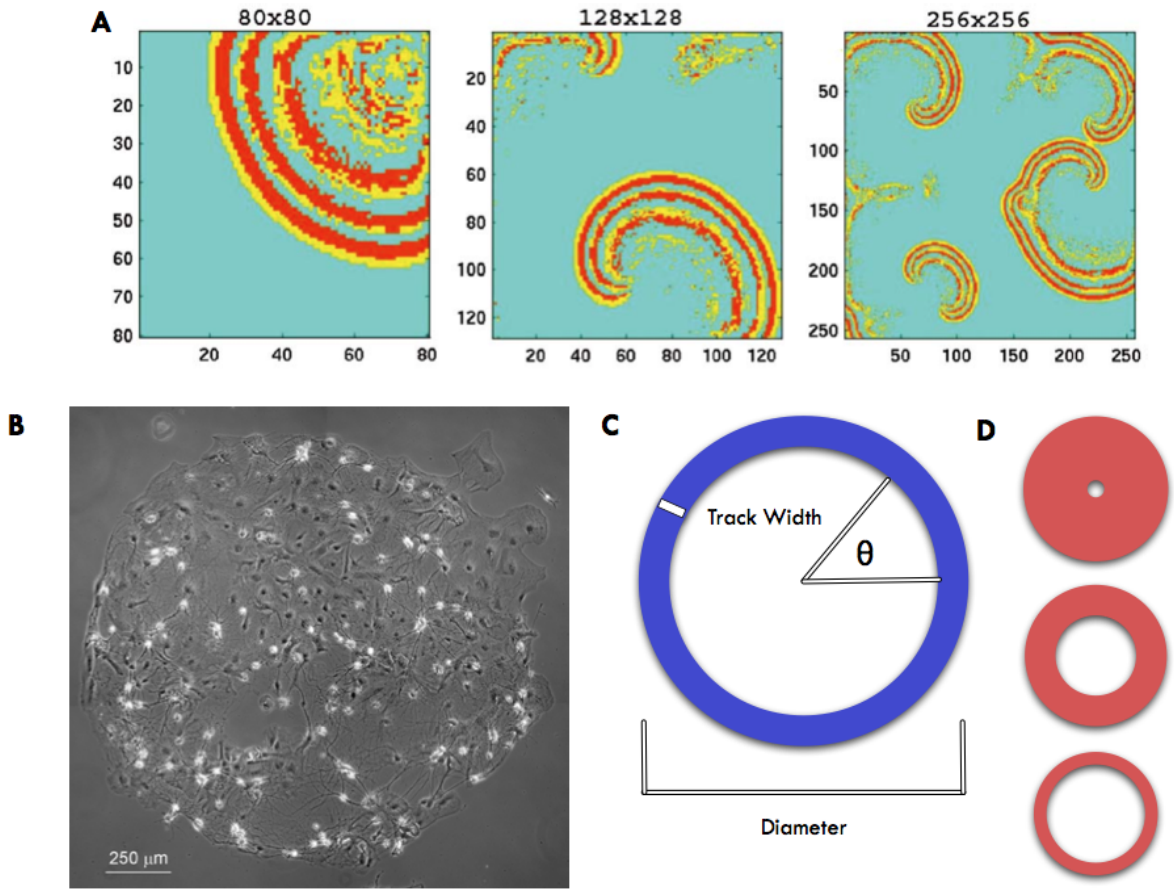

Figure 2.8: **Spatial models of neural networks.** A) Demonstration of scale-based network activity. Wave propagation and collisions in this two-dimensional model produce different mean results for the network description (Modified from Rulkov, 2004) [89]. B) Dissociated neurons plated onto a stamped pattern of neuron-compatible surface proteins. Reverberatory activity was observed at this scale using calcium-based fluorescence imaging. (Modified from Volman, 2007) [106]. C) Ring geometry based on stamp dimensions to constrain activity to tangential path. D) Scale-based analysis by modifying track width while maintaining stamp outer diameter. Alternatively, track width is held constant while outer diameter is scaled (not shown).

2.3.3 Development approach

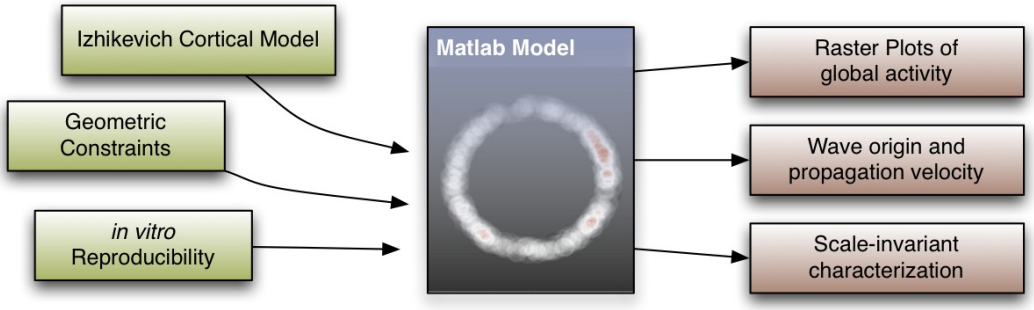

Figure 2.9: **Cyclic model workflow.** A model was constructed by extending the Izhikevich cortical model with geometric constraints defined to be reproducible *in vitro*. The model was coded in Matlab and yields results in the form of raster plots of spontaneous activity. This data is then used to determine wave origin, propagation velocity, and scale-invariant components underlying neural activity.

A neuronal network model was constructed to address the questions of spatial restriction on network activity at a local scale. The model is based off of a generalized cortical spiking model first published by Izhikevich[46]. The original model was developed around the premise of recreating the repertoire of neural activity found in cortical neurons and interneurons with a minimal set of differential equations. Starting from a reduced Hodgkin-Huxley model, the model description for each neuron was comprised of 2 differential equations and 4 abstracted parameters to define the resulting neurophysiology[46]. Neurons were then randomly connected independent of any spatial relationship. Using a 1000 neuron network (800 excitatory, 200 inhibitory), Izhikevich was able to reproduce physiological relevant alpha (10 Hz) and gamma (40 Hz) oscillations[46].

As a cortical model, the initial implementation of random connectivity was sufficient for the production of oscillatory behavior. To pursue the lines of study described previous, it was necessary to extend the basic cortical model to include spatially distribution and connectivity methods. Other groups have previously shown how to implement spatial forms of the base Izhikevich model and have provided a solid theoretical background to the scaling aspects of neural activity in small networks [89, 87].

Our model follows the standard approach as depicted in Figure 2.10. Model neurons are first randomly assigned a location on a spatial map. The spatial map is defined by regions of permissible locations from specified geometric input parameters for neuron placement. One modeling precaution that must be observed is the creation of a spatial map with sufficient resolution to provide a unique location for each neuron to be placed.

Once all neurons have been situated, a density map of neuronal locations is created. The density map is produced by summating a circular window for each neuron into a single image. Higher values correspond to higher regional densities of neurons. Similar density maps are produced for excitatory, inhibitory, and estimated synaptic weights.

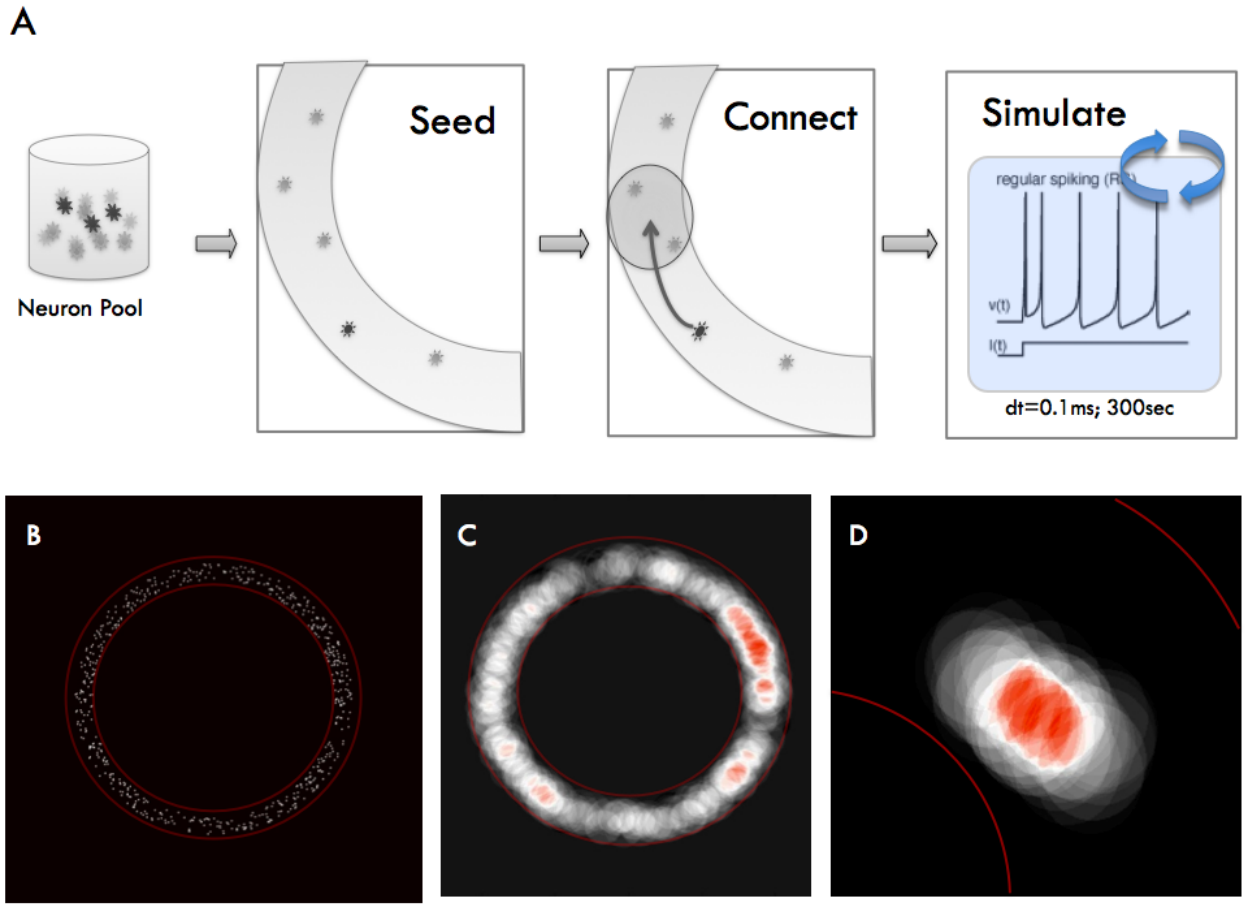

Figure 2.10: **Cyclic model pipeline.** A) To generate a spatial neural network model, neurons are first randomly distributed onto the permissible region. Synaptic weights are randomly assigned and scaled based on distance between neurons. Finally, the simulation is run to generate network activity. B) Model neurons distributed onto a cyclic pattern. C) Density map of network showing areas of highest concentration (red). D) Density map for a single network, showing strength and spread of the connectivity map.

Synaptic connections are established from a combination of individual neuron weight and distance measures. Random base synaptic weights are assigned to each neuron following with the base Izhikevich model [46]. Neuron-to-neuron weights are then calculated by multiplying the base weight with an inverse distance relationship from originating neuron to the target neuron. Finally, the model is vectorized and simulated with a sub-millisecond time step in Matlab (Mathworks 2009b) to produce membrane voltages and action potential fire times for each neuron. To visualize the raw activity, a raster plot of neuronal spike trains is produced and displayed by seed index or radial distribution. The raster plot by seed index provides a global overview of the level of activity within the network while the radially distributed plot provides a means for identification of propagating waves within the network.

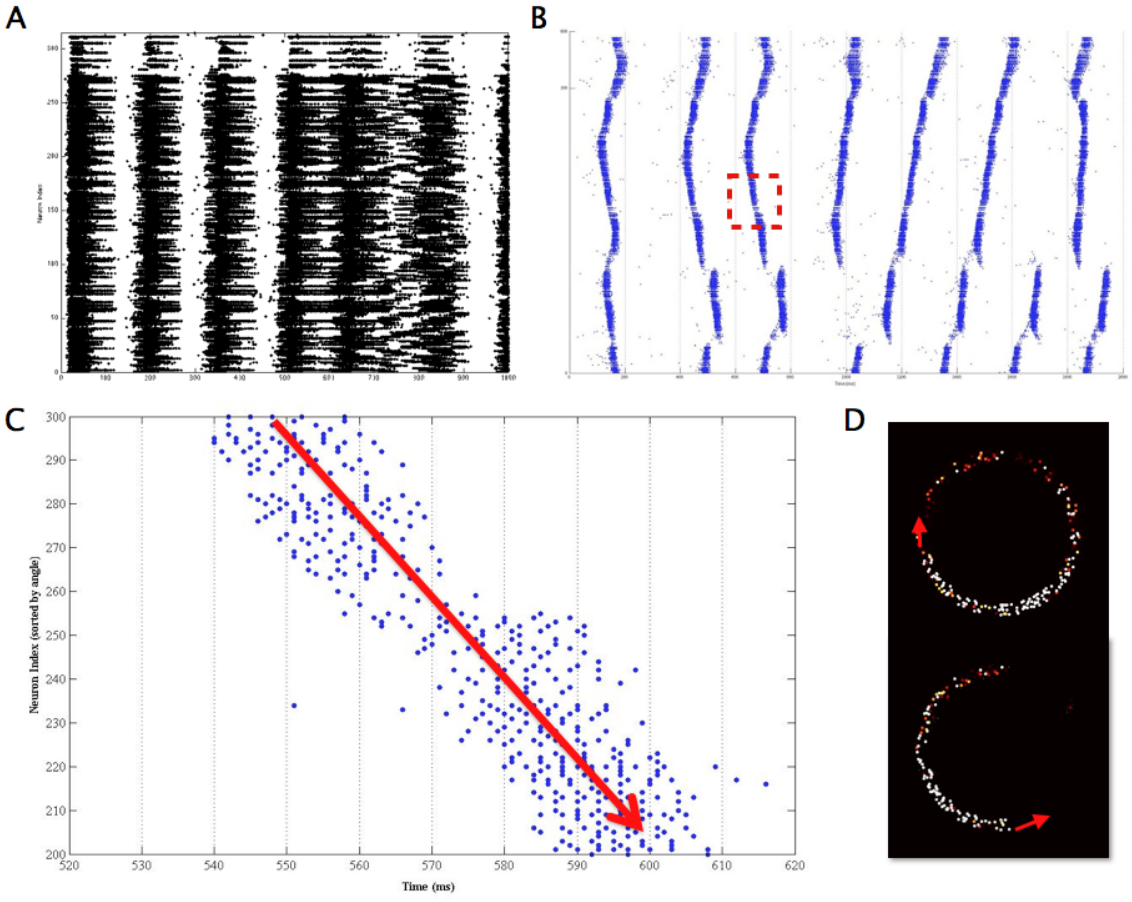

Figure 2.11: **Methods for quantifying activity.** A) Unsorted raster plot of action potential firing over time. B) Radially sorted raster plot showing organized wave propagation around a ring geometry. C) Detail view of highlighted region in B; wave velocity is determined from the slope of the linear regression of the selected data points. D) Directional wave propagation in different networks with similar seeding parameters, indicating sufficient anisotropy from random seeding and connectivity to create recurrent waves.

2.3.4 Quantifying activity

To supplement conventional metrics of network activity such as mean firing rate, inter-neuron correlation, and spectral analysis, additional metrics were developed and implemented in Matlab to describe wave activity and origin. Code for visualization methods and animations of network activity were also developed.

To calculate propagation velocity of a tangential wave, neurons were first sorted by their radial position and assigned a radial index. A regression was then performed on a region of space-time to produce a linear mean velocity of the wave. Figure 2.11B and C illustrate a highly-confined wave to demonstrate algorithm's application. Velocities are produced with in both relative and absolute terms (radians per second and meters per second, respectively).

To identify the origin of a particular wave, a moving-window regression is applied for the duration of the wave. Identifying the local minima programmatically yields areas of burst origin and collapse. These areas are then sorted by time to produce the start and end point of each wave or waves. For visualization purposes, burst origins may then be overlaid onto density maps produced during network formation. While this method has not been evaluated for robustness, adjustment of the moving-window span provides a means to accommodate networks with high variability or low neuron count.

2.3.5 Discussion and future work

The cyclic model described here is still in a preliminary form. Early results demonstrated propagating waves of activity as coefficients were scaled to account for the difference in mean connectivity density found in the all-to-all original model. The very presence of such waves indicates sufficient anisotropy present within the seeding and connectivity methods to result in recurrent activity. Unidirectional preference of propagation was not found within each network, which is to be expected from the random seeding. To revisit this issue in the future, an axonal segment extension is being developed for each neuron within the network. Placement of the axon terminal will be varied between a random distribution, following the random seeding method, and a directed approach, which places the axon terminal preferentially clock-wise/counter-clockwise within the cyclic geometry. This model extension should enable the study of propagation delays in the production of recurrent activity.

Finally, as was an objective of the original model, a series of in vitro experiments using dissociated neurons will be necessary to produce physiologically realistic model parameters. Preliminary work on this topic has already been started by peers with the promise of combining calcium imaging with model predictions to evaluate scale-based reverberatory activity in cyclic networks.

3.0 MICROFLUIDIC DEVICES FOR CELL CULTURE

Studying cellular development and communication is necessary to generate an understanding of the unique role different cell types play in the general operation of a biological system. Both development and communication are highly regulated, integrative processes that have been refined over the billions of years of eukaryotic cell evolution. Much of our current understanding of these processes is limited to how well scientists are able to dissociate specific signaling pathways from a larger set of cellular responses. This limitation is introduced by the working resolution of the instruments and experimental perturbations available. By increasing the static and dynamic working range of instruments, great advances can be made toward identifying key molecular and biophysical interactions, and mapping them to distinct cellular processes. With clever implementations and thoughtfully designed experiments great advances can be made in identifying key biophysical interactions and mapping them to distinct cellular processes.

3.1 CELL SIGNALING AND GUIDANCE

Local guidance cues play a fundamental role in developmental biology [49]. Cell migration and differentiation across multiple developmental time points is regulated by presence of diffuse and membrane-bound molecules. Substrate-based signaling acts via ligand-receptor pair binding and can present as either positive or negative modulators of cell behavior. The signaling mode can exist as a discrete on-off scheme or a graded transition over positive, neutral, and negative directors [60]. Minor changes in substrate concentration have been shown to have a disproportionate affect on actual cell behavior, causing a transition from attraction to repulsion over very short distances [60]. Differences in the slope of a concentration gradient has also been shown to have a similar affect [37, 60].

Development of the vertebrate visual system highlights the importance of synergistic interactions between different guidance cues to establish consistent functional networks and structures (Figure 1)[21, 42]. Network connectivity in the visual system forms from an orchestrated display of multiple extrinsic and intrinsic signals regulated by differential protein expression and secretion timelines [37]. Much work has been done to identify the various families of ligand-receptor pairs that are responsible for each cue during development. Netrin-NetrinR, SLIT-ROBO, and Semaphorin-Plexin represent the most studied soluble ligand-receptor pairs [21, 41, 25]. Ad-

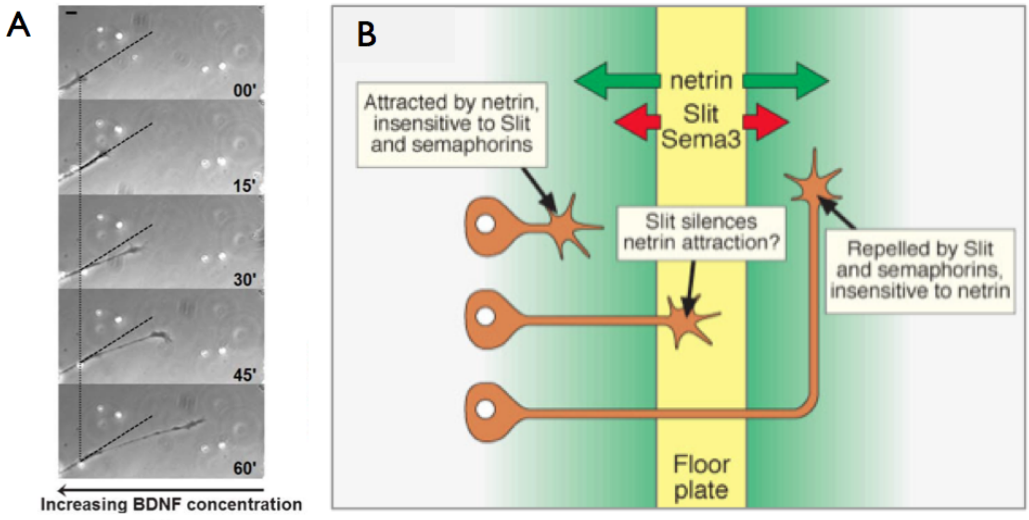

Figure 3.1: **Axonal guidance.** A) Axonal guidance against a gradient of a diffusible molecular cue (BDNF). B) Concerted signaling of netrin, slit, and semaphorin are responsible for regulating midline axonal crossings during early development [67].

ditional guidance roles are played by neurotrophic growth factors such as NT3/4, Nerve Growth Factor (NGF), and Brain-Derived Neurotrophic Factor (BDNF) [49]. The Ephrin-Eph pair, ECM-binding proteins (Laminin, Fibronectin, integrins), and cell adhesion molecules (nCAM, synCAM) are membrane-bound ligand-receptor pairs that also contribute towards guidance [21, 37, 42, 80]. The specific role of each family has been covered extensively in reviews by Dickson, Dalva, and Yoshimura [21, 18, 113]. Researchers have shown that while individual guidance pairs often obey Sperryś original one-to-one hypothesis, the final guidance cue is the result of combined interactions of several diffuse and membrane-bound gradients [48, 41].

To study individual guidance cues and their synergistic effects, proper spatial and temporal presentation of each molecular cue is required. Early studies have relied on selective patterning of culture surfaces or physical barriers to produce the controlled presentation of molecular cues. In vitro experiments were set up around Campenot chambers, Dunn chambers, stripe assays, and simple explants cultures to establish the foundational work in local guidance pathways [49, 3, 111]. Glass micropipettes have also been used to control the presentation of guidance cues to a precise region of a dissociated or slice culture preparation. Each technique brought with it unique advantages for the study of certain pathways. However, limitations in each system left a large area of experimental conditions inaccessible.

Glass micropipette techniques such as vacuum superfusion and microinjection allow for precise delivery of chemical stimuli across a very small region of interest (ROI) for a specified duration [105]. The downfall of a micropipette technique is the requirement of constant supervision during delivery, making long-term exposure

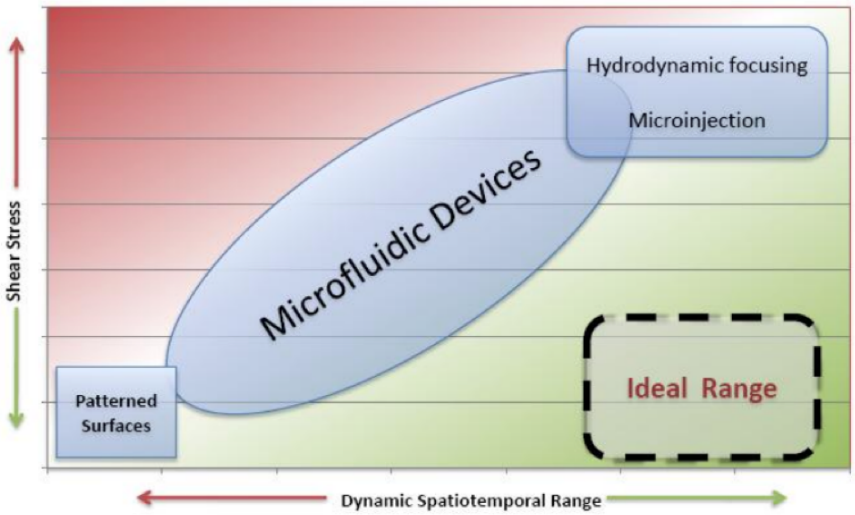

Figure 3.2: **Current microfluidic device capabilities.** Overlay of various microfluidic experimental methods for cell culture and perturbation. An ideal microfluidic device for neurosciences would have a large dynamic range - the ability to define the stimulus from a focal stream to a broad gradient - and minimal shear effects. Due to the direct relationship between high resolution and increased shear, novel approaches must be considered.

protocols difficult. Patterned surfaces represent the opposite stimulation paradigm. By treating culture surfaces with proteins of interest prior to seeding, it is possible to produce static concentration patterns or gradients of adherent guidance cues that remain stable for the length of the experimental protocol [16, 116, 81, 100, 9].

3.2 MICROFLUIDIC DEVICES FOR CELL CULTURE

Recent technological advances in the past decade have yielded a third experimental option: Microfluidic devices. [36, 96, 73, 83]. Commonly fabricated from Polydimethylsiloxane (PDMS) or etched into a silicon (Si) wafer, a microfluidic device contains micron-scale features to guide fluid flows using input pressure, internal pumps, or electrokinetic forces [96]. Cell culture chambers with volumes ranging from pico- to nanoliter scales enable precise control of the internal environment and subsequent experimental perturbations applied. The small physical scale of each device allows for the production of high local substrate concentrations from miniscule quantities of (often expensive) reagent. Microfluidic devices for biology have an added advantage of scaling efficiently as many individual devices will fit onto a single microfluidic chip [99, 23].

3.2.1 Governing principles of microfluidic fluid flow

As the characteristic length of a flow regime decrease, the turbulent components of the Navier-Stokes equation drop out, leaving a simplistic flow environment [95]. Disproportionate allometric scaling of the viscous forces with respect to the fluid's momentum constrains all internal fluid flow into a laminar flow regime [95]. The dimensionless Reynolds value (Re) describes this relation and can be used to describe common flow environments (Equation 3.1). Generalized pipe-based laminar flow regimes exist at Reynolds numbers up to 2300. For $Re > 2300$ there exists a transitory region containing both laminar and turbulent microenvironments. A fully turbulent flow regime is established for $Re > 4000$ [96]. The regime transitions for specific channel cross-sections can be approximated using an adjusted hydraulic radius, as describe by Mortensen et. al. [75]. Calculation of Re may use fluid density (ρ), mean velocity (U), characteristic length (L), the dynamic viscosity (μ), and the kinematic viscosity (ν).

$$Re = \frac{Inertial}{Viscous} = \frac{\rho UL}{\mu} = \frac{UL}{\nu} \tag{3.1}$$

The characteristic order of Re within a microfluidic device remains $<< 1$ due to uneven scaling of the allometric area to volume ratio (See the 2005 Squires review [95]), forcing all flows to a laminar profile. An important issue that arrises from the low Re value is the absence of turbulent flow and thus the elimination of any turbulent mixing. All mass transfer within a microfluidic device must be accomplished by advective transport (along the flow path) and passive diffusion (perpendicular to the flow path)[96].

Hydrodynamic focusing microfluidic devices [1, 97, 109] take advantage of the laminar flow environment to focus and target a central laminar stream using peripheral laminar streams. Fluid flows intersecting in a laminar flow regime form parallel streams whose cross-sectional areas are proportional to relative driving pressures of each flow. Boundaries are formed between each set of parallel flows allowing for lateral diffusion of a chemical substrate from one stream to another. By defining the initial substrate concentrations, researchers are able to guides flow streams to target specific regions of a cell culture environment. By controlling relative inlet pressures of each stream, it is possible to predict and define the lateral position of each laminar boundary.

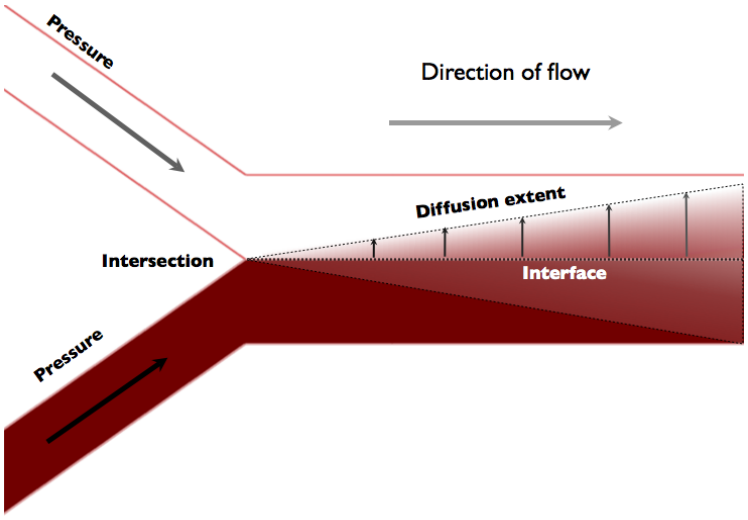

Figure 3.3: **Mass transfer in microfluidics.** Mass transfer is restricted to passive diffusion in a microfluidic flow regime. Transverse diffusion distance (one dimension), or the square root of the mean-square displacement can be determined as a function of time for molecules with known diffusion coefficients.

Mass transfer at laminar boundary is limited strictly to transverse passive diffusion. The extent of transverse diffusion is proportional to the square of interface time [8], a decrease in effective diffusion as flow rates increase. Therefore, to maintain tightly focused streams with minimal transverse diffusion, high flow rates are necessary. High flow rates introduce additional shear stress proportional to increases in flow rate throughout the system [96, 109, 52]. In an environment where laminar streams with different substrate concentrations come into contact, the amount of mass transport can be determined using a second dimensionless number: the Péclet number (Pe), calculated from the mean fluid velocity (U), characteristic length (L), and substrate diffusivity (D).

$$Pe = \frac{Advective}{Diffuse} = \frac{UL}{D} \tag{3.2}$$

The Péclet number describes the relation of advective mass transport with respect to lateral diffusive transport (Equation 3.2). A large Péclet value indicates a high degree of substrate containment within a flow stream. Using a third dimensionless term defined as the Schmidt number, Sc, to describe the ratio of viscous transport to bulk mass transport (Equation 3.3), it is possible to relate directly Pe to Re (Equation 3.4).

$$Sc = \frac{\mu}{\rho D} = \frac{\nu}{D} \tag{3.3}$$

$$Re = \frac{Sc}{Pe} \tag{3.4}$$

Unlike the Reynolds number, however, the Péclet number is not constrained to a characteristic order within a microfluidic device [95]. As a result, it is possible to define a mass transport profile range from highly-contained to fully-diffuse by varying the channel geometry and volumetric flow rate [96].

Hydrodynamic focusing devices exist at one edge of possible microfluidic flow environment conditions as defined by diffusion restrictions. Smooth gradient-producing microfluidic devices are located on the opposite edge [36] and take measures to ensure complete diffusion of chemical substrates. To overcome diffusion limitations, these gradient devices contain extended boundary lengths, optimized internal divisions, and/or ultraslow fluid flow rates to allow for sufficient interfacial time [115, 44] needed for complete diffusion. Many gradient producing features require large on-chip areas to achieve complete mixing (Figure 3.4)[48].

Both hydrodynamic targeting and gradient producing devices have been used for biological assays. Hydrodynamic devices have been used to selectively stimulate sub-cellular regions of cells for drug delivery and receptor clustering assays [101]. Gradient devices have been used to study applications ranging conventional cellular chemotaxis against a gradient of soluble growth factors to axonal turning assays based around molecular markers found in the developing nervous system [20].

3.2.2 Microfluidic device features

Multiple approaches are available to control driving pressures within a microfluidic device. Hydrostatic pressure differentials can be created by varying the relative height of external fluid reservoirs to create a steady fluid flow through a device. Hydrostatic methods suffer from a number of limitations including by not limited to indirect control of flow rate, flow rate decay over time, and evaporation [96]. Programmable syringe pumps may be employed to deliver fluid at a predefined flow rate through a device. Syringe pumps, while able to provide direct control of flow rate, are subject to mechanical limitations originating from the screw-based drive mechanism. At low flow rates, delivery profiles are susceptible to aliasing by the stepper motor. In scenarios involving parallel laminar streams, this aliasing produces an unstable boundary, effectively decreasing the precision of the focused stream. To overcome the limitations inherent in hydrostatic and syringe pump driven fluid flows, direct control over inlet driving pressures is often used [57].

Dynamic pressures sources have been demonstrated in microfluidic cell culture applications [57, 58]. A dynamic source consists of a regulated continuous pressure supply feeding into an electronic pressure controller (EPC). The EPC is then programmatically controlled with an embedded controller or PC interface. In addition to driving fluid flows, pressure-driven flows can be used to deform internal valve geometries of a microfluidic device [59, 103]. Pioneered by the Quake group [103], deformable internal geometries enable researchers to create push-down and pull-up valve features inside of a microfluidic device. A single valve feature is comprised of two parts: a flow channel and a control channel with no outlet. A thin PDMS membrane separates the two layers, allowing for gas diffusion out of the dead-end control channel during initial device setup and perfusion. Fluid flow through the flow channel is driven by a static low-pressure (P_f). To actuate the device, a high pressure (P_c) is applied to the control channel, forcing the thin PDMS membrane to deflect, obstructing flow in the flow channel. The amount

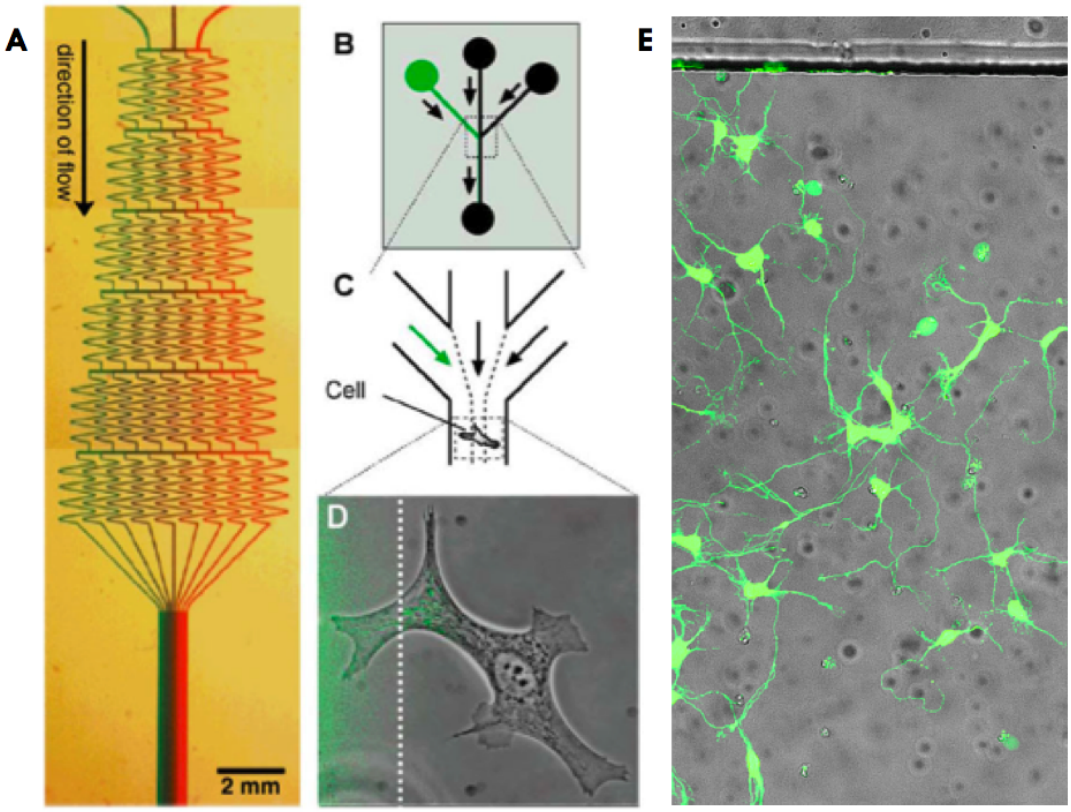

Figure 3.4: **Types of stimuli in microfluidic devices.** Two primary types of cue presentation are available when using a microfluidic cell culture device. Gradient generating devices produce smooth and stable defined distributions of the molecular cue of interest. To produce these cues, an increased interface time is created providing for sufficient time for molecules to diffuse into adjacent laminar streams. Focused or hydrodynamic devices produce laminar streams with a high degree of advective substrate motion. Hydrodynamic devices operate by minimizing the interfacial time between streams while localizing the target of interest as close to the stream intersection as possible. A) Smooth gradient generator, often referred to as a "Christmas Tree" configuration [111]. B) Three inlet single cell microfluidic device. C) Detail view of stream intersection. D) Selective labeling of a cell with membrane-permeable dye (Mitotracker Green). The fluorescence signal within the cell indicates increased intracellular diffusion with respect to advective flows [97]. E) Calcien AM labeled neurons in a microfluidic Device (Image from A. Vishwanathan, University of Pittsburgh 2009)

of deflection is directly proportional to the P_c/P_f ratio with minor hysteresis effects seen toward the fully-open and fully-closed limits. The Quake setup uses an external valve controller to provide discrete control, precise fluid handling and delivery with millisecond resolution, and minimal reservoir volumes on-chip.

To allow for greater dynamic control, the Folch group extended the initial Quake concept to create a device capable of modifying effective internal resistances of each flow channel [59] continuously. The Folch system used multiple push-up valves in a serial configuration to create independent resistances values within each channel. Following an electrical circuit analogy (similar to Figure 3.6A), the Folch device was then able to produce graded hydrodynamic profiles by varying the relative resistances over time.

3.2.3 Conceptual approach

We have developed microfluidic concept that integrates the key capabilities from binary and continuous device types described above to control the position of a focused hydrodynamic stream. The device concept uses compact deformable internal valve geometries, multilayer soft-lithography, and a dynamic pressure control platform to create coordinated fluid profiles and targeted substrate streams.

Our microfluidic platform extends the work of Folch by using a single variable push-down valve rather than multiple discrete valves as in their original implementation (See Figure 3.6B). The linear deformation of the push-down valve geometry makes this configuration possible as a function of control pressure (P_C)[103]. Therefore, by using an external dynamic pressure source, a continuous range of internal resistances can be achieved with a single push-down valve configuration. Our design therefore recreates the capabilities of a Quake-based and a Folch-based system while providing smooth control of valve open and close states with minimal on-chip space requirements.

3.2.4 Device descriptions

To aid in device description, we developed a categorical system based on method of driving pressure used and connected valve configuration. The three major devices classes are passive, driven, and dynamic. Passive devices refer to devices where the flow rate is governed completely by hydrostatic pressure differentials and internal valve state. Driven devices share all of the capabilities of the passive device configuration but also provide the option of high flow rate profile generation, useful for creating well-defined laminar streams with short interfacial times. Finally, dynamic devices implement a dynamic pressure source in conjunction with the binary valve system to provide an large dynamic range for arbitrary profile production with high temporal precision.

Each device configuration consists of four defining variables. The first of which is the actual device layout. Based on a CAD drawing, circuit-equivalent representations were created and labeled. Binary valves were represented by a SPST switch. Dynamic valves were represented as potentiometers. Color coding used to represent the type of pressure for each inlet: black circles indicates a passive (hydrostatic) source; blue circles represent a constant high pressure source (10 PSI); and green circles indicate a dynamic pressure source (0-30 PSI).

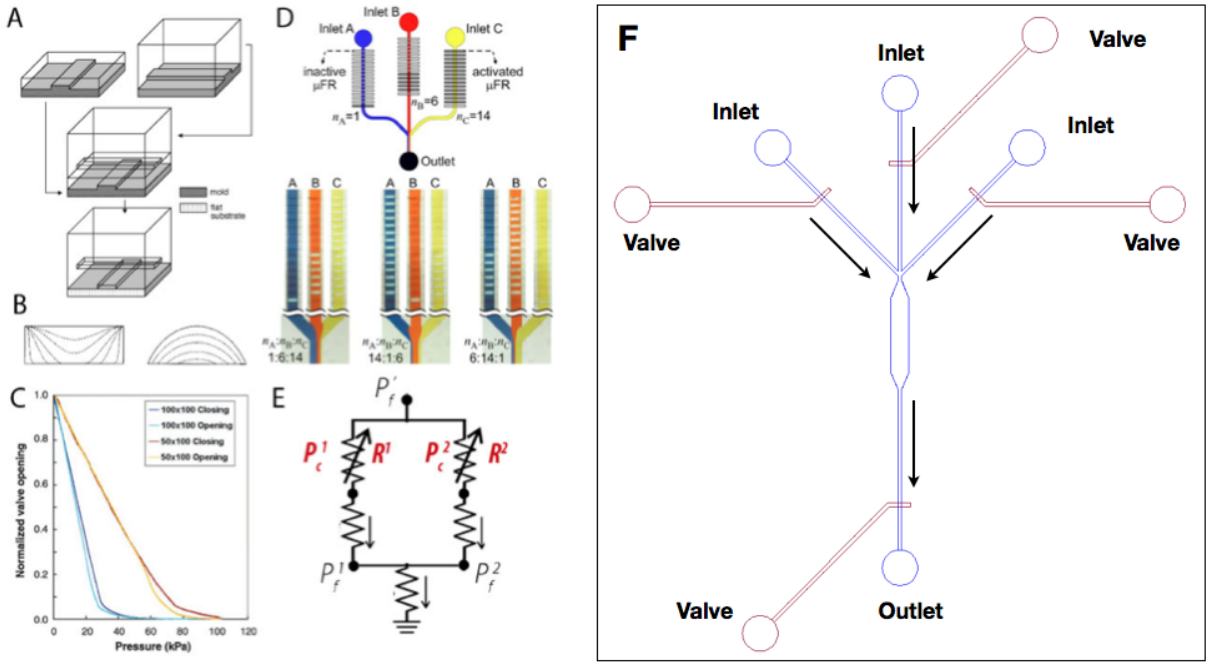

Figure 3.5: **Microfluidic features and conceptual design.** The conceptual device proposed here relies on three basic technologies. A) Internal valves are created using multilayer soft-lithography to direct fluid flows via external pressure sources. B) Rounded channel cross-sections ensure complete closure of the valve when sufficient pressure is applied to the control channel. C) A quasi-linear relationship exists for the opening and closing movement of the valve itself. Minor amounts of hysteresis are visible. D) Using multiple semi-open valves, differential control of channel resistance enables for precise laminar boundary positioning. E) Equivalent circuit model of D. Rather than utilize multiple inputs to determine a discrete channel resistance, a summed variable resister is substituted. F) CAD drawing of conceptual model. Three fluid inlets flow intersect at a flow chamber before exiting via the outlet. The summed variable resister described in E. is realized using a dynamic pressure source to create arbitrary valve closings, capable of producing a continuous range of interfacial boundary locations.

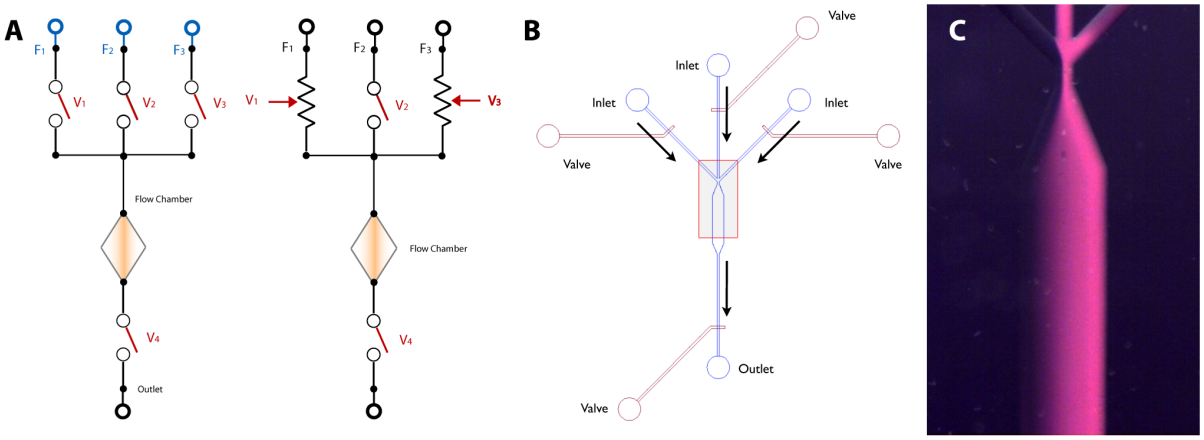

Figure 3.6: **Microfluidic design.** A) Circuit equivalent models for a binary device (left) and a analog device. The binary device operates by closing any of the three internal valves to control stimulus presentation. The analog device uses a dynamic pressure source to deflect the internal valves to partially-close or fully closed configurations, creating a large range of potential flow profiles. B) Device schematic - circles represent punched inlets in the actual PDMS device. C) Image of passive flow device with right valve closed. (Green McCormick dye used, colors inverted to aid visibility).

The second defining parameter is the state table. Similar to a karnaugh map, the state table maps the state of each device input to the type of flow profile expected in the experimental flow chamber. Unlike a karnaugh map however, the addition of using dynamic valving and pressure sources introduces an analog value for some of the input conditions. A half-closed valve is represented on a normalized scale from 0 to 1.

A third parameter defined is a predicted flow profile table. Using intensity profiles collected experimentally, the expected flow profile within the flow chamber is mapped to the input states that created it from the state table. This furnishes a description of the types of experimental profiles possible for each device type. The last parameter defines the physical connection between the each device input and the corresponding connection on the hardware controller and is used during experimental setup.

Passive devices Passive devices rely on hydrostatic differences between inlet and outlet fluid reservoirs. Both reservoirs are open to atmosphere, with the pressure differential proportional to height differences. The disadvantage, however, is the spatial resolution afforded by passive device flow rates. Slow flow rates result in long interfacial times leading to formation of diffuse linear gradients. Passive devices are therefore best suited for long-term experiments with sustained low flow rates needing smooth gradient production.

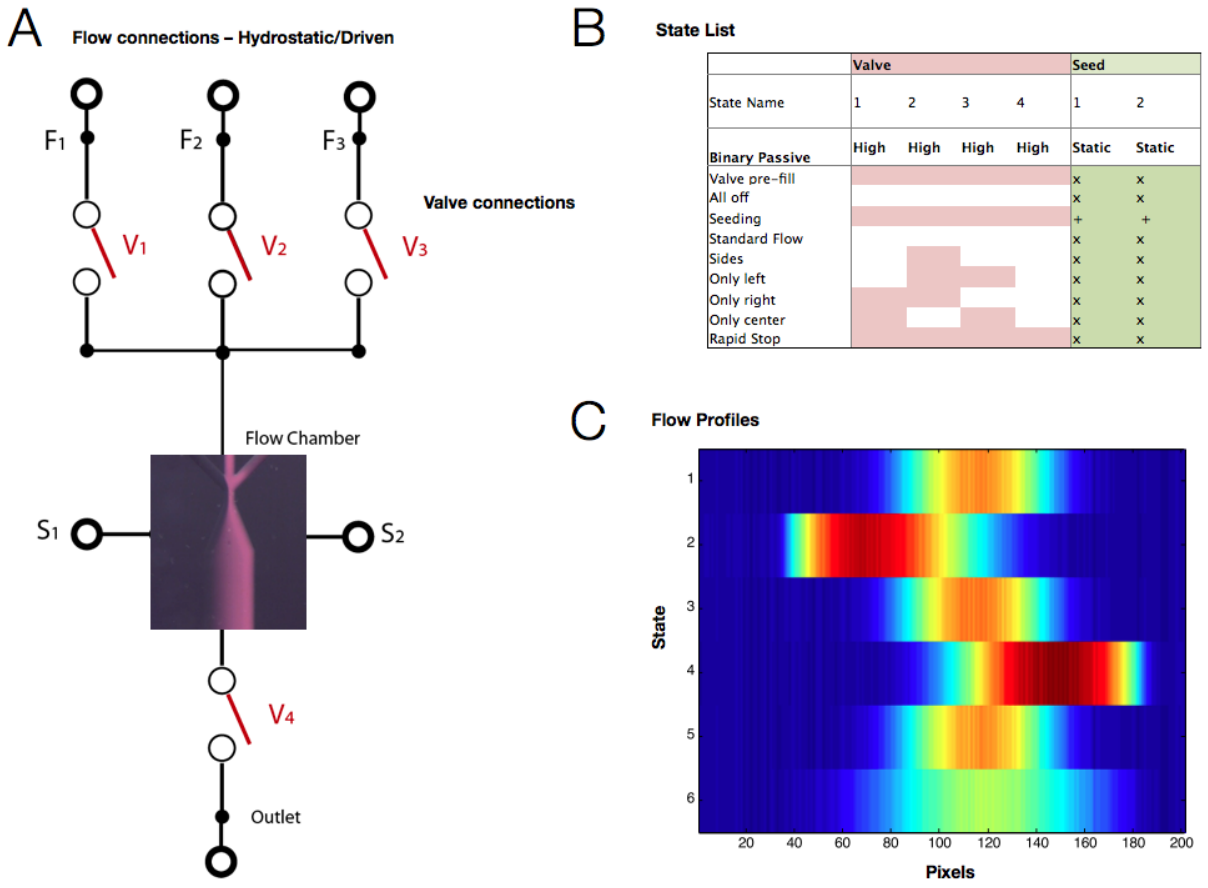

Figure 3.7: **General device description.** To fully describe a single device, it is necessary to know the input connections, which states are possible, and what type of profile each state will produce in the experimental chamber. A) Annotated circuit diagram of a passive device. B) State table for all possible device states. C) Flow profiles corresponding to each state.

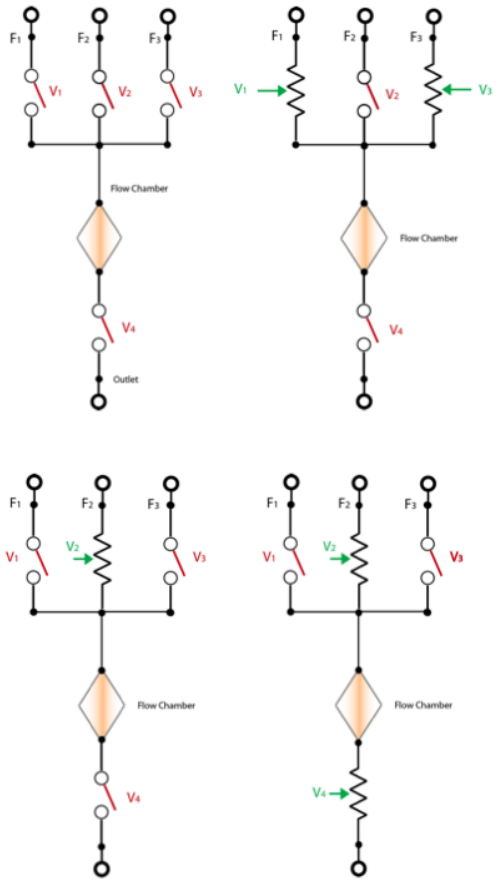

State	Description	F1	F2	F3	v1	v2	v3	v4	Description
S1	Normal flow	always on			0	0	0	0	*smooth gradient, central*
S2	left off				1	0	0	0	*smooth gradient, left to right*
S3	center off				0	1	0	0	*no stimulus*
S4	right off				0	0	1	0	*smooth gradient, right to left*
S5	flow off				1	1	1	0	*prevents fluid from entering*
S6	outlet off				0	0	0	1	*prevents fluid from exiting*
S7	left only				0	1	1	0	*contents of left stream*
S8	center only				1	0	1	0	*contents of central stream*
S9	right only				1	1	0	0	*contents of right stream*
S10	all stop				1	1	1	1	*All valves turn on, prevents any backflows*

	Description	F1	F2	F3	v1	v2	v3	v4	Description
S11	shift left	always on			0.5	0	0	0	*smooth gradient, peak slightly off center to left*
S12	shift right				0	0	0.5	0	*smooth gradient, peak slightly off center to right*
S13	expand				0.5	0	0.5	0	*smooth gradient, broader than Normal flow*

	Name	F1	F2	F3	v1	v2	v3	v4	Description
S14	focus	always on			0	0.5	0	0	*reduced central pressure = narrow central gradient*
S15	focus left				1	0.5	0	0	*reduced central pressure + v1 on = narrow gradient left to right*
S16	focus right				0	0.5	1	0	*reduced central pressure + v3 on = narrow gradient right to left*

	Name	F1	F2	F3	v1	v2	v3	v4	Description
S17	focus	always on			0	0.5	0	0	*reduced central pressure = narrow central gradient*
S18	focus left				1	0.5	0	0	*reduced central pressure + v1 on = narrow gradient left to right*
S19	focus right				0	0.5	1	0	*reduced central pressure + v3 on = narrow gradient right to left*
S20	slow flow				?	?	?	0.5	*reduces overall flow rate through device (applied to D1+D4 states)*

Figure 3.8: **Passive device descriptions.** A) Device layouts for I. Basic, II. Peripheral, and III / VI Central subclasses of device type. B) Base state table and supplemental tables for subclass-specific functions. All passive devices share states S1 to S10.

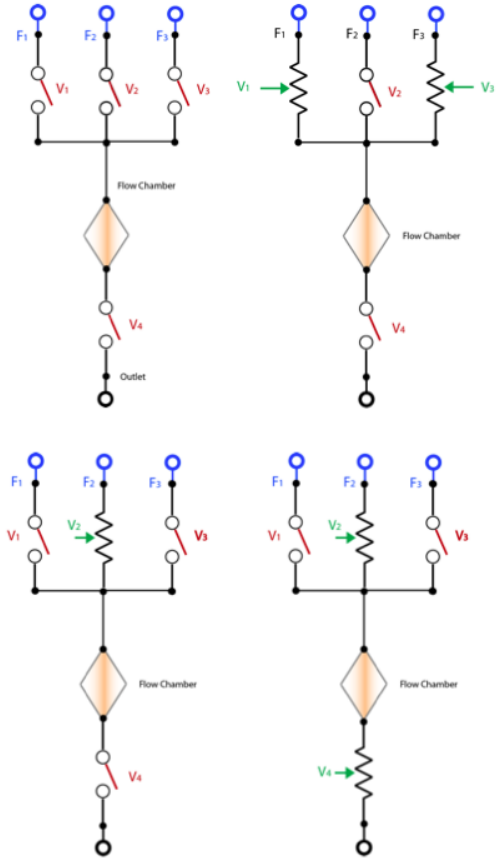

	Name	F1	F2	F3	v1	v2	v3	v4	Description
S21	Normal flow	always on			0	0	0	0	*3 laminar flow streams, 1:1:1 distribution*
S22	left off				1	0	0	0	*2 laminar flow streams, stim:media distribution*
S23	center off				0	1	0	0	*2 laminar flow streams, media:media distribution*
S24	right off				0	0	1	0	*2 laminar flow streams, media:stim distribution*
S25	flow off				1	1	1	0	*prevents fluid from entering*
S26	outlet off				0	0	0	1	*prevents fluid from exiting*
S27	left only				0	1	1	0	*contents of left stream*
S28	center only				1	0	1	0	*contents of central stream*
S29	right only				1	1	0	0	*contents of right stream*
S30	all stop				1	1	1	1	*All valves turn on, prevents any backflows*

	Name	F1	F2	F3	v1	v2	v3	v4	Description
S31	shift left	always on			0.5	0	0	0	*3 laminar streams, 0.5:1:1 distribution*
S32	shift right				0	0	0.5	0	*3 laminar streams, 1:1:0.5 distribution*
S33	expand				0.5	0	0.5	0	*3 laminar streams, 0.5:1:0.5 distribution*

	Name	F1	F2	F3	v1	v2	v3	v4	Description
S34	focus	always on			0	0.5	0	0	*reduced central pressure = narrow central stream (1:0.5:1 distribution)*
S35	focus left				1	0.5	0	0	*reduced central pressure + v1 on = 2 laminar streams, 0.5:1 stim:media*
S36	focus right				0	0.5	1	0	*reduced central pressure + v3 on = 2 laminar streams, 1:0.5 media:stim*

	Name	F1	F2	F3	v1	v2	v3	v4	Description
S37	focus	always on			0	0.5	0	0	*reduced central pressure = narrow central gradient*
S38	focus left				1	0.5	0	0	*reduced central pressure + v1 on = narrow gradient left to right*
S39	focus right				0	0.5	1	0	*reduced central pressure + v3 on = narrow gradient right to left*
S40	slow flow				?	?	?	0.5	*reduces overall flow rate through device (applied to any of the D5+D8 states)*

Figure 3.9: **Driven device descriptions.** A) Device layouts for I. Basic, II. Peripheral, and III / VI Central subclasses of device type. B) Base state table and supplemental tables for subclass-specific functions. All driven devices share the base device states S21 to S30. In addition, driven devices also inherit the device states of their passive analogs. (Figure 3.8

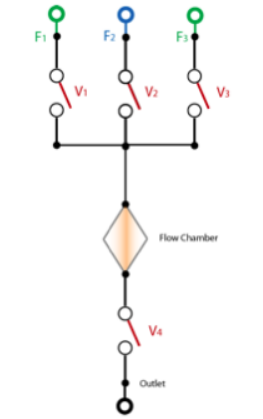

	Name	F1	F2	F3	v1	v2	v3	v4	Description
A1	Normal flow	1	1	1	0	0	0	0	*3 laminar streams, 1:1:1 media,stim,media distribution*
A2	Dynamic	?	?	?	0	0	0	0	*3 laminar streams, variable distribution, media:stim:media*
A3	Left_dyn	0	?	?	1	0	0	0	*2 laminar streams, variable distribution, stim:media*
A4	Right_dyn	?	?	0	0	0	1	0	*2 laminar streams, variable distribution, media:stim*
A5	All off	0	0	0	1	1	1	1	*all valves closed, device sealed*
A6	Flow off	0	0	0	1	1	1	0	*prevents fluid from entering*
A7	Outlet off	0	0	0	0	0	0	1	*prevents fluid from exiting via outlet*

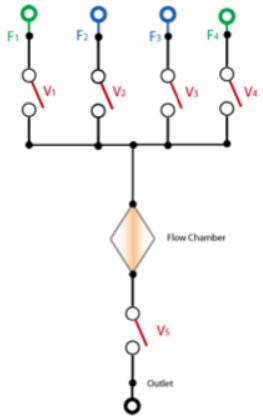

	Name	F1	F2	F3	F4	v1	v2	v3	v4	v5	Description
A1	Normal flow	1	1	1	1	0	0	0	0	0	*4 laminar streams, 1:1:1:1 media:stim1:stim2:media*
A2	Dynamic_1	?	1	1	?	0	0	1	0	0	*3 laminar streams, variable distribution, media:stim1:media*
A3	Dynamic_2	?	1	1	?	0	1	0	0	0	*3 laminar streams, variable distribution, media:stim2:media*
A4	Left_dyn1	0	?	0	?	1	0	1	0	0	*2 laminar streams, variable distribution, stim1:media*
A5	Left_dyn2	0	0	?	?	1	1	0	0	0	*2 laminar streams, variable distribution, stim2:media*
A6	Right_dyn1	?	?	0	0	0	0	1	1	0	*2 laminar streams, variable distribution, media:stim1*
A7	Right_dyn2	?	0	?	0	0	1	0	1	0	*2 laminar streams, variable distribution, media:stim2*
A8	All off	0	0	0	0	1	1	1	1	1	*all valves closed, device sealed*
A9	Flow off	0	0	0	0	1	1	1	1	0	*prevents fluid from entering*
A10	Outlet off	0	0	0	0	0	0	0	0	1	*prevents fluid from exiting via outlet*

Figure 3.10: **Dynamic device descriptions.** A) A single-inlet dynamic device. This device is capable of constant switching between hydrodynamic targeting, expansion, and focusing. B) A two-inlet dynamic device. Extending on the capabilities of the single-inlet device, the two-inlet can arbitrarily switch chemical cues and boundary positions throughout the course of an experiment.

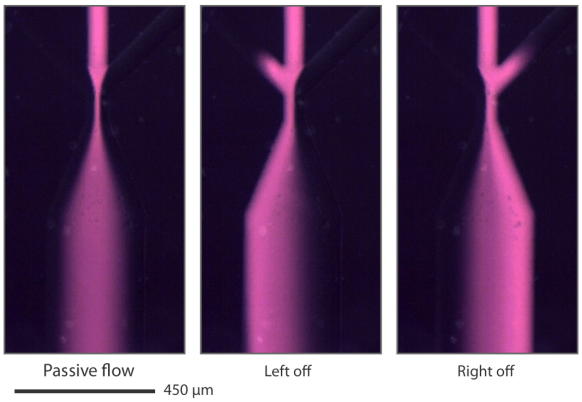

Figure 3.11: **Passive gradient generation** Three flow states in a passive device with binary control.

Subclasses of passive devices are formed by adjusting the type of control mode for each valve. The most basic uses a binary valve configuration. This provides profiles created by the combination of one, two, or more of the possible inputs. Introducing dynamic valves at the periphery enables the device to selectively scale back one or both of the peripheral inputs. This in effect allows the device to expand the central laminar (targeting) stream. Unequal closure of the peripheral valves will also modify the center line of the central stream as defined by the midpoint between the left and right boundaries. This creates the targeting capability seen in the Folch IFR devices [102]. Moving the dynamic valves to the central laminar stream removes the precise control of the center line but adds the ability to scale the central stream from a fully-open to a fully-closed position.

Active devices Active devices rely on a constant hydrostatic pressure source to drive fluid flow through the device. The same subclasses present with passive devices are available for driven devices as well. The advantage of the driven devices lies in the ability to select between no flow, hydrostatic flow, or driven flow instantaneously. To facilitate this, the fluid reservoirs connected to the both input and output can select between atmosphere or constant pressure.

Dynamic devices represent a departure from the valve-mediated control scheme found in both passive and drive device classes. These devices implement a dynamic pressure source for controlling inputs directly while providing binary valving to maintain the temporal resolution advantage found in valve-based systems. No true subclasses exist within our current description of dynamic devices. The only variation exists in the number of discrete inputs bounded by the two dynamically driven streams.

Dynamic devices posses the greatest potential with regard to types of flow profiles possible. To harness that potential though, significant control mechanisms must be in place to continuously monitor the dynamic output and boundary positions. The bulk of the control system described later in this chapter was designed around these steep requirements.

When properly controlled, the dynamic devices are capable of producing an almost endless range of experimental profiles, including hydrodynamic targeting, stream expansion, stream focusing, and discrete pulse sequences with boundary repositioning between pulses. Increasing the number of discrete inlets provides a means to switch between multiple chemical cues mid-experiment.

3.2.5 Device fabrication

To fabricate the three-layer design, a modified version of the Quake Laboratory MSL protocol was used [103]. Two fabrication methods were needed to ensure proper valve function at high control pressures. First, a positive resist with low reflow temperature was used. The resist was reflowed post-exposure to produce rounded channels needed for complete valve closure. Second, a ratio-metric method of PDMS mixing and bonding was applied to create a high-strength PDMS-to-PDMS bond between the individual layers. The interlayer bounds were test and found to hold a 40 PSI pressure reliably over a one-week time span.

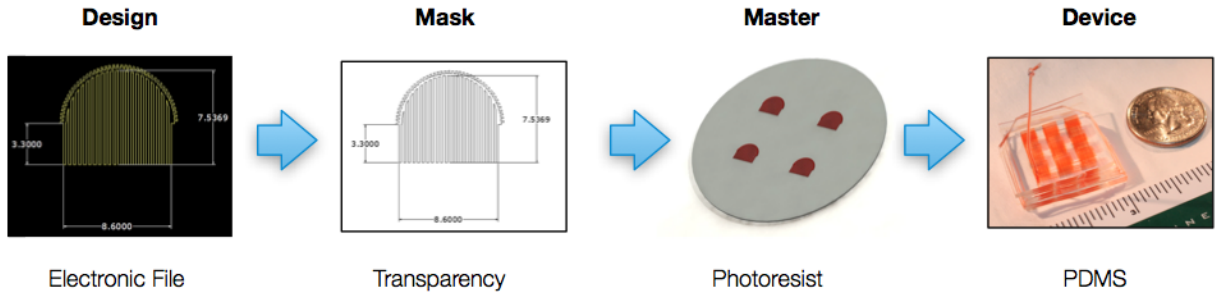

Figure 3.12: **Multilayer fabrication process.** Four steps comprise the standard fabrication method used for most PDMS-based microfluidic devices. A) The design is first created using CAD software. B) The design is transferred to a transparency using a high resolution printing process to create a UV mask. C) Photoresist is spun on a silicon wafer and developed using the UV mask to create a device master. D) PDMS is poured onto the master to produce a relief of the channel features. This is then bound to a solid substrate such as glass or another layer of PDMS.

Master fabrication Each design was drawn in CAD software (AutoCAD, Autodesk 2007) and printed at 20,000 DPI onto a plastic transparency through a third-party printing company. Device design parameters were based on the Stanford Microfluidics Foundry protocols [103]. The following additions were made to the design procedure to account for the high pressure and multilayer configurations eventually employed.

- Tolerance for 1 mm misalignment in any in-plane direction.
- Inlet locations placed with a minimum edge-to-edge distance of 3 mm.
- Inlet locations at least 3 mm from any device edge.

For the control and culture layer masters, SU-8 3025 negative photoresist (MicroChem) was spun onto 3"" SI wafers with resist heights of 20μm and 65μm respectively. The wafers then underwent a soft-bake at 95°C for 25 minutes before masked UV exposure. Following exposure the wafers underwent a post-exposure bake at 95°C for 10 minutes. Each master was developed using non-dilute Su-8 Developer, washed with isopropanol, and hard-baked at 150°C for 120 minutes. The completed masters were then left to cool overnight and stored in a dry, dust-free environment.

The flow layer masters were fabricated from AZ-4620P positive photoresist (Ellsworth Chemical). Resist was spun on to a 3-inch SI wafer producing a layer 15um thick. The wafer was then baked using a ramped temperature profile from 65°C to 115°C over 10 minutes. The resist was allowed to cool to room temperature before masked UV exposure. The master was then developed using a bath of AZ 1:4 developer/water solution (Ellsworth Chemical) over 10 minutes. The resist edge bead is be removed manually to provide a smooth edge around the circumference of the wafer. After rinsing with de-ionized water, the master was hard-baked using a ramped temperature profile from 65°C to 190°C, increasing at 10°C/hour. The hard-bake will cause the AZ resist to reflow into the rounded geometry necessary to produce the complete push-down valve structures needed for the designs. The flow layer master was then silanized with a 30 minute exposure to TFOCS (Sigma) vapor in a chemical hood to passivate the surface in order to prevent undesired bonding between PDMS molds and the photoresist during future device fabrication steps.

PDMS device fabrication Each microfluidic device was fabricated from polydimethylsiloxane (PDMS), a two-part pre-polymer:crosslinker mixture (GE RTV 615a/b) shown to have excellent biocompatibility and structural properties for cell culture applications [36]. The fabrication process consisted of four steps. For step 1, two separate ratiometric mixtures of RTVa and RTVb compound were used. For the control layer, a 1:5 ratio of a:b was used while a 1:20 ratio of a:b was used for the flow layer. The mixed PDMS was then degassed before being poured onto each respective master. The flow layer was spun at 2000 rpm for 30 seconds to create a 20um layer. Both layers were then baked at 80°C for 35 minutes providing sufficient time to set. The control layer was then removed from the master and inlet holes were punched using a sharpened 20Ga dispensing needle. The punched control layer was then placed on to the flow layer, still on the wafer, using the internal features to align the layers. A weight was placed onto the two-layer complex and the device is then allowed to bake for another 180 minutes at 80°C.

Two hours into the bake process, PDMS for the culture layer was mixed using a 1:5 ratio of a:b compounds. After degassing, the PDMS was poured onto the culture layer master and allowed to bake at 80°C for 35 minutes. Once both bake steps had completed, the combined two-layer device was lifted from the stimulation layer master. Inlets for the seeding and stimulation layers were punched using the 20 Ga needle. The culture layer PDMS was then removed from the master. The two-layer complex was aligned with the inverted culture layer and placed onto a glass cover slide. A weight was again placed onto the final three-layer device before baking for a final 24 hours at 80°C. Once complete, the device was placed in a sterile culture dish and stored for future use.

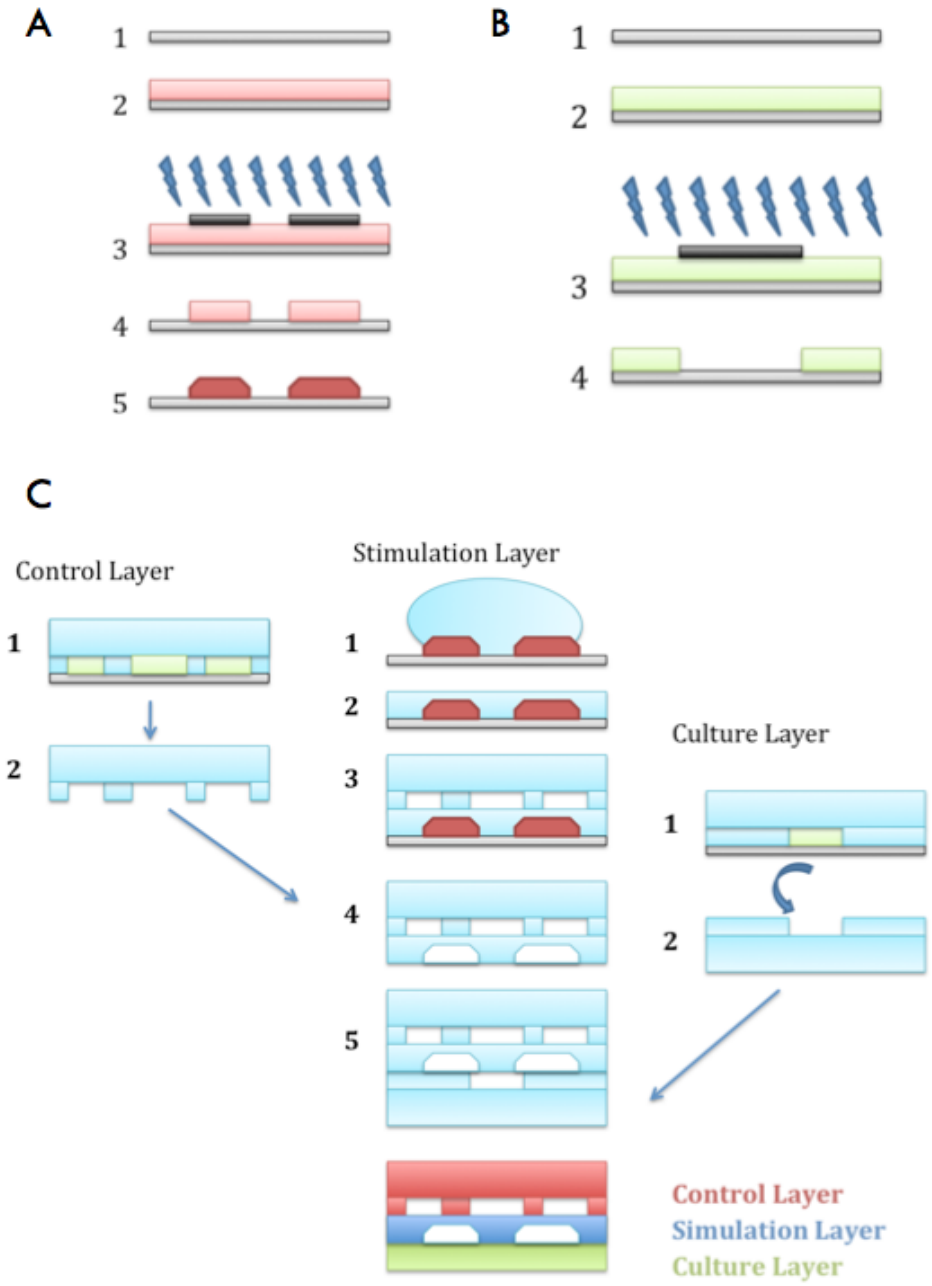

Figure 3.13: **Multilayer soft-lithography fabrication steps.** A) Fabrication of the flow layer master using a positive photoresist. B) Fabrication of the control and culture layer masters using a negative photoresist. C) PDMS fabrication and assembly of a complete three-layer MSL device.

3.2.6 Control platform

Pressure control hardware and feedback To control the microfluidic device state and integrate multiple sources of feedback, a complete hardware and software platform was developed. The platform based on the Quake 24-valve digital controller [103] and extended to incorporate two dynamic pressure controllers. Real-time image analysis and pressure feedback components were also integrated. Off-the-shelf components were integrated with a custom PCB and linked to a National Instruments USB DAQ for data I/O.

- 8 binary high pressure sources (35 PSI)
- 8 binary low pressure sources (10 PSI)
- 2 dynamic pressure sources (0 - 30 PSI)
- High pressure sensor for high pressure source (0 - 100 PSI)
- Low pressure sensor for low pressure source (0 - 30 PSI)
- Pressure sensors for dynamic pressure sources (0 - 50 PSI)
- Video and still image capture of boundary position

The platform configuration incorporates all design features above into a single platform with shared information and power buses. Starting from the microfluidic device itself, fluid lines run to sealed reservoirs containing the fluid of interest. Each reservoir is then connected to the appropriate valve according to the valve table for the specific microfluidic device design. This is the final parameter necessary to describe a device configuration, as mentioned in above.

Each valve is independently controlled using the digital controller previously described [103]. The digital controller interfaces directly to a PC via a USB interface. For dynamic pressure sources, electronic pressure controllers (EPC, Parker Microfluidics) were placed between the fluid reservoirs and the binary valves to control final inlet pressures. Control of the EPC handled with a National Instruments data acquisition device furnishing binary and analog I/O. Finally, piezoelectric differential pressure sensors are used to sample the valve and driving pressure sources and pass the data to the PC through the NI device.

Software configuration and task-based design Custom software was written to interface with the hardware platform and perform data analysis. The user interface and application logic were written in Visual C# using the Microsoft .NET 3.5 framework. Multiple open-source libraries were used to handle hardware I/O (.NET serial libraries), real-time image analysis (Intel OpenCV and EMGU OpenCV C# wrapper), graph presentation (Microsoft Chart library), statistical analysis (Microsoft Office COM interface), and state management (.NET XML parsing and serialization libraries). Figure 3.14 shows the user interface with functional regions labeled.

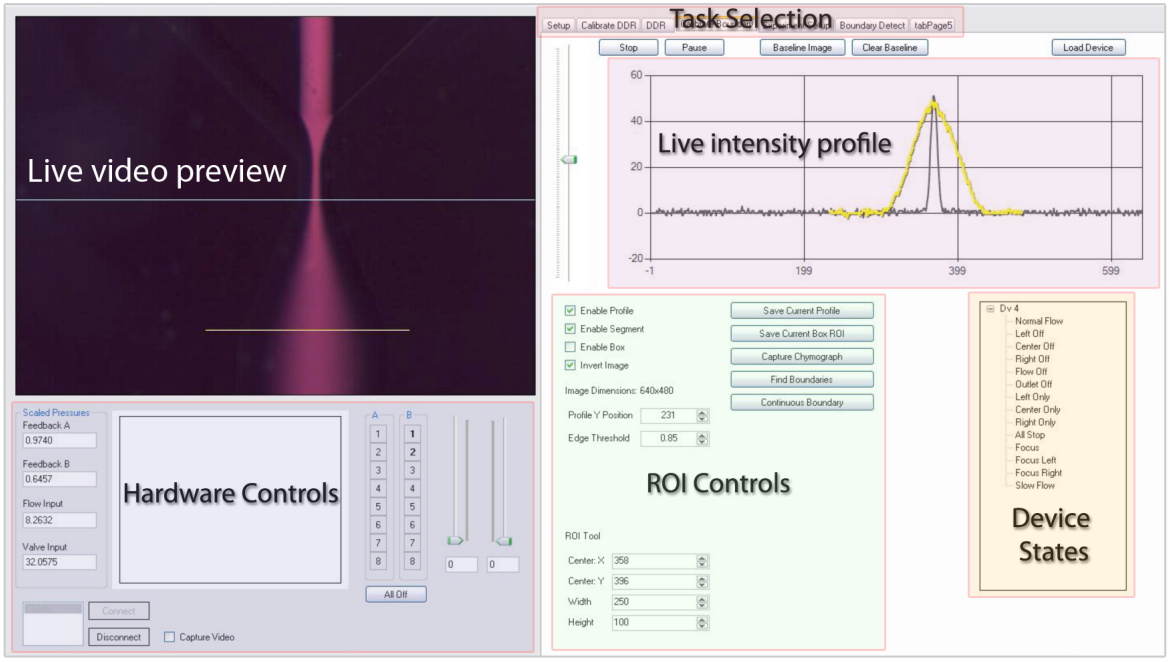

Figure 3.14: **Profile measurement user interface.** The user interface displays a live view of the video source. During analysis, line overlays show the sample location to produce the intensity profiles on the right side of teh interface. The yellow bar defines the ROI and can be moved to targets of interest with a mouse click. Static and dynamic data outputs are listed in the Analysis options. Available device states are loaded on application start and can be toggled between directly.

A task-based design was employed to generate the user interface and determine which variables are exposed to the enduser. Starting with an end goal, each task was defined in terms of what information needed display, interaction, and the type of output desired. Task-specific data displays are embedded into tabs within the user interface. Shared classes such as the analysis or data acquisition class are accessible through the user interface main class. Direct device control is available but protected variables have been implemented within classes ensure that the actual device state remains stable.

Data collection of raw images, two-dimensional intensity profiles, and full color chymograph generation were automated in separate tabs within the user interface. Data collection was integrated into the experimental design, combined control of device state and data collection concurrently. In addition, real-time two-dimensional intensity

profile calculate and thresholded boundary detection were implemented as add-ons to the live video display within the interface itself. All collected image data was collected within the analysis class and stored for future processing.

3.2.7 Device characterization

A series of experiments were performed to characterize the platform's ability to generate arbitrary flow profiles with high repeatability and precision. The first set of experiments covers profile generation and state-to-state transitions. The second set of experiments introduces time-based elements for characterization.

Profile generation Two measures of flow profile generation are important for the design of future biological experiments: how closely the generated flow profile corresponds to the prescribed profile, and how repeatable the generated profile is over consecutive presentations.

To address the former, we created an arbitrary boundary task where the lateral position of a laminar boundary was defined a priori. This position was then converted into controller-compatible driving pressure values and replayed through the microfluidic hardware. A region of interest was defined prior to experiment start to generate an intensity-based chymograph of the replay.

To address the repeatability question, we created an arbitrary replay task where the device was instructed to switch between 2 flow states automatically every two minutes over 100 trials. Midway through each profile, a two-dimensional intensity profile was collected autonomously. First, last, mean and confidence intervals for the flow profiles were then compared.

Temporal control The capabilities of the platform presented here afford the ability to control both binary and continuous valve states within the same PDMS device and control configuration (Active / Passive devices).

To characterize the utility of this component, we first developed a task to trigger rapid pulses of a targeted stream. As with the previous characterization experiments, we utilized autonomous data collection to record two-dimensional intensity profiles and a continuous chymograph.

Finally, to demonstrate the integrated binary and continuous control of the internal device state, we developed a task for the temporally-controlled presentation of a targeted stream to isolated regions of a mock culture environment. To accomplish this task, a sequence of stimuli stream positions were defined prior to the experiment. During the experiment, the peripheral streams were positioned to generate the correct boundary positions. A binary valve state was triggered to start and end the stimuli presentation. The peripheral streams were then repositioned by the control system and the process was repeated for the remaining steps of the experimental sequence. Two-dimensional intensity profiles and chymographs were generated throughout the course of the experiment. Real-time boundary positions and stream locations were recorded for future analysis.

3.2.8 Results

Profile generation The arbitrary boundary experiment was performed with user-generated positions with a Matlab script. Figure 3.15 (left) shows the stages of the boundary experiment. The curves represent boundary positions over time (X values). The top-most curve shows the user-generated input from Matlab passed to the control platform. The middle figure shows the chymograph generated by the software interface sampled at 30 frames per second. The bottom figure shows the position of the input profile overlaid onto the normalized boundary found from a thresholded-boundary detection algorithm. The input and generated curves show good correspondence across the range of positions, with minor errors present at sharp transitions.

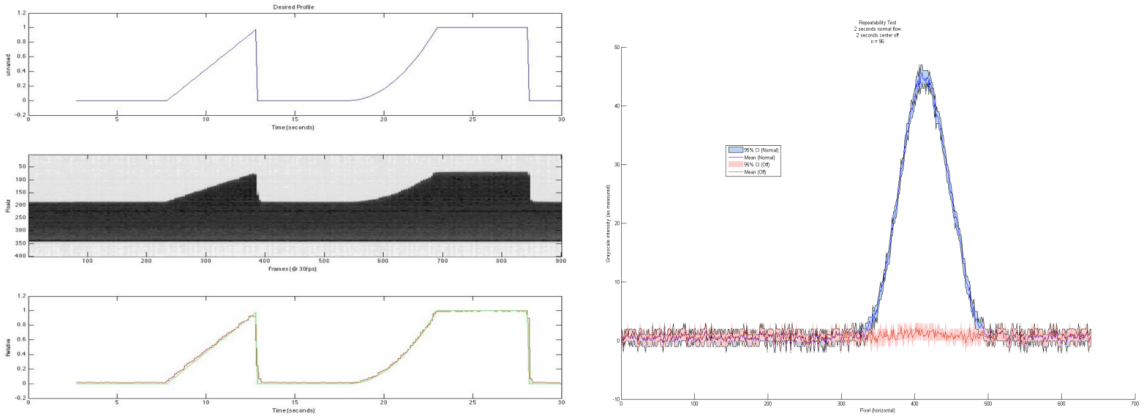

Figure 3.15: **Profile generation and repeatability** A) Input profile, raw chymograph, and normalized comparison between slow (5 second) boundary paths. B) Flow profiles with 95% confidence interval. Data was generated automatically through software available in the analysis class.

The results of the repeatability task are pictured on the right side of Figure 3.15. The two-dimensional intensity profile was collected midway through the two-second stimulus. 95% confidence intervals were calculated in Matlab and plotted for their respective flow profile. Additionally, the first, last, and mean flow profile were plotted to demonstrate minimal drift across trials. The data collected show a high degree of repeatability across flow state changes.

Temporal control A series of experiments were designed to presented complex sequences of repeated stimulus pulses to specific regions of interest. Figure 3.17 shows full color chymographs collected during the replay of a series of experiments created to selectively target user-defined regions of interest with arbitrary order and duration. Detail views of each stimulus are provided along side of the overall experimental presentation. Data was sampled at 30 frames per second. Experiments presented here lasted from 90 to 100 seconds total, producing 3000 frames of information.

The top-most image in Figure 3.17 shows an ordered presentation of a dyed stream to four discrete lanes $(1 \rightarrow 2 \rightarrow 3 \rightarrow 4)$ within the flow chamber. Notice there are discrete bolus of stimuli with no connection between, indicating full isolation of specific areas within the chamber. The four lane positions were defined prior to the experiment and are not fully equivalent in lateral coverage. This is addressed in the discussion.

The central region in Figure 3.17 shows an experimental sequence with unordered presentation$(1 \rightarrow 2 \rightarrow 3 \rightarrow 4 \rightarrow 2 \rightarrow 3 \rightarrow 1)$. Note here the duration the stimuli are equal. Finally, the bottom region of Figure 3.17 shows an experimental sequence with unordered presentation, varied stimuli duration.

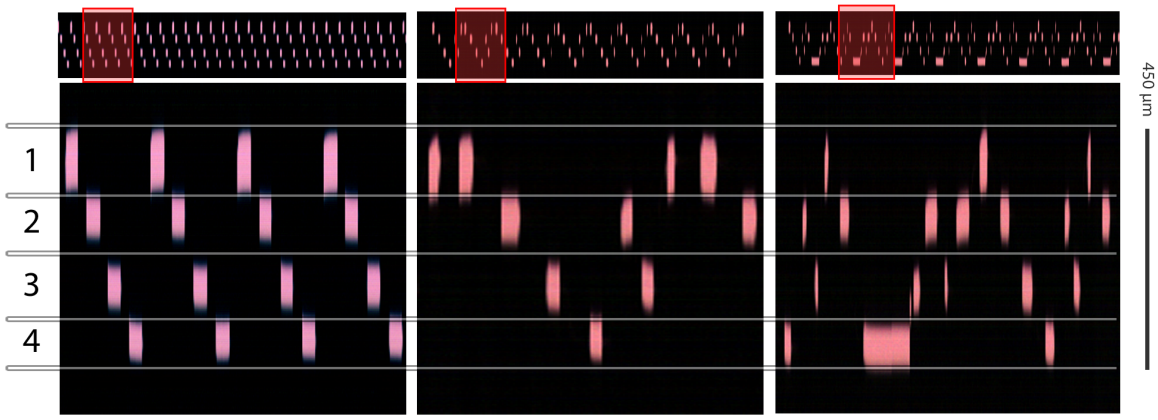

Figure 3.16: **Chymographs of Targeted Streams** Overall (top) and detailed (bottom) chymographs from three experimental sequences performed on the same device. The first (left) sequence contains an ordered presentation of evenly distributed pulses. The second (middle) sequence modifies the order of the stimulus presentation. The third (right) sequence demonstrates an unordered stimuli presentation with varied duration.

Figure 3.17 shows a sequential series of frames from a dynamic experiment with the real-time boundary detection and tracking enabled. A dyed central stream was targeted to different regions of the flow chamber similar to the profiles presented in Figure 3.15. The boundary detection was performed at the blue line located in the lower portion of Figure 3.17. A 85% intensity threshold was used to detect the left and right bounds of dyed stream (red lines). The midline (pictured in blue in the figure) is the average lateral position between the two bounds. The custom ROI (yellow) line was not used in this replay.

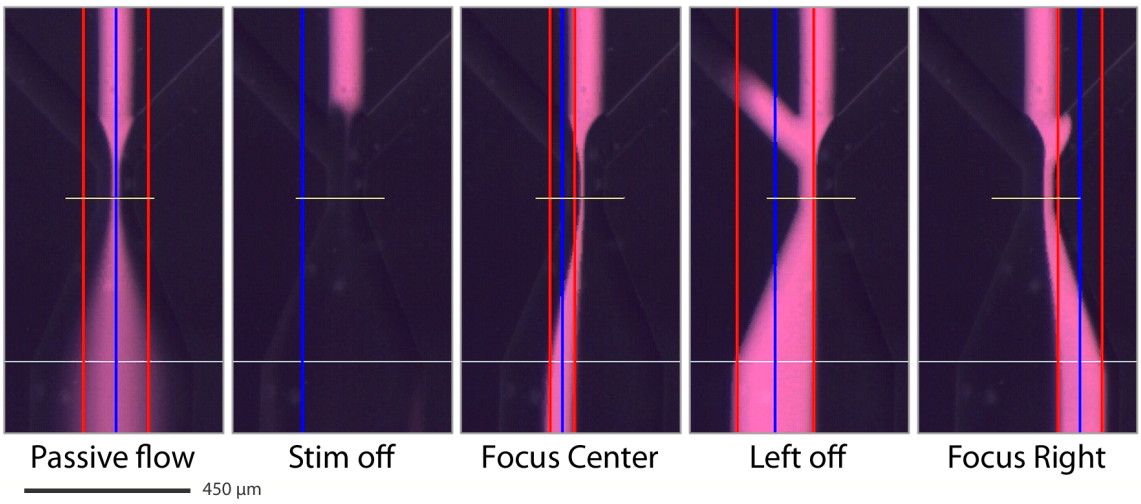

Figure 3.17: **Real-time boundary detection and stream tracking** Frames from raw video captured by the user interface. Boundary detection, based on intersections at the blue line located at the bottom of each frame, is overlaid onto the live video feed. Left and right boundaries are labeled by solid red lines with the stream midline labled by a solid blue line. In the "stim off" frame, the midline is free as no boundaries are found.

3.2.9 Discussion

Here we describe and characterize a novel microfluidic platform that incorporates existing microfluidic device features with a novel valve implementation and control system. The platform provides researchers with an accessible user interface to arbitrary profile generation and data collection for a large group microfluidic device designs. The platform interacts with a multilayer microfluidic device based on existing devices for cell culture. From characterization experiments we have shown arbitrary flow profile generation with high repeatability and control. In addition, we have demonstrated a working proof-of-concept real-time boundary detection and stream tracking implementation. Additional experiments must be performed prior to routine biological operation, focusing on seeding and media replacement protocols [108]. The source code for the user interface, device descriptions, statistical analyses, and real-time boundary detection will be made available online for redistribution. System performance measures such as valve closing and opening response time, pressure sensor resolution, and video capture rate are dependent upon hardware used. 500 millisecond response times and 100 second experimental durations were chosen to meet our future laboratory's needs.

3.3 SPECIALIZED MICROFLUIDIC DEVICES FOR NEUROSCIENCE

Long-term culture of dissociated neurons has been demonstrated in both open and sealed microfluidic device designs. Neuronal biocompatibility of PDMS-based microfluidic devices increases following autoclave sterilization [72]. ECM-derived proteins are perfused into devices prior to initial cell seeding, further increasing the biocompatibility of the culture chamber. Proteins such as fibronectin, laminin, and poly-lysine promote cell adhesion and neurite extension [52]. Attention is paid to ensure even protein distribution as non-uniform gradients will introduce unwanted guidance cues. Protocols for neuronal harvest, seeding, and characterization are being developed concurrently by other members of the Zeringue Research Group to create a foundation to begin cellular experiments [3, 73].

3.3.1 Research approach

One area that remains beyond the scope of current technologies is the precise focal long-term stimulation of sub-cellular regions of shear-sensitive cells such as neurons. Neurons react to both their chemical and physical extracellular environment, however as previous studies have demonstrated, neurons possess a greater sensitivity to shear stress than most other cell types. In a low shear environment, neuronal projections have been shown to minimize their shear state by orienting to the flow direction. At slightly higher shear levels, neurites will retract completely and discontinue future projections [48]. Attempting to employ a focal microfluidic device to selectively target the axon or dendritic region will produce the unwanted shear affects, preventing effective study. Gradient devices have been used successfully for neuronal culture but sacrifice stimulation precision by using reduce flow speeds and larger culture volumes [48, 111, 50].

The research plan presented here directly addresses the limitations inherent in using hydrodynamically focused devices for neuronal stimulation. We have proposed a new microfluidic conceptual design that enables highly focused fluid streams for shear-sensitive cellular applications. Two prototypes have been designed to demonstrate biological proof of concept based on current model systems in developmental biology and axon guidance. From the development and characterization of the system, three technological innovations will be described and demonstrated for future microfluidic devices.

The primary technological advancement results from the combination of hydrodynamic focusing, described above, and lid-driven microfluidic flow over a high-aspect ratio gap. The concept demonstrated will produce highly focused laminar streamlines over of a shear-sensitive region of cell culture. The design restricts lateral diffusion while permitting vertical diffusion, allowing for precise spatial delivery of chemical stimulant to selected regions of the culture. This concept will enable researchers to address cellular chemotaxis and axonal guidance questions while minimizing shear-based signaling effects.

A microfluidic concept was developed to address two central design objectives. The first objective, described previously, controls the position of a focused hydrodynamic stream using compact internal features. The second design objective to present the focused stream across a cell culture environment over a long experimental duration

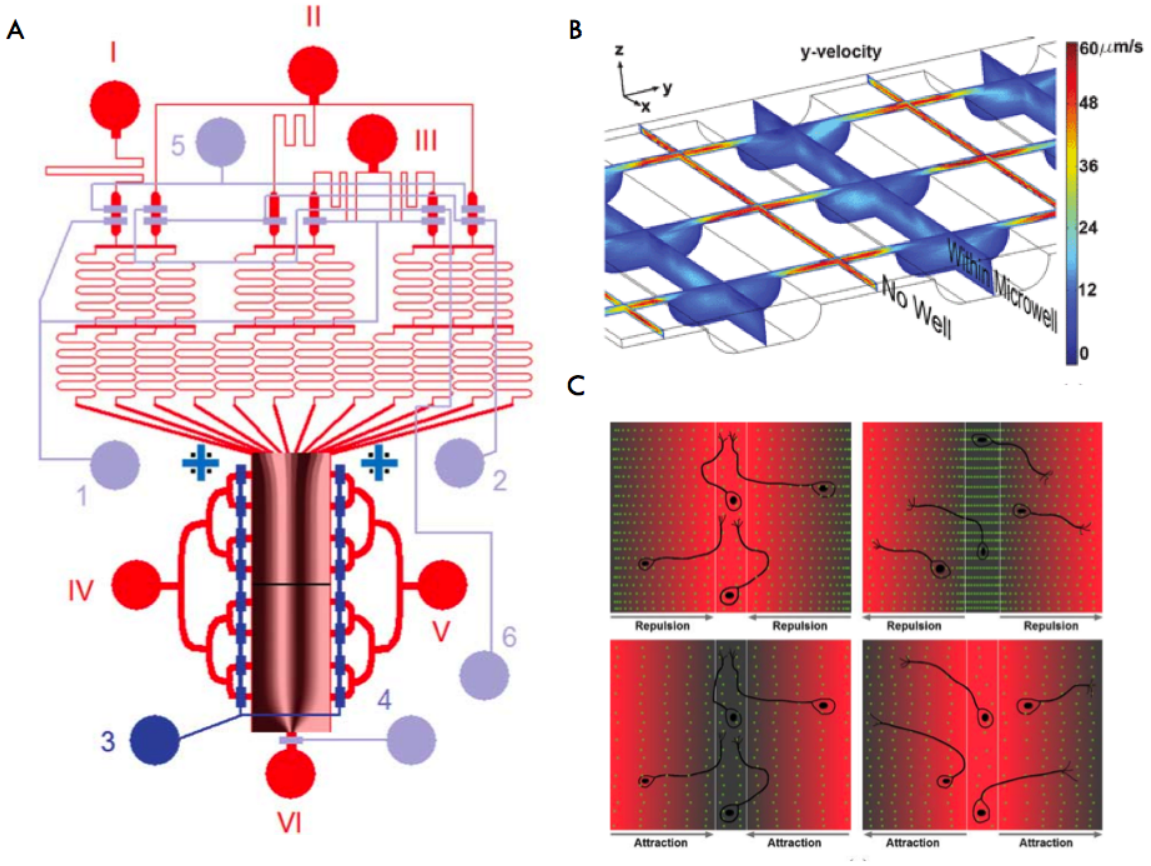

Figure 3.18: **Specialized devices for neuroscience.** Developed by Wang et. al. in 2008 [48], this multilayer microfluidic device provides high spatial and temporal control of a bimolecular stimulus presentation. A) Schematic of the device. Flow inlets and outlets are pictured in red. Valve inlets are pictured in blue. B) Etched glass microwells provide the base surface of which the PDMS layers are bonded to. The microwells create a regional expansion, lowering fluid velocities via the Bernoulli's relation. This reduces to level of shear stress seen by the neurons growing on the bottom. C) Diagram of the biomolecular gradients produced from surface (laminin) and diffusible (BDNF) cues. Due to flow velocities inside of the device, sub-domain stimulation of neurons is not available.

without subjecting the cells to detrimental amounts of shear stress. To satisfy the first device objective, a novel microfluidic design was developed around the existing microfluidic concepts of deformable internal geometries and variable flow resistances inside of a device.

3.3.2 Lid-driven flow generation

The second design objective was addressed by pairing the dynamic valve configuration established above with a third fluidic layer. The third layer, referred to as the culture layer, contains a specific gap geometry that produces a shielding effect for cells grown inside the device. Investigators have demonstrated in simulation and experiment the presence of lid-driven flow over gaps containing a minimal feature aspect ratio [54, 96]. As feature geometries exceed the critical ratio for a given flow velocity, vortices form within the gap itself. Due to the laminar nature of the flow itself, the vortices originate from standing potentials rather than boundary layer separation. The benefit of such a configuration is the isolation of cells from the direct fluid streamlines and in doing so reduction of shear stress exposure by several fold [48, 54, 56].

The degree of shear exposure is directly linked to the amount of substrate confinement in a focused hydrodynamic stream. As shown previously, decreased flow rates result in longer interfacial time and therefore increased lateral diffusion extents, reducing the effective minimum resolution of the targeting stream. In combination with the lid-driven flow geometry it is possible to maintain high flow rates with little change in the shear environment felt by cells in the culture layer. The lid-driven flow permits passive vertical diffusion of the substrate while maintaining a highly-contained stream with minimal lateral diffusion for targeted delivery. A downfall of this approach appears in the difference between inlet concentrations and actual delivered concentration as the majority of mass transport occurs via advection as the flow rates increase [56]. Therefore it is necessary to conduct appropriate transport simulations to determine the inlet concentrations necessary to achieve the desired effective concentration.

As shown previously, decreased flow rates result in increased lateral diffusion, reducing the effective minimum resolution of the targeting stream. In combination with the lid-driven flow geometry it is possible to maintain high flow rates with little change in the shear environment felt by cells in the culture layer. The lid-driven flow permits passive vertical diffusion of the substrate while maintaining a highly-contained stream with minimal lateral diffusion for targeted delivery.

To facilitate the study of within a lid-driven flow regime, the capability is needed to increase the volumetric flow rate while maintaining the relative driving pressure ratios. To accomplish this, we implemented a pressure-based feedback mechanism into both the device configuration parameters and the profile measurement interface.

The feedback mechanism samples the low pressure source value at runtime. This value becomes the normalized flow rate to which the peripheral dynamic pressures sources are scaled to. For an even 1:1:1 laminar distribution, the dynamic pressures are matched to the source. Reducing the low pressure source manually will reduce the peripheral sources equally, resulting in a constant profile for variable volumetric flow rates. To encapsulate this information, a flag that toggles between relative and absolute values within each device state table is maintained.

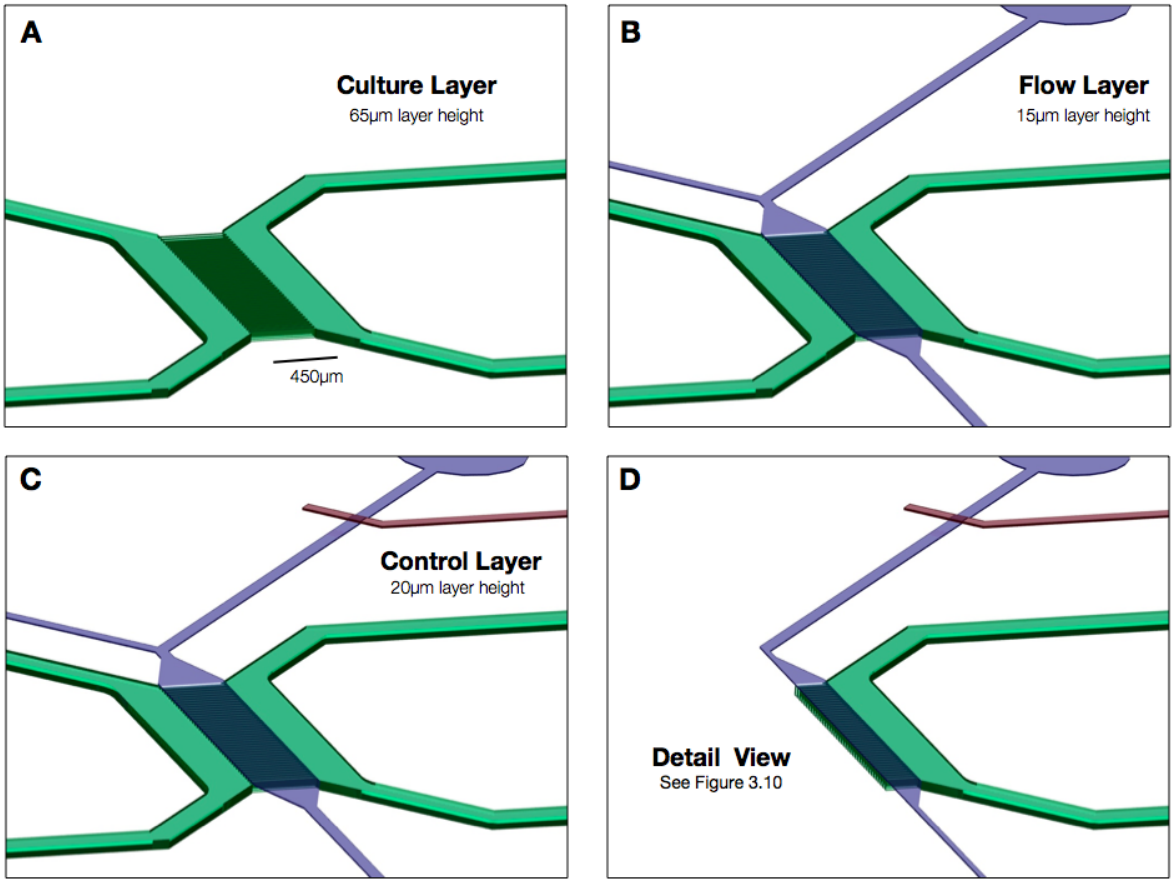

Figure 3.19: **Conceptual device fabrication.** The conceptual device consists of three distinct layers: Culture, Flow, and Control. The culture and flow layers share a fluid interface. The control layer sits above the flow layer and handles valve closure. All layers are sealed and ported to external reservoirs. A) The culture layer contains two parallel regions for neurons to grow in with a series of microchannels between to allow for neurite extension. B) The flow layer is aligned over top of the microchannels to produce gap-flow compatible geometry. C) The control layer is aligned over the flow layer to ensure valves will close fully. An alignment tolerance of 1mm is built in to the design. D) Slicing the model produces a cross-section of the gap-flow structures. Detail view is shown in Figure 3.20

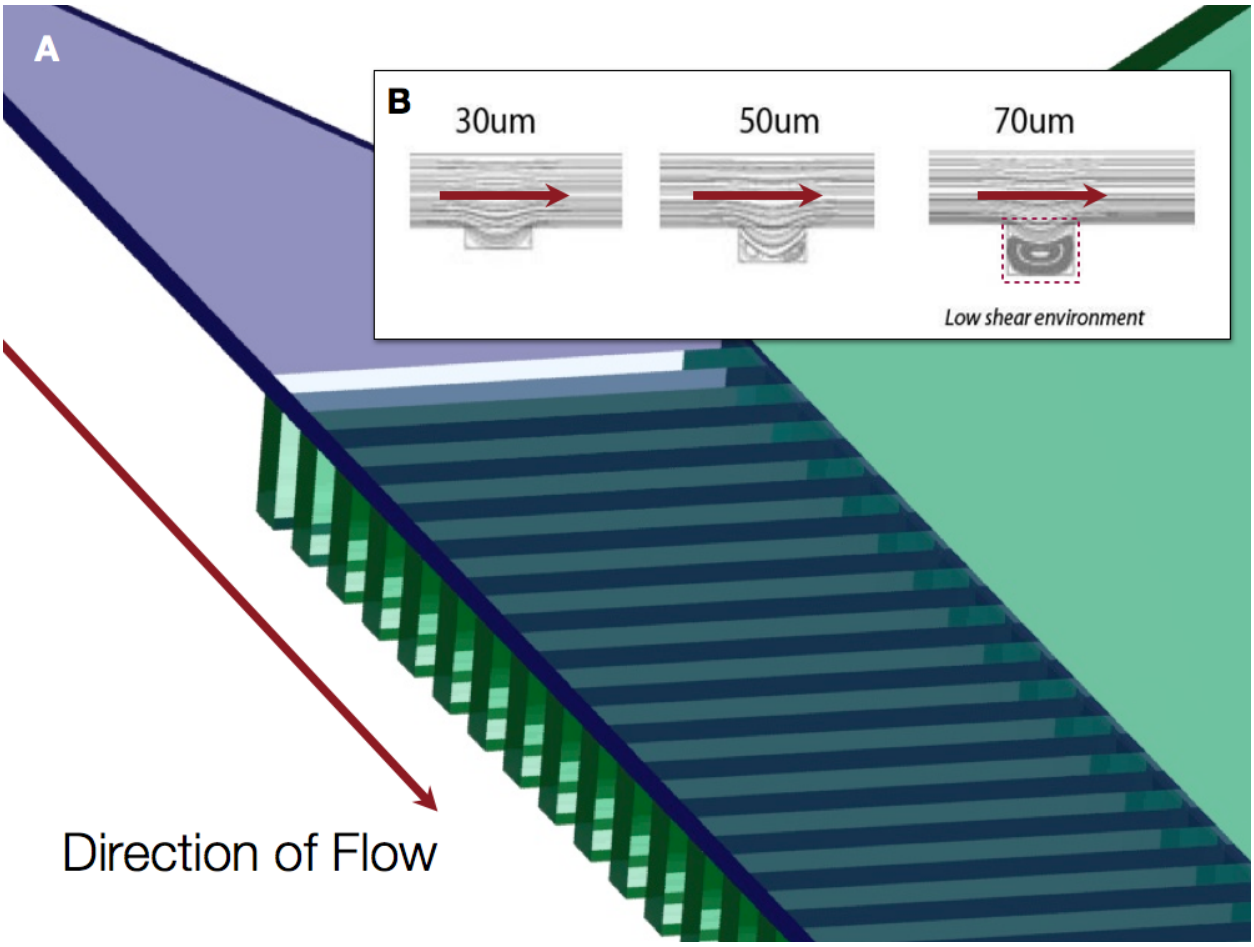

Figure 3.20: **Detail view of gap-flow structures.** A) As fluid passes through the flow layer (blue), a lid-driven flow regime will be produced across the culture layer (green) as long as the fluid velocity remains high. B). Prior work has established a model for the transition into the lid-driven regime for a given relative gap depth with respect to gap width that holds for the laminar flow regime found in microfluidics [84]

.

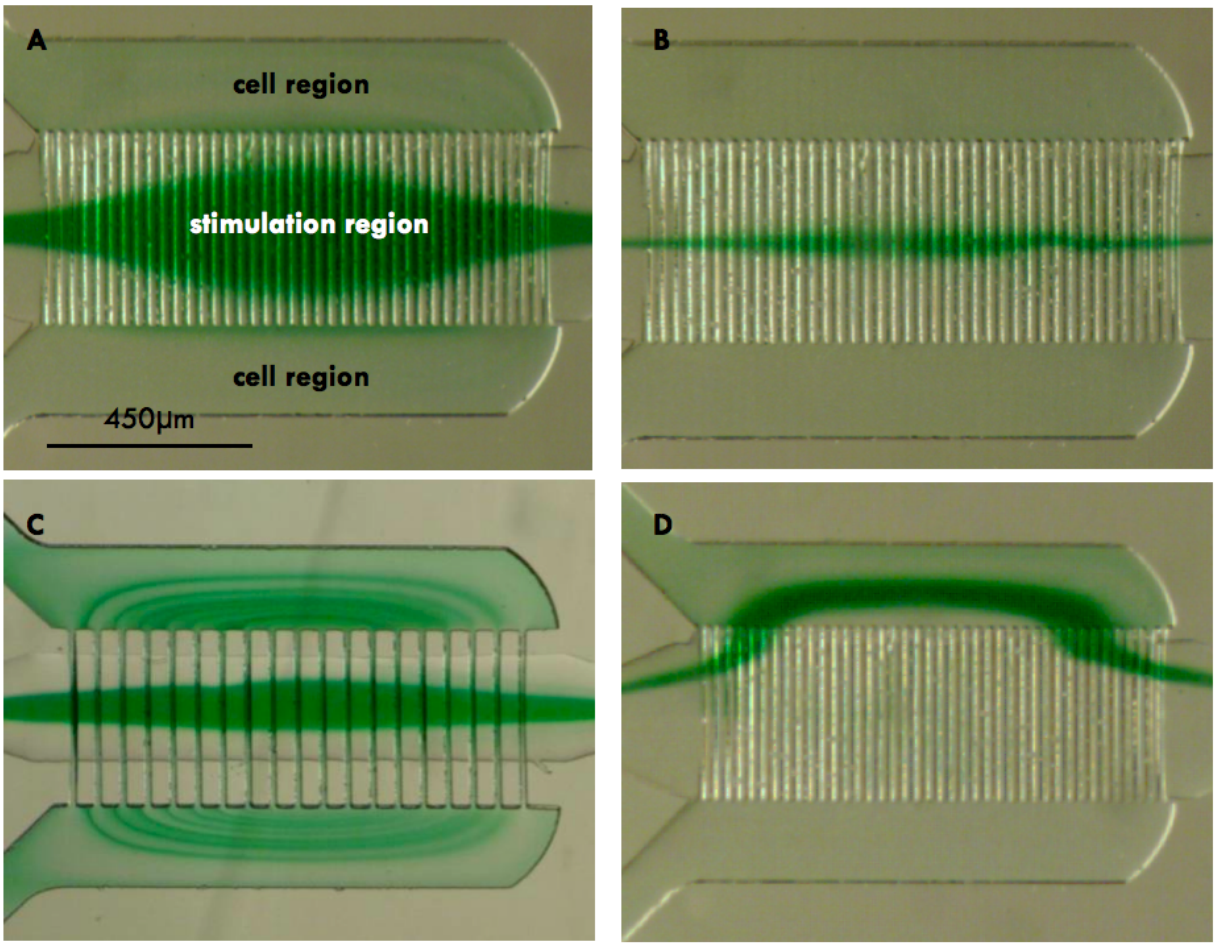

Figure 3.21: **Gap flow transition.** Images from a dynamic device with a green dye added to the central stream. A) Equally distributed flow over narrow gaps produces expansion. Trace amounts of the green dye from the central stream are visible at the periphery of each culture region. B) Expansion is minimized by using a focused stream. C) Unexpected radiant flow streamlines were produced with a modified gap spacing and flow layer width were used. D) Targeting stream into the culture area by adjusting the inlet pressure ratio.

3.4 INDIRECT FLOW RATE MEASUREMENT

Microfluidic devices provide precise control of the local microenvironment for cell culture applications [71] . Characterization and control of the parameters that define the microenvironment is necessary to reliably reproduce physiological conditions inside of a microfluidic device. Few controllable device parameters are readily accessible at experimental runtime. Volumetric flow rate is one such parameter that drives multiple environmental variables important to in vitro cell culture devices. Shear stress production, waste removal, and media renewal are directly related to the rate of fluid flow through a cell culture device [108]. In turn, volumetric flow rate can be controlled using a constant pressure source or syringe pump. It is important to monitor flow rate during an experimental protocol to ensure that the desired culture environment is maintained. Here we present a simple technique to monitor volumetric flow rate inside of a microfluidic device at runtime.

There are several common techniques to measure microfluidic flowrates. They fall into two general categories with respect to the experiment type: offline and online. Offline techniques are those that obtain/analyze flow rates prior to or following an experiment, typically requiring different conditions than the actual experimental conditions. Online measurement techniques utilize data collected during the actual experiment with flow rate determined either in real-time or shortly after.

Offline techniques typically have the benefit of very precise measurements that determine flowrates regardless of channel geometry and without the need for specific geometric assumptions (e.g. sidewall variations and fabrication defects are accounted for). One of the most common and reliable techniques is particle image velocometry (PIV) [90]. This technique uses the movement of small particles along fluid streams to determine flowrates. When taking consecutive images of a moving fluid, displacement of particles within the fluid can be analyzed. This technique gives precise information of fluid flow within the specific microfluid environment in question as well as different flow regimes within that environment that might deviate from ideal. Further, no a priori knowledge of the fluid environment is required to obtain fluid flow information, only particles that can be traced. Liquids commonly used in biological microfluidics (i.e. culture media) do not contain resolvable particles, meaning that this technique must be used separate from the actual experimentation or that traceable particles must be added to the culture media. Additionally, the computational requirements for PIV do not allow for easy real-time implementation without specialized computational hardware [114].

Online flowrate techniques often rely on control of a fluid source, such as a syringe pump or hydrostatic pressure head. Using microtubing and microchannel systems with syringe pumps can emphasize the variability in pressure created by the syringe driving mechanism that can reach above 20% pressure variations [92]. Even when an acceptable time-averaged flowrate has been determined, fluctuations above the average due to these variations can result in unacceptable shear stresses. Although, the long stabilization times associated with these setups [92] would not be a disadvantage for purposes of shear stress reduction. For controlling fluid flows in microchannel structures, pressure heads produce the most reliable and consistent flows. One problem with these setups is that the pressure drops across all of the components (microchannel structures, connective tubing, connections) must

be known. Typically the pressure drops are measured with expensive pressure gauges set up within the system throughout the experiment. This method works well if one is able to isolate the microchannels within the setup, but still requires specialized pressure-sensing equipment.

3.4.1 Theory and implementation

Our technique addresses the limitations inherent in current online systems to provide near real-time measurements of volumetric flow rate for arbitrary microchannel structures using equipment commonly found in most laboratories (computer, stereomicroscope, Firewire video camera). The method relies on automated video analysis of a sessile drop at the outlet of the microfluidic device. By observing the increase in drop volume over time, volumetric flow rates can be estimated throughout an experimental procedure while the microfluidic device is online. This technique is enabled by the presence of sessile drop shape variables that covary with the drop volume over a known volume range. These smooth mathematical relationships provide a means to infer drop volume from easily observable measures.

The shape of a sessile drop on flat surface is defined by the interaction between interfacial, atmospheric, and gravitational forces. Characterization of drop shape may include multiple parameters: Contact Angle (Θ) at the fluid-surface interface, Maximum and Contact Diameters (D_{Max}, D_c), Drop Height (H), and side profile, to establish a set of conserved measures across a range of drop volumes. The range is determined by the maximal height at which a sessile drop maintains a spherical shape with a circular contact region. At drop volumes that exceed this height, the magnitude of gravitational force overcomes interfacial tension to produce an asymmetric pool across the surface. The height at which this transition occurs is referred to as the critical height (H_{Crit}) [19]. Using numerical simulations or finite-element analysis, robust algorithms have been developed to estimate drop shape and volume with one or multiple parameters as input conditions [22, 40]. Importantly, the previous work completed in drop shape analysis enables us to put forth the assumption that, given a static contact angle and fluid viscosity, a smooth physical relationship exists between the maximum drop diameter (D_{Max}) and drop volume while the drop height (H) is below the critical height (H_{Crit}).

Following the assumption that a smooth relationship exists between maximal drop diameter and drop volume for given drop heights, it is then possible to determine an underlying representative equation by measuring the maximum diameter of fluid drops with known volumes. This process yields a calibration curve with which future drop volumes can be estimated for all experiments conducted with the calibrated device. Using this method, we are able to bypass the requirement for contact angle measurements and therefore eliminate the need for additional camera angles or equipment.

The complete analysis setup consists of three components: a microfluidic device connected to a fluid reservoir with an adjustable pressure source to drive fluid flows, a stereomicroscope with 1.3 Megapixel Firewire^{TM} video camera focused on the outlet port, and a PC running the analysis software. During each experiment, the pressure system is set to a specified value and turned on. Video frames are captured at 10 Hz and processed to extract the maximal drop diameter.

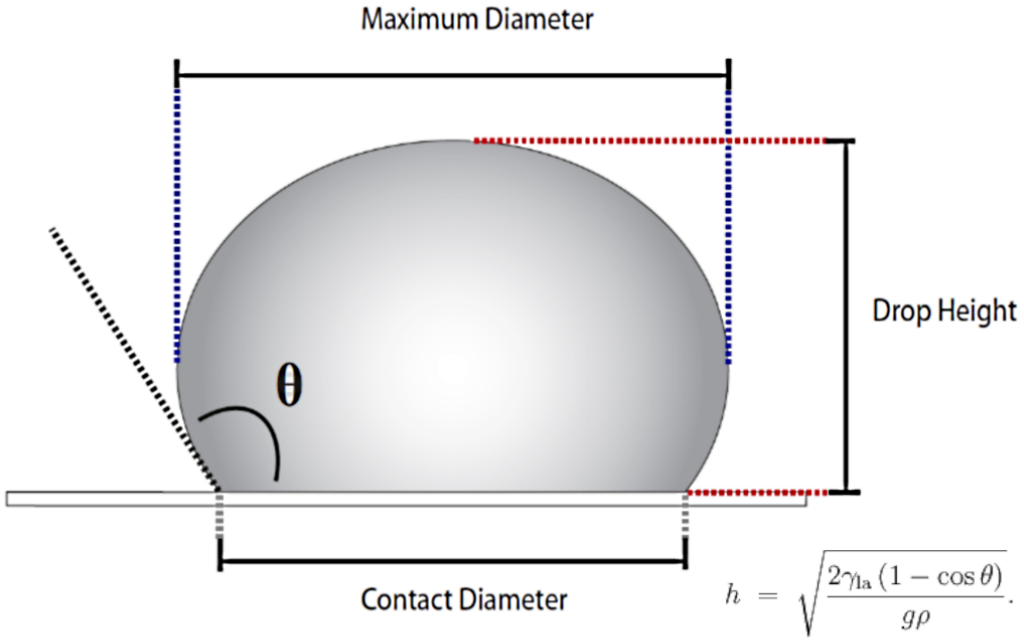

Figure 3.22: **Schematic of sessile drop:** Sessile drop shape may be characterized across one or more physical parameters, including Contact Diameter (D_c), Maximum Diameter (D_{Max}), and Drop Height (H). Contact angle (Θ) is determined by the fluid-surface interfacial forces and remains constant as drop volume increases. This angle is a product of the liquid being used, experimental atmosphere, and surface chemistry. For Θ less than 90 (degrees), indicating a wettable surface, D_c will equal D_{Max}.

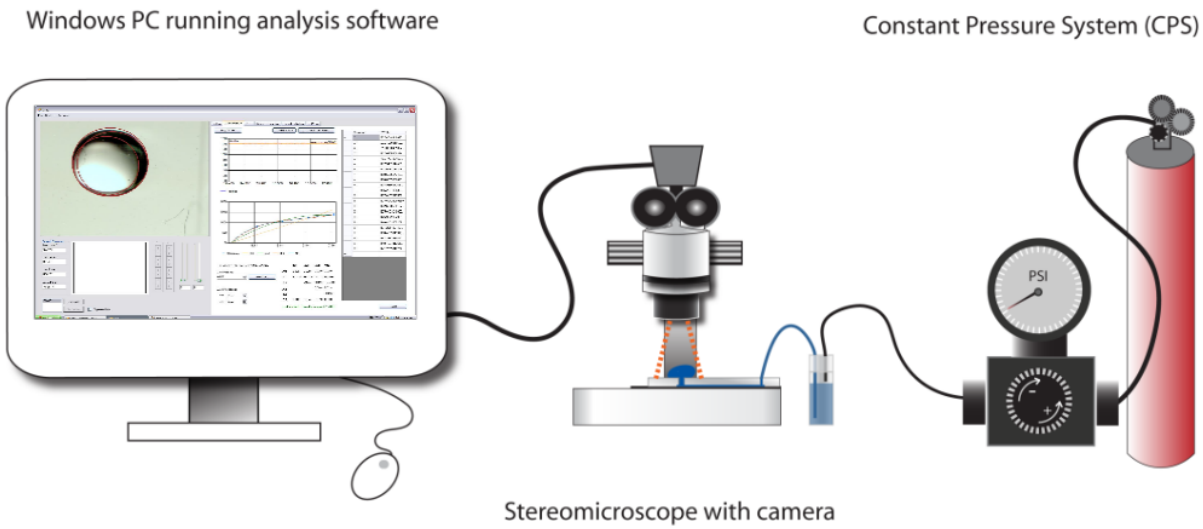

Figure 3.23: **Flow rate measurement experimental setup:** The stereomicroscope is used to visualize the microfluidic device through a firewire camera. The computer captures video from the camera and handles all processing of data through a custom software interface.

To accurately and repeatedly determine drop diameter, we have developed software to perform an automated image analysis sequence in near real-time from the live video source. The software, written in Visual Studio 2008 and running on a PC (1.8 GHz CPU, 2GB RAM), implements the Microsoft .NET 3.5 framework and the Intel OpenCV imaging library to handle image capture from the Firewireł video camera and subsequent analysis steps. Each video frame is filtered to reduce noise, converted to grayscale, and analyzed using a circular Hough transform [2] to identify the drop location and circular diameter. Independent analysis of each captured frame enables the software to compensate for shifts in drop center due to uneven surfaces or other imperfections in the microfluidic device outlet.

To demonstrate the utility of the diameter-based analysis, we evaluated the performance of our method for measuring flow through straight-channel microfluidic devices against an equivalent computational model based on a set of generalized Hagen Poiseuille equations.

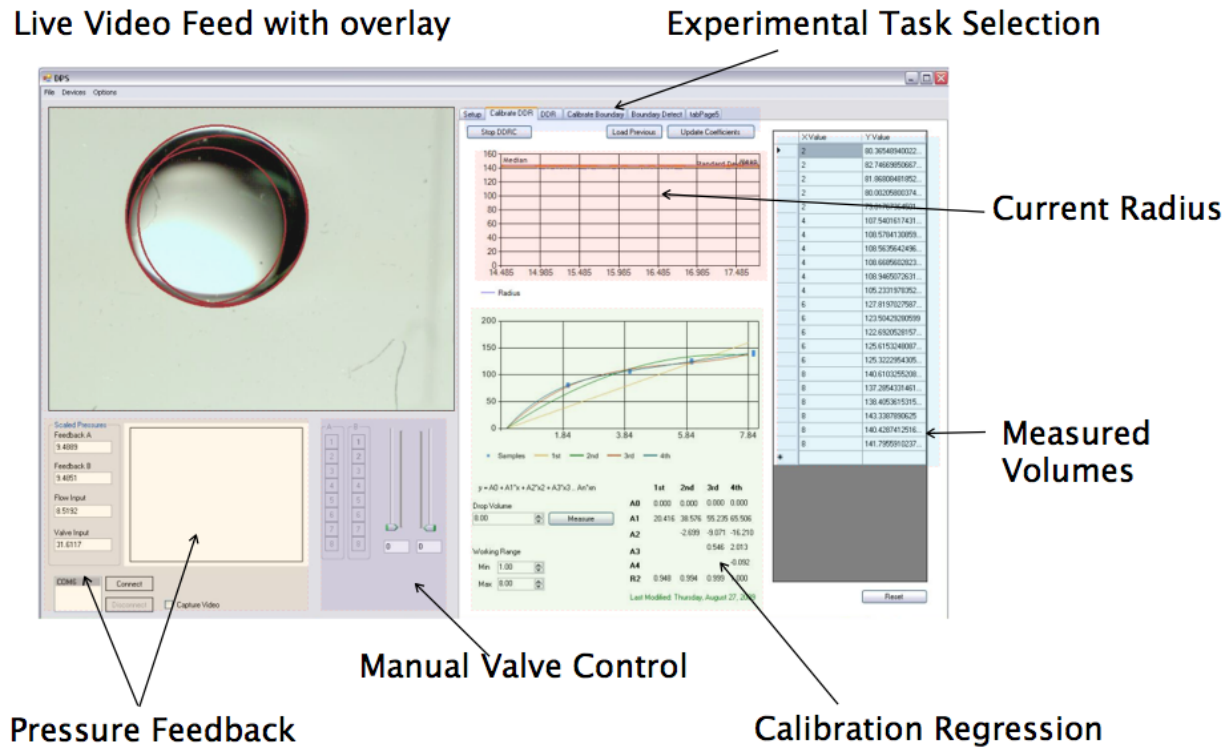

Figure 3.24: **Drop diameter regression user interface.**The user interface displays a live view of the video source. During analysis, a circle overlay is placed onto the image to verify successful identification. Graphs displaying drop diameter, averaged drop diameter, and drop volume are updated as the analysis is being performed. Data in the form of individual points or final estimated flowrate can then be exported into a comma-separated format for further analysis.

3.4.2 Microfluidic device design and fabrication

The microfluidic designs contain a series of straight channels with differing heights and widths. Channel heights vary from 25 μm to 60 μm with widths ranging from 20 μm to 100 μm. These dimensions, while not comprehensive, represent values commonly found in microfluidic devices for biological applications. The devices were fabricated from polydimethylsiloxane (PDMS) using conventional soft photolithographic techniques. Each device was ported using a 20 GA sharpened dispensing needle before final bonding to a glass slide. A 10 inch length of Tygon micro-bore tubing connects sealed fluid reservoirs to each device inlet. The fluid reservoirs, each containing 2.0 mL of de-ionized water, are then connected to a controlled hydrostatic pressure source.

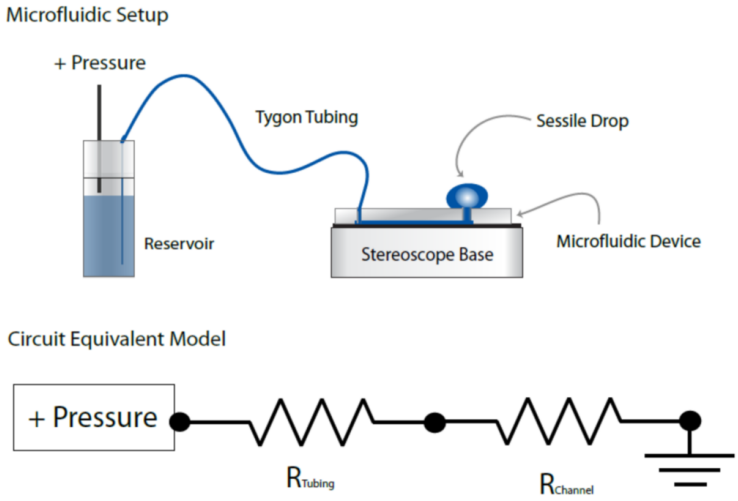

Figure 3.25: **Microfluidic circuit-equivalent model.** Experimental fluid circuit (upper pane) is composed of three components: a sealed fluid reservoir, Tygon microbore tubing, and a microfluidic device. A pressure source drives fluid from the reservoir through the tubing and micro-channel device. A circuit-equivalent model (lower pane) based on a generalized form of the Hagen-Poiseuille equation for pressure driven fluid flow through a channel is used to compare experimental measures to physical theory.

The computational model was created in Matlab (Mathworks, 2009b) to calculate volumetric flowrate (Q) and corrected internal channel resistance (R^*_{Hyd}) for a given set of channel geometries and driving pressures. The model follows a standard circuit-equivalent resistance model (Figure 3.25), using a generalized Hagen-Poiseuille equation (Equation 3.5)to first calculate the fluidic resistance of each model component before solving for the volumetric flow rate across the complete circuit (Q).

$$\Delta p = R_{Hyd} Q = \alpha R^*_{Hyd} Q \tag{3.5}$$

$$R^*_{Hyd} = \frac{\eta L}{A^2} \tag{3.6}$$

$$\alpha = \frac{R_{Hyd}}{R^*_{Hyd}} \tag{3.7}$$

Determination of the corrected hydraulic resistance (R_{Hyd}) was performed using a shape-dependent method based on channel shape and compactness [75]. The complete model produces hydraulic resistance (R_{Hyd}) and volumetric flowrate (Q) as a function of channel geometry (Width-to-Height ratio: γ, Length: L , Cross-sectional area: A^2), dynamic viscosity (μ), and net pressure drop (Δp). Dimensions from the fabricated straight channel microfluidic devices were used to create a set of representative input parameters. Theoretical flow rates were found to increase linearly with respect to increasing driving pressures while the fluidic resistance term remains constant for a given set of channel dimensions.

To avoid the need for specific contact angle measurements, a drop volume calibration curve is created for each microfluidic device to prior to use. The device surface is dried and cleaned of debris using vinyl tape (3M #471). Drops of fluid are placed onto the surface using a micropipetter for the expected working volume range. This range is determined by the effective magnification of the stereomicroscope and the estimated flow rate through the device. A calibration tool integrated into the software records the maximal drop diameter across the working range of known volumes and produces a polynomial regression to fully specify the calibration curve.

In our experimental scenario, driving pressures (7.5 PSI to 12.5 PSI) were expected to yield flow rates from 100 to 1000 nanoliters/sec. Sampling at 10 Hz over 5 seconds would produce a volume difference of up to 5 μL. Using 5 μL as an approximate target, a calibration curve was created for volumes of 1 μL to 8 μL. Drops of each volume (n=10) were placed onto the microfluidic device surface and were measured using the software described above.

Prior to each experiment the device surface is rinsed with de-ionized water and cleaned with vinyl tape to remove debris. The analysis software is started and allowed to collect data autonomously while the experiment proceeds. Multiple experimental runs can be recorded before a final save command writes chronologically-ordered data: drop diameter, pressure, calculated volume, and basic descriptive statistics (mean pressure, mean flowrate, and pearson's R) to a comma-separated file for further analysis. Comparisons between theoretical and experimental data are then carried out using Matlab.

3.4.3 Results

Flow data was collected across all possible channel height, channel width, and driving pressure combinations. Each condition was averaged across eight runs to produce a final flow rate. Sample raw data in the form of maximal drop diameter over time is presented in Figure 3.26. Conversion to drop volume via the calibration curve produces a linear relationship as seen in Figure 3.26a. The average volumetric flow rate (Q_{Avg}) is represented by the slope of the linear regression with a very high PearsonÕs goodness-of-fit measure. Average drop volume change over time for three channel widths (Figure 3.26b) and for three driving pressures (Figure 3.26C) are shown for a single device. Internal channel resistances are then calculated from observed flow rates using the generalized

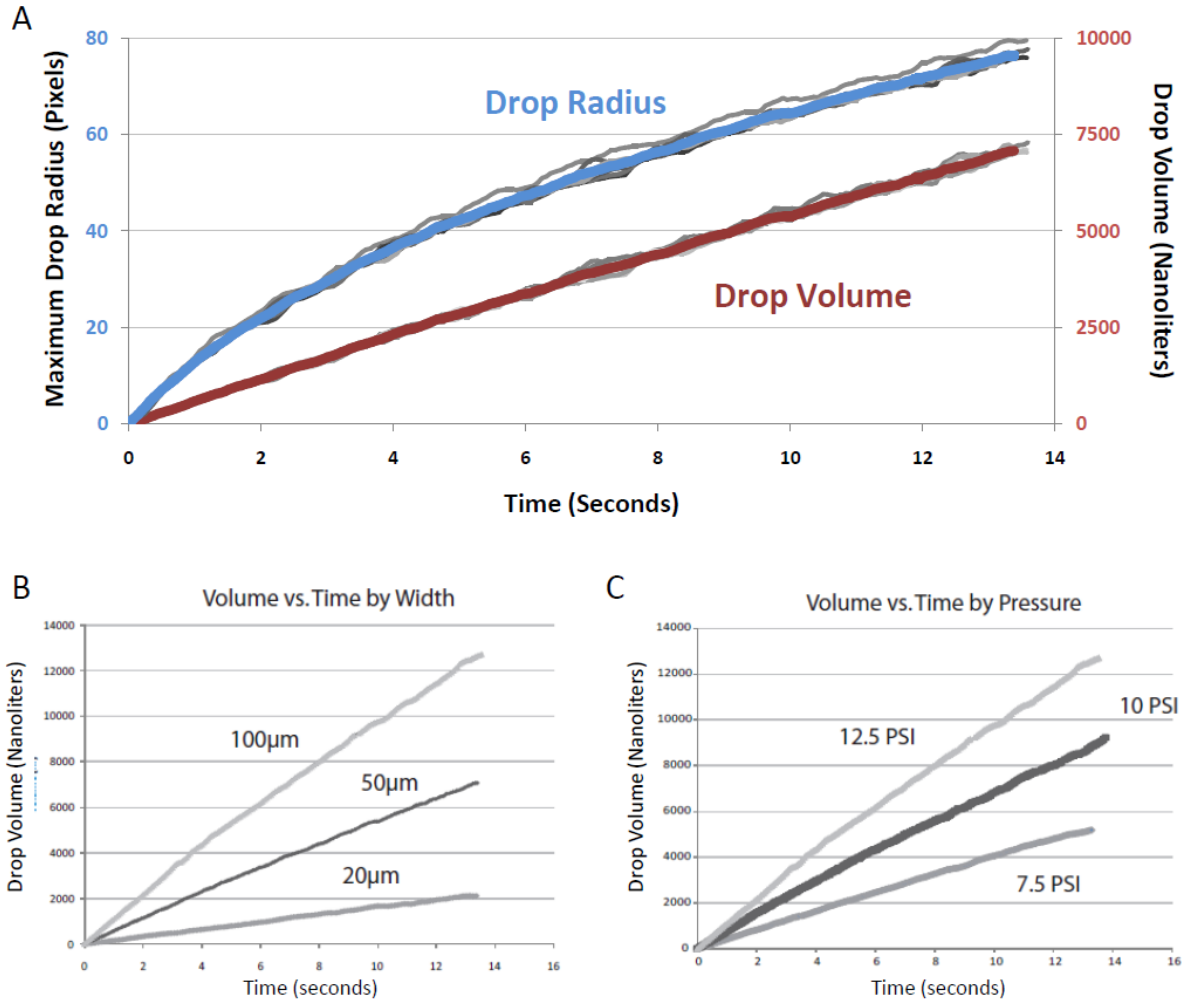

Figure 3.26: **Drop diameter experimental data.** A) Chart showing the relationship between drop radius and volume. The average (thick) of 8 individual experiments (thin) are shown for both the drop radius measurements (blue) and volume calculations (red). One can see the inverse squared relationship between volume and diameter when they are plotted on the same graph. B) Experimental drop volumes over time through three different channel widths from a constant pressure source. C) Experimental drop volumes from 3 different source pressures through the same fluid channel. For the given microchannel, one can easily see the increase in flow rate as pressure increases, as determined by the increased slope of the volume trace.

Hagen-Poiseuille equation described above. Comparison of flow through a single device against model prediction is shown in Figure 6. Good agreement is found between predicted versus experimental flow rates for differing channel widths and driving pressures (Figure 3.27a). In agreement with the linear model, flow rates were found to increase proportionally with increasing driving pressures while channel geometry was held constant.

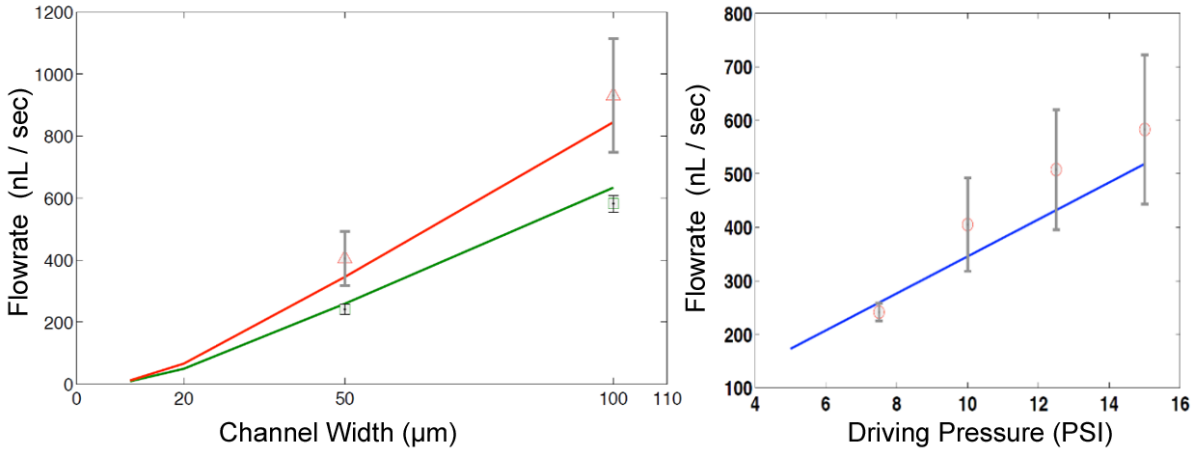

Figure 3.27: **Experimental vs. theoretical flow rate comparison.** The experimental (open symbols with error bars) and theoretical flow rates (solid lines) are plotted against a fixed parameter. A) Constant Channel Height (25 micrometer) with different channel widths and driving pressure. B) Constant channel dimensions with increasing driving pressure.

3.4.4 Discussion

Volumetric flow rates through a straight channel microfluidic device measured using the drop diameter technique matched an analogous computational model based on a generalized Hagen-Poiseuille approach. The agreement between model and experimental measures demonstrate the utility of the technique. The introduction of error from the use of a calibration curve and simplified sessile drop shape-volume relationship is only apparent at the boundary of the working volume range. This error is expected, first from the intrinsic relationship between image resolution and drop diameter accuracy and secondly from the complex interactions governing sessile drop shape. Two measures are readily available to address this error. Directly, the working range can be adjusted by physically modifying the magnification of the stereoscope to minimize the boundary edge effects. To account for the additional interactions inherent in sessile drop shape, a higher order polynomial regression may be chosen to account for the variance present throughout the working range. During our experimental analysis the flow rates were held constant with the final volumetric flow rate obtained from the linear region of curve. A higher order polynomial may be considered for experimental conditions that involve dynamic flow rate changes or a variable device configuration.

3.4.5 Outlook

Here we have demonstrated a simple approach for volumetric flow rate measurement in a microfluidic device using readily available hardware and software. The approach relies on the fixed surface tension interactions that governs contact angle at a fluid-solid interface to assume that, for a given range of drop volumes, the maximal drop diameter obeys a smooth relationship. Software was written to analyze the drop volume changes over time to produce a volumetric flow rates while the microfluidic device was online. The method was validated against a theoretical computational model.

4.0 STRUCTURAL REFERENCES FOR FINE-SCALE NEUROANATOMY

4.1 DIFFUSION-WEIGHTED IMAGING

Diffusion-weighted imaging is a subset of magnetic resonance imaging that takes advantage of the asymmetric diffusion of molecules through permeable biological microstructures. Briefly, a strong RF pulse is used to excite molecules along a defined plane. The response is sampled with a temporal resolution exceeding the relative diffusion time of the water molecule within the voxel size specified. The signals measured are then indicative of how rapidly the excited molecules travel outside of the original imaging plane. A strong signal indicates regions of restricted diffusion. A weak signal indicates free diffusion. By scanning slices across multiple angles, it is possible to build a map of preferred diffusion directions across the entire brain. Algorithmic development to extract useful information through post-processing of DWI data are under constant development. Multiple scan protocols and analysis techniques have been developed to address specific issues in DWI such as white matter crossing angle or packing density. A significant need exists to validate these analytical methods on absolute predefined physical structures.

4.2 MICRO-DWI PHANTOM

4.2.1 Research plan

A microfluidic diffusion phantom (MP) for diffusion-weighted imaging was developed to provide a reliable physical structure with which high resolution fiber tractography methods can be validated against. The diffusion phantom was fabricated using conventional photolithographic techniques to create an internal channel network that mimics white matter fiber tracts. A multilayer structure was used to maximize fluid volume within the phantom to increase SNR in each sample voxel. Each layer is fabricated independently and later linked via a cross-layer fluid connection referred to as a "via". The channel orientation and layer count are definable at fabrication time, allowing for arbitrary stacking and crossing angle. Configurations containing stacked parallel patterns, crossing patterns, or radially-oriented channels will then be used to validate specific issues with current tractography methods with regard to crossed fibers, low-angle intersections, and areas of high curvature. The fluid channels have a square cross section with a characteristic side length as defined by initial CAD designs. Perfusion of the

phantom is performed using a constant pressure system to push doped MR fluid into the device, forcing air from the microfluidic channels into the surrounding semi-permeable substrate. This process results in a sealed diffusion phantom containing a bubble-free network of fluid-filled channels suitable for diffusion weighted imaging.

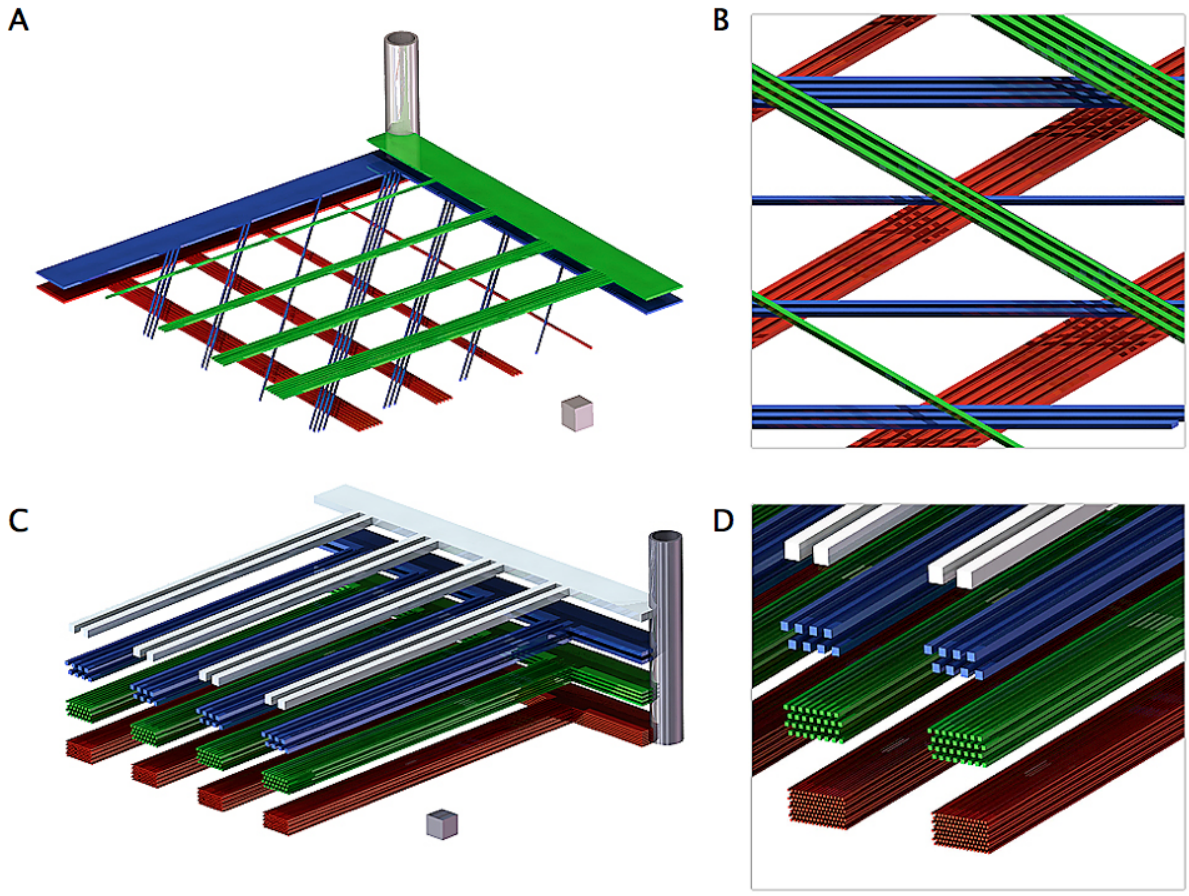

Figure 4.1: **Microfluidic diffusion phantom conceptual designs.** Rendered images of phantom design concepts that present difficult issues for current DWI-based analysis. A) Full view of a "Multiple crossings" phantom. This design contains multiple crossing locations with variable fiber counts at each layer. 1mm^3 cube located in lower right corner for scale. B) Detailed view of the "Multiple crossings" phantom. C) Full view of a "Volume equivalent" phantom. This design contains layers with different channel distributions with identical volume fractions. 1mm^3 cube located in lower right corner for scale. D) Detailed view of the "Volume equivalent" phantom.

4.2.2 Design parameters

The conceptual phantom designs were developed around a set of physical constraints established from white matter tract dimensions, limits of DWI resolution, and current capabilities of the photolithographic fabrication method used.

Current diffusion phantoms contain feature sizes on the order of 500μm or greater. With improvements to DWI scan protocols and post-hoc tracking methods, the ability to resolve of more detail allows for smaller feature size and greater complexity. Preliminary channel dimensions for the microfluidic phantom were therefore defined by a working range of white matter tract diameters from 5μm to 300μm. Two design types were developed initially: a single parallel channel configuration with angular reference marks and a grid-based configuration with 9 individual voxel locations. The angular design was created with the endpoint goal of creating arbitrary low-angle crossing patterns between layers. The grid-based design was created to allow multiple crossing patterns within a single microfluidic phantom.

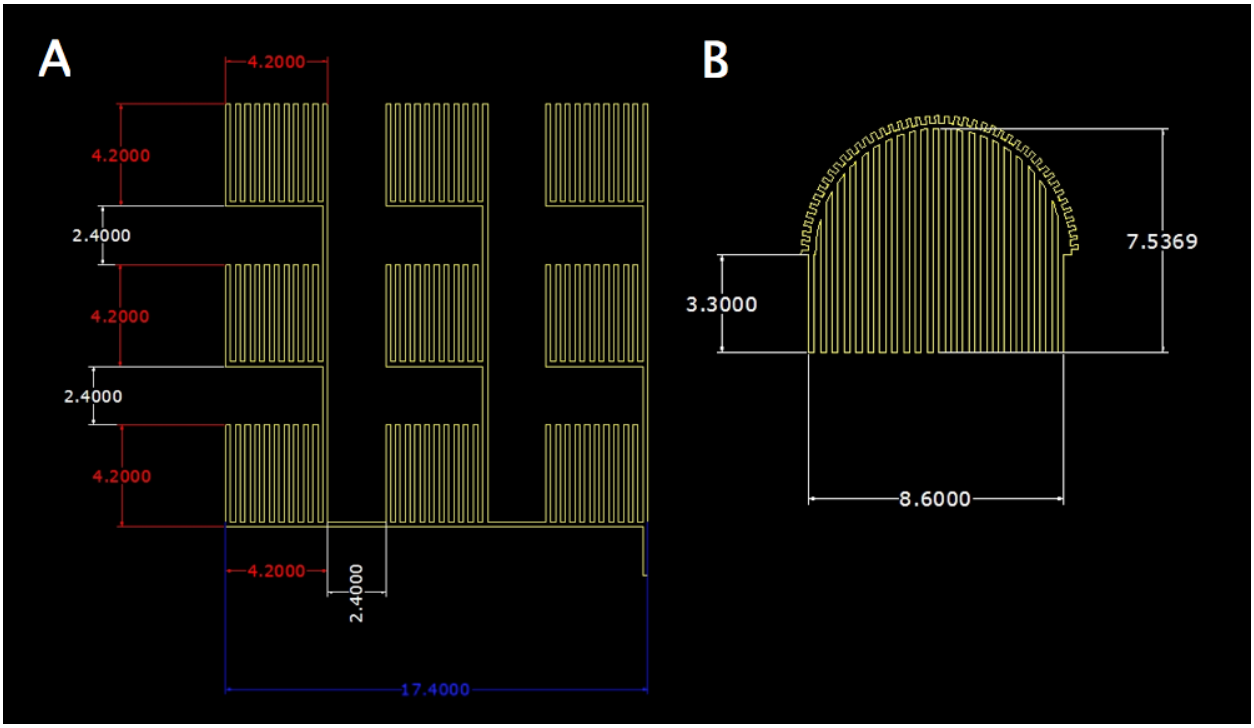

Figure 4.2: **Microfluidic diffusion phantom channel configurations.** Annotated CAD drawings of the grid-based (A) and angular (B) designs. Both designs were developed around a working voxel size of 2.2mm with a 1mm alignment factor. All units are in millimeters.

The minimum voxel size was governed by the MRI specifications and the specific DWI scan protocol used. A voxel size of 2.2mm x 2.2mm x 2.2mm was used as the starting point from which an adjustment factor was added to accommodate up to 1mm of misalignment within the scan plane. The minimum voxel size established a baseline volume from which the fluid volume fraction was calculated. Increasing volume fraction will increase the SNR of the DW signal within each voxel. Maximization of the fluid volume fraction is a direct benefit toward increasing the versatility of the microfluidic phantom and is therefore a primary research goal.

The limiting constraints for the volume fraction optimization process are controlled by the photolithographic fabrication technique used in device fabrication. Soft photolithography uses a polymer (Polydimethylsiloxane or

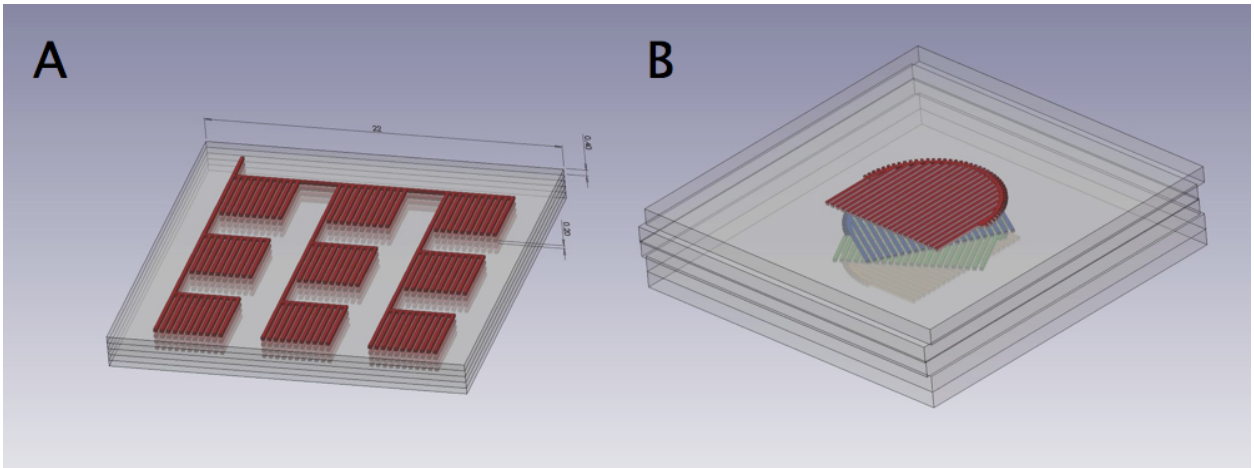

Figure 4.3: **Microfluidic diffusion phantom full device renders.** Rendered images of assembled four-layer devices filled with a color dye. A) Grid-based phantom device, containing 9 experimental voxels. Visualized with a 400μm layer thickness. B) Angular phantom device, containing single experimental voxel with arbitrary layer orientations. Visualized with a 1mm layer thickness.

PDMS) as the primary structural component of the microfluidic phantom. To increase the fluid volume fraction, channel density much be increased. In doing so, the layers of supporting PDMS will become proportionally thinner. During the fabrication process, these thin layers of PDMS become difficult to handle manually and are prone to tearing. During fluid perfusion of each device, the thin regions of each layer are the site of pressure-induced punctures. Fabrication capabilities exist to define channel structures with a resolution of less than 10 microns; however the structural integrity of the substrate remains the limiting factor in determining the maximum fluid volume within a single sample voxel. Stiffer substrates such as PMMA may provide for greater overall integrity but do not provide a viable option for gas removal during the forced perfusion process.

4.3 METHODS

Each microfluidic phantom is fabricated using a conventional multilayer soft photolithographic method. Following a coordinated series of steps, a computer-generated design is converted into a re-usable physical mold referred to as a device master. A transparent polymer compound (polydimethylsiloxane or PDMS) is then poured onto each master and allowed to harden. The polymer layers are removed from the master and assembled into a final device by hand. Multiple diffusion phantoms are then placed into a larger fluid container roughly the size and volume of a conventional MRI phantom.

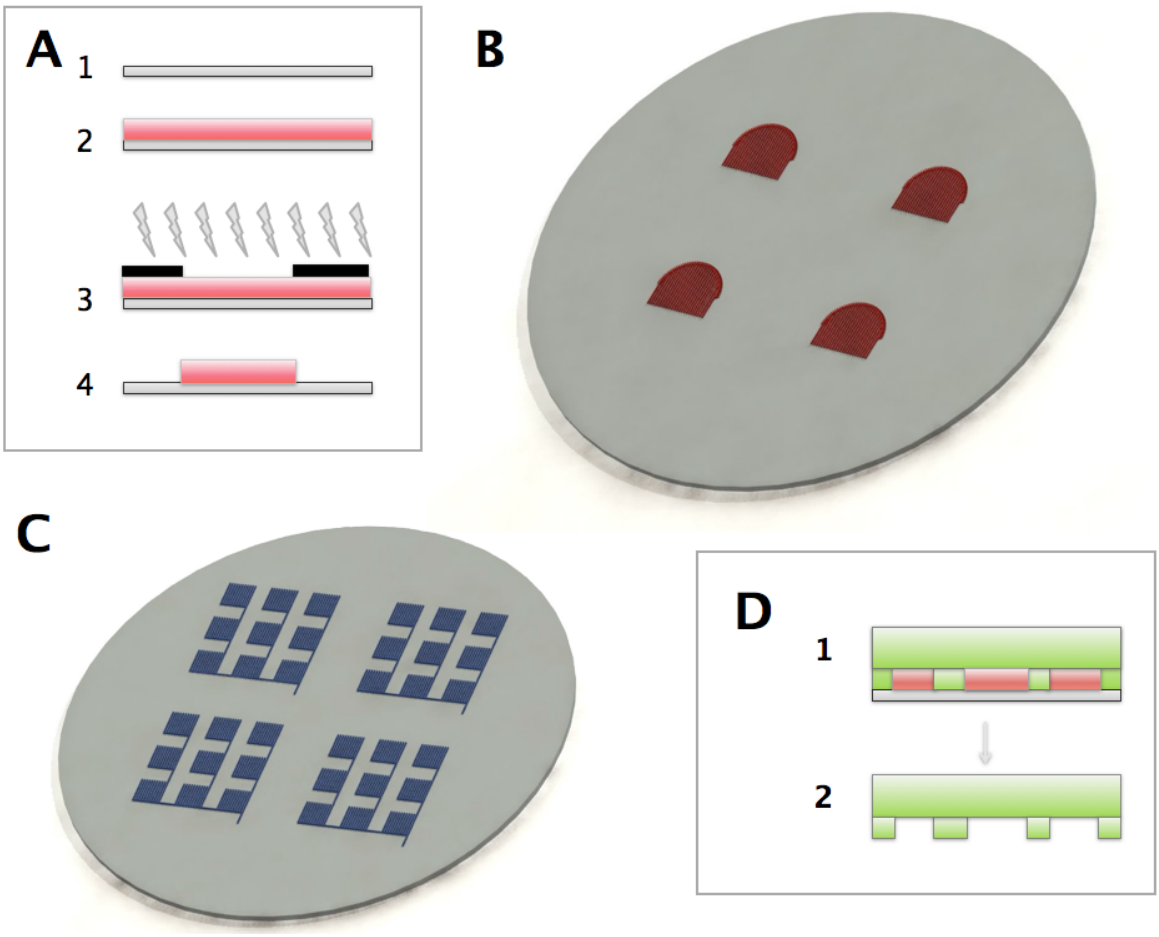

Figure 4.4: **Microfluidic diffusion phantom fabrication.** Photolithographic Fabrication Method. A) Master fabrication workflow. The silicon wafer is first cleaned with isoproponal[1]. A negative photoresist (SU-8 2100) is spun onto the wafer[2]. The resist is baked and then exposed to UV light[3]. The unexposed resist is then removed during a development bath[4]. B) Render of a completed angular master. A single master will produce four layers with equal height for every iteration. C) Render of a completed grid-based master. D) Layer fabrication workflow. PDMS is prepared and degassed before pouring onto the device master. The PDMS is baked until hard[1]. The PDMS layers are then removed from the master and prepared for assembly using O^2 plasma bonding[1].

4.3.1 Tract design

Tract designs are created using CAD software (AutoCAD 2007, Autodesk) using the design criteria mentioned prior. Tract designs are then transferred to a printed transparency mask at 20,000 DPI with a minimum feature resolution of 5 microns through an outsourced laser printing facility.

4.3.2 Master fabrication

The device master is created by first spin-coating a photo-crosslinkable substrate (SU-8 2100 Negative photoresist, Microchem Corp., Newton, Ma) onto a clean silicon wafer. For the sake of brevity, a single resist and protocol will be described, but the process is quickly generalizable across different resist types and heights, enabling channel designs defined heights and cross-sectional profiles. To create channel structures for a 200μm phantom, approximately 100 grams of the SU-8 photoresist are poured onto a silicon wafer cleaned with isopropanol. The wafer is then spun at 1000 rpm for 60 seconds with a ramp acceleration of 200 rpm/s. This yields a layer of photoresist approximately 200 μm thick across the surface of the wafer. Masked UV exposure of 30 seconds cross-links features within the negative photoresist. The master is then developed using non-dilute SU-8 developer for 10 minutes, removing all of the unexposed resist. Finally a hard bake is performed at 150°C over two hours, ramping at 20°C per hour to improve the integrity of the surface bond between the silicon wafer and the photoresist. The hard bake process allows the master to be reused to make multiple copies of the same device design.

4.3.3 Phantom fabrication and assembly

To produce the microfluidic phantom device, a pre-weighed amount of polydimethylsiloxane (PDMS) is poured onto a device master and spun to the desired thickness. The PDMS layer is degassed in a desiccator and then baked at 80°C for one hour. After baking, the PDMS layers is removed and sliced into individual layers. Debris is removed from the layer surfaces using vinyl tape (3M #471) before undergoing Oxygen plasma bonding. The assembled devices are then ported using a sharpened 20 GA dispensing needle. Filling of the phantom device is performed using a constant pressure source (Nitrogen) attached to a sealed fluid reservoir containing doped MR fluid. The reservoir is connected to phantom with Tygon microbore tubing. A static pressure (8 PSI) is applied to the reservoir, forcing fluid into the device. Once the device has been fully perfused, the tubing connecting the device and reservoir is clamped, allowing for disconnection.

A watertight plastic (polyethylene) container with dimensions of 11 cm O.D. x 15 cm tall was used for the outer shell. An internal shelf constructed from polycarbonate was added to the container to place multiple phantoms on. A mounting brace was created with polycarbonate and secured using nylon screws and mounting fixtures. After filling each phantom, the container itself was filled with MR solution and sealed. The final container volume is approximately 900 mL.

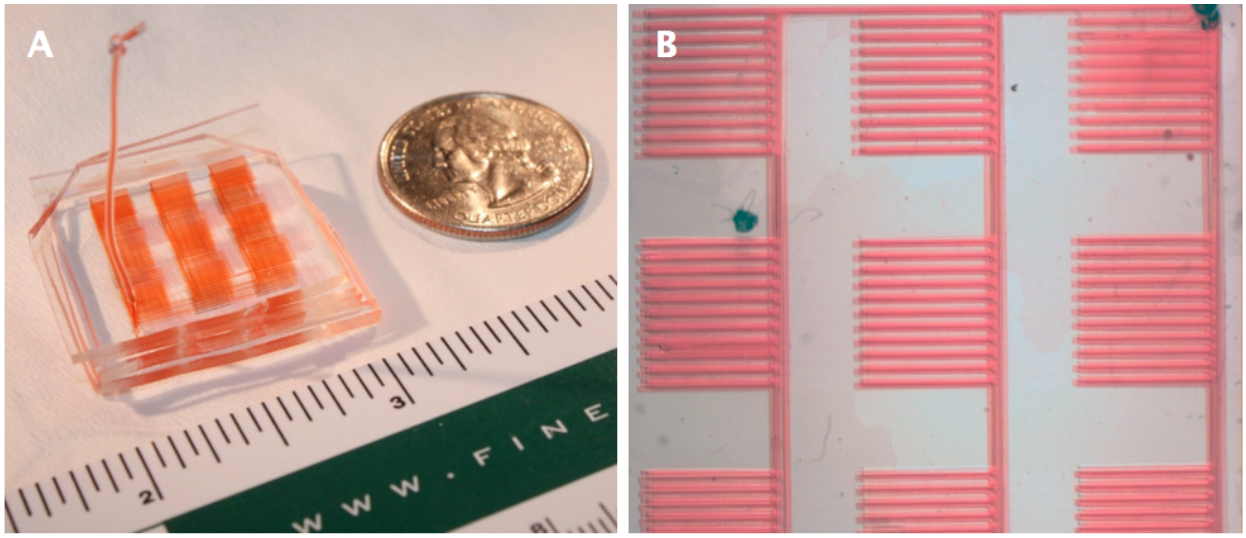

Figure 4.5: **Assembled and filled microfluidic phantom.** A) Assembled PDMS phantom filled with MR doped solution with a soluble MR-safe red dye added to visualize channel filling. Layer heights are 1mm yielding a final height of 5mm. B) Magnified view of internal channel structures. Channels are 200μm wide with 200μm spacing between. Minor channel offsets can be observed between layers, however no net effect will be observed as the principal diffusion directions remain aligned across layers.

4.4 OUTLOOK

The microfluidic diffusion phantom was scanned both independently in the standalone container and concurrently with a human subject in a Siemens 3T magnetome. A proprietary diffusion protocol was used to produce a high angle representation of the phantom. Post-processing algorithms were then used to generate tract-based maps onto the areas of the phantom containing internal channel structures.

A complication of low signal-to-noise in the experimental voxels limited the ability of the preliminary experiments to resolve a 1 to 1 representation of the channel structure to mapped tract. Low SNR produces a decreased dynamic range during sampling of each voxel, effectively blurring the difference between free and restricted diffusion directions. To address this issue in future designs, increased channel volumes with respect to voxel size will be developed. By increasing the net volume fraction of water to PDMS, an increased SNR will be realized.

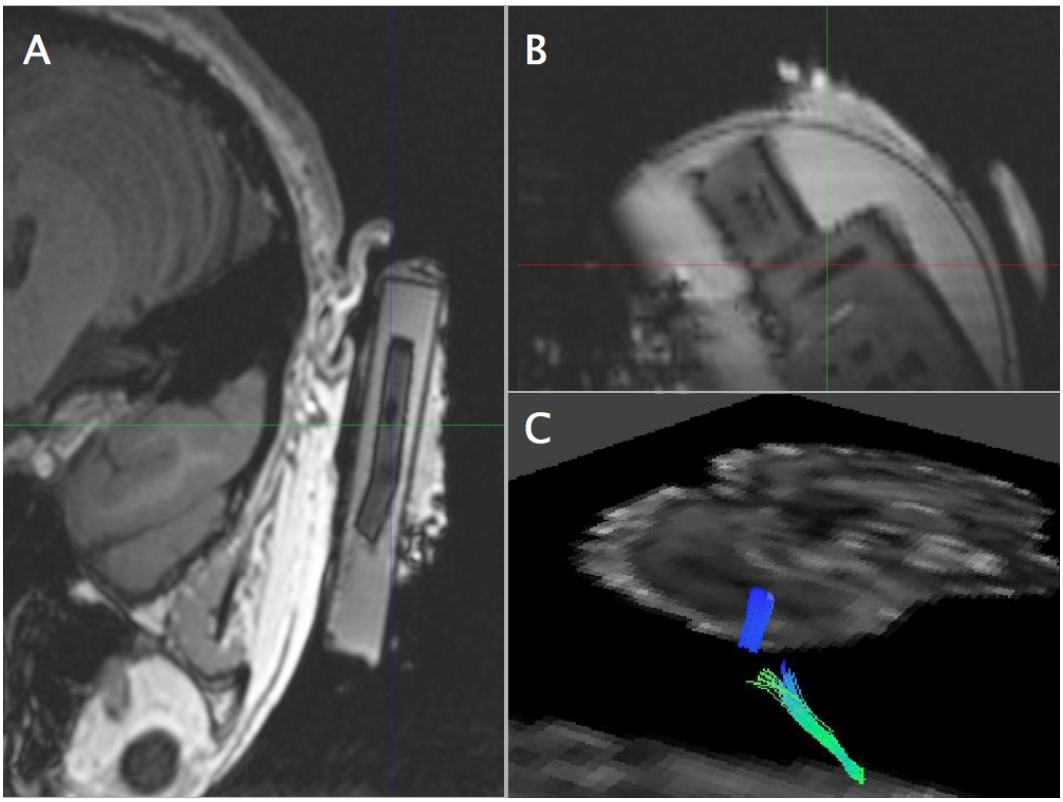

Figure 4.6: **Preliminary DW-MRI Results.** Images of the diffusion phantom from a simultaneous scan procedure using a Siemens 3T magnetome. A) Cropped portion of a T1-weighted coronal MRI. Fluid regions will appear dark. B) T1-weighted image slice from sagittal view. Internal channel structures are visible as dark regions. C) Angled view with preliminary fiber tracking results. Colors correspond to preferred diffusion direction according to conventional anatomic axes. (Images provided by Walter Schneider, University of Pittsburgh)

5.0 CONCLUSION

Neurobiological systems span a wide dimensional range. We present a scale-driven methodological development for three biological systems to demonstrate the utility of applied engineering approaches in neurobiology and provide an avenue for future study. Concepts in computational modeling, microfluidic device platforms, and MRI phantoms are examined - starting from the level of a single synapse and concluding with long-distance cortical connectivity.

5.1 COMPUTATIONAL MODELS OF NEURAL ACTIVITY

A preliminary model was designed and implemented to integrate multiple aspects of diffuse calcium signaling at the post-synaptic density.This model demonstrates the feasibility of using a molecular-scale approach to identify key features of STDP-based results. It is thought that more complete understanding of the mechanisms responsible for STDP and related responses will provide an increased ability to model the self-organization of a neural network.

A recurrent small network model was implemented to address the role of geometrical parameters on the character of neural activity. It was shown that sufficient inhomogeneity was produced from random seeding and connectivity methods to produce preferential propagation of waves of activity throughout the cyclic network.

5.2 MICROFLUIDIC PLATFORM DEVELOPMENT

Neuronal synapses are sub-cellular domains with distinct physiological properties. Signaling dynamics in these regions occur on the order of milliseconds and across sub-micron distances. Advances in microfluidic technologies provide a functional toolset to design and conduct experiments to address cell signaling and chemotaxis at this scale. Current microfluidic strategies are able to produce focused streams, timed pulses, and smooth gradients of diffuse chemoactive molecules.

Here we have demonstrated a simple approach for volumetric flow rate measurement in a microfluidic device using readily available hardware and software. The approach relies on the fixed surface tension interactions that governs contact angle at a fluid-solid interface to assume that, for a given range of drop volumes, the maximal

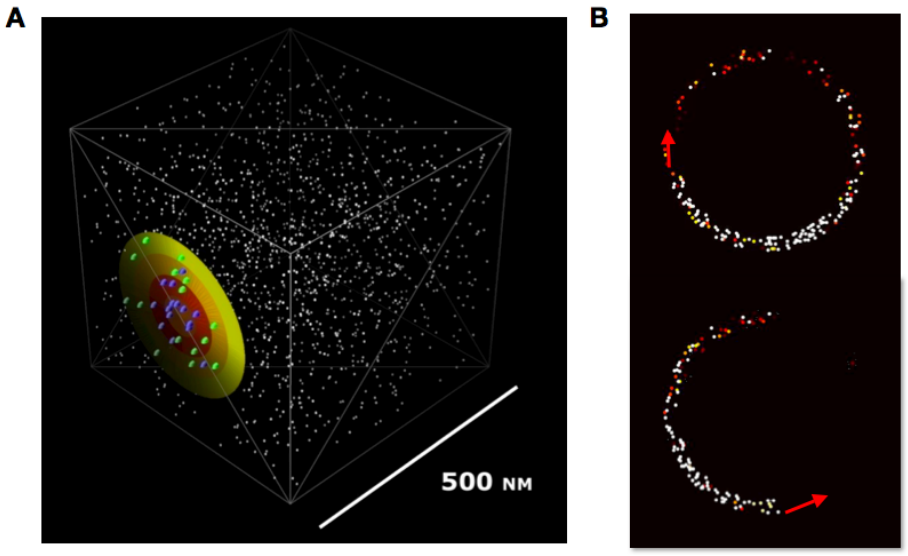

Figure 5.1: **Summary: Computational models of neural activity.** A) Spatial model for STDP-based signal detection using calcium-mediated biophysical mechanisms. B) Directional wave propagation in a recurrent network model using constrained cyclic geometries.

drop diameter obeys a smooth relationship. Software was written to analyze the drop volume changes over time to produce a volumetric flow rates while the microfluidic device was online. The method was validated against a theoretical computational model.

Here we have presented a microfluidic control platform that integrates multiple design strategies to address the intrinsic high spatiotemporal resolution of neurons. The polydimethylsiloxane (PDMS) microfluidic device, fabricated using multilayer soft-lithography, contains a modified push-down valve configuration to guide multiple laminar streams. The control platform implements a dynamic pressure system to produce variable internal resistances while maintaining full binary control of each push-down valve. By adjusting the relative and absolute inlet pressures, we are able to produce a targeted hydrodynamic laminar stream with high spatiotemporal resolution and repeatability. Custom hardware and software provide an interface to define experimental protocols and generate flow profiles. Multimodal sensor feedback enables closed-loop control of the platform across multiple experimental conditions. System performance was characterized using arbitrary profile generation, profile repeatability, and selective targeted labeling of cells in culture.

In its current form, the platform is readily extensible for non-neuronal culture applications. Looking to the future, the next steps in the development of the experimental platform focus on creating complete cell culture protocols following the task-based approach.

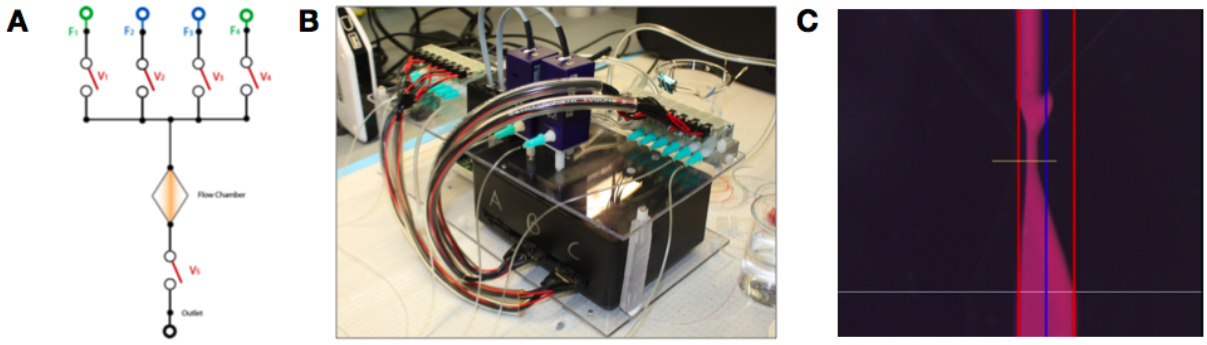

Figure 5.2: **Summary: Microfluidic platform.** A) Conceptual design of a dynamic valve-based device for cell stimulation. B) Control platform hardware furnishing pressure sources and feedback to a PC interface. C) Laminar measurement and tracking, implemented in near real-time using computer vision libraries.

5.3 MICROFLUIDIC DIFFUSION PHANTOM

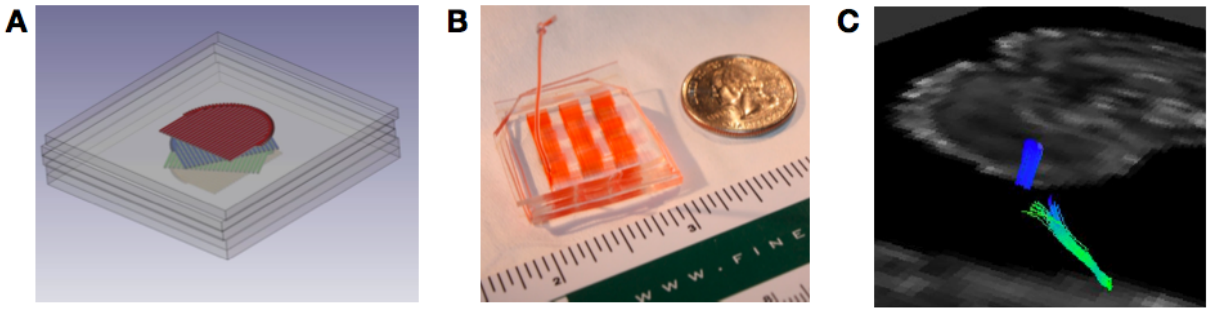

Figure 5.3: **Summary:Microfluidic diffusion phantom.** A) Conceptual render of multiple crossing diffusion phantom. B) Filled phantom with dyed fluid to visualize internal structures. C) Preliminary tractography results showing mapped tracts to phantom structures.

Finally, a microfluidic phantom for diffusion-weighted magnetic resonance imaging was developed for validation studies of long-distance cortical white matter connections. The diffusion phantom provides a reliable physical structure with which high resolution fiber tractography methods can be tested against. The diffusion phantom was fabricated using conventional photolithographic techniques with an internal channel network that mimics white matter fiber tracts and crossings. We show mapped tracts to the features inside of the phantom via post-processing of diffusion-weighted images.

APPENDIX

ADDITIONAL MATERIALS

A.1 SOURCE CODE DESCRIPTION

All source code described below is available or will be made available pending publication at http://zrg.bioe.pitt.edu. The code is released under a BSD license unless otherwise noted.

A.1.1 Computational

- **propmodel** - (matlab class and script): Based on Izhikevich cortical code, generates constrained network model from given parameters, simulates, and produces images and data for visualization
- **siamxppmcell** - (matlab class and script): Runs deterministic model to generate calcium release profiles, refactors profiles into probabilities, runs MCell with specified inputs, loads and parses molecule data from mcell, generates figures for later analysis and visualization
- **ddrmodel** - (matlab class and script): simulates H-P flow through a straight-channel microfluidic device with known geometries. Reads raw data from experiment to generate comparisons between theoretical and experimental measures. Generates figures and graphs of results.

A.1.2 Microfluidics

- **autocirclemate** - (matlab script): Performs post-hoc circular Hough transforms on a static image imported into matlab. Used to perform proof-of-concept experiments behind the drop diameter methodology.
- **video2flowrate** - (matlab script): Performs post-hoc circular Hough transforms on a series of images or video source imported into matlab. Used to perform proof-of-concept experiments on flow-rate measurement using the drop diameter regression method.
- **video2data** - (matlab script): Performs manual boundary detection of a flow profile video captured from the DPS platform. Used to perform proof-of-concept experiments in boundary tracking. Exports position data to raw text.

- **DPS** - (VC# project): what it does... The dynamic pressure system project is built around a central user interface (baseform) with functions subserved by other classes. The project references the Microsoft .Net 3.5 framework, Intel OpenCV vision library, Microsoft Chart for plotting, and Microsoft Excel COM APIs for the regression analyses.
  - **DPS baseForm** - (C# class): Manager code, instantiates all objects used and handles messaging between them. Video capture and task selection are defined here.
  - **DPS baseControl** - (C# class): General hardware code. Instantiates all connections between National Instruments DAQ and ties into the valvecontroller subclass. Device state management is handled here, with XML serialization used to access the discrete device states and experiment protocols.
  - **DPS valveControl** - (C# class): Specific hardware code. Interface to the Quake 24bit valve controller.
  - **DPS Analyze** - (C# class): Storage and analysis code. All imaging data is passed through her to generate usable forms. Includes intensity profile creation, chymograph generation, and raw data export.
  - **DDR standalone** - (C# class): A reduced version of DPS baseForm designed to be redistributed as a standalone product. Removes unneeded library dependencies.

A.2 SUPPLEMENTAL FIGURES

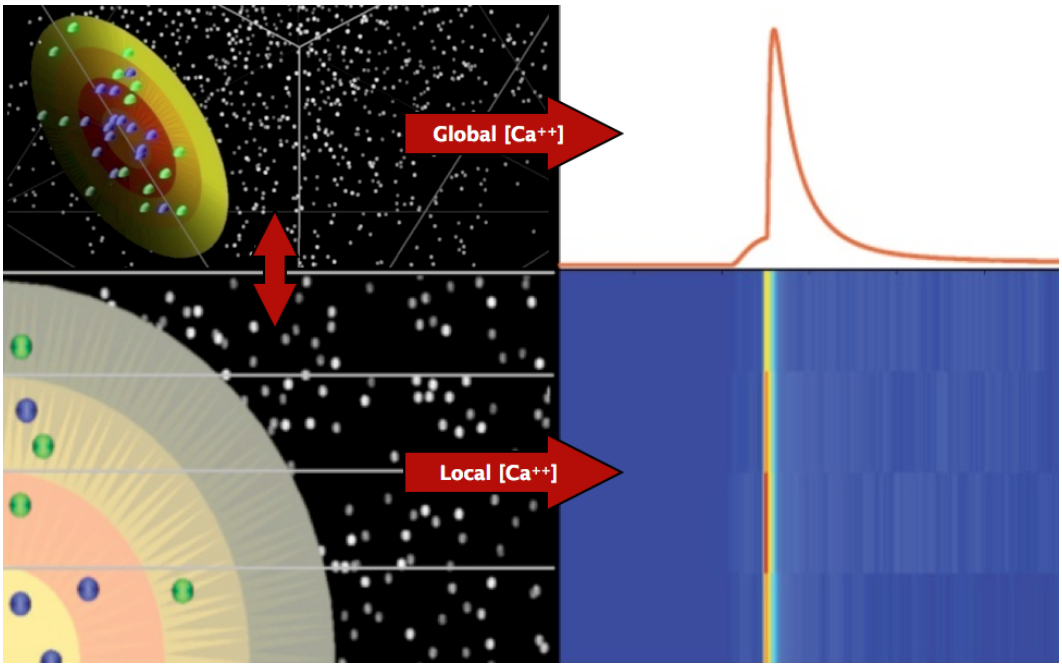

Figure A1: **Global vs. local intracellular calcium profiles.** The MCELL model has been calibrated to reproduce the peak global intracellular calcium concentrations produced from the original Rubin model. To quantify local signaling around the synapse, cylindrical sampling volumes provide radial concentrations at the PSD.

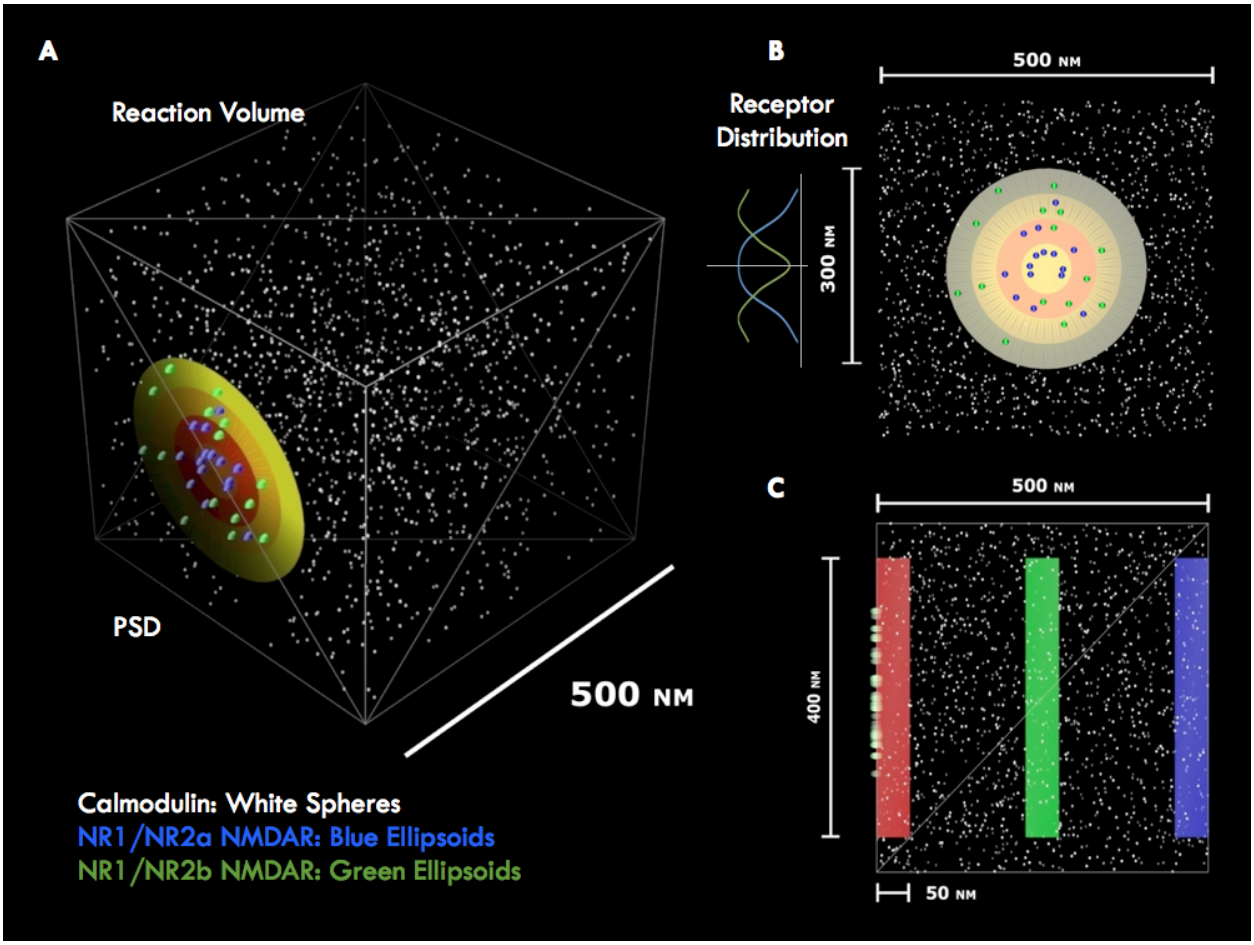

Figure A2: **Spatial model of synapse.** A) Isometric view of full reaction volume and postsynaptic density region. White spheres represent individual calmodulin molecules. B) Receptors are placed radially according to a normalized distribution. Blue ellipsoids represent NMDARs that are defined by NR2a channel kinetics while Green ellipsoids represent those defined by NR2b channel kinetics. The four regions of the PSD can be easily seen. C) Regional sampling volumes used to measure relative concentrations by the PSD, in the middle of the reaction volume, and at the most distal location

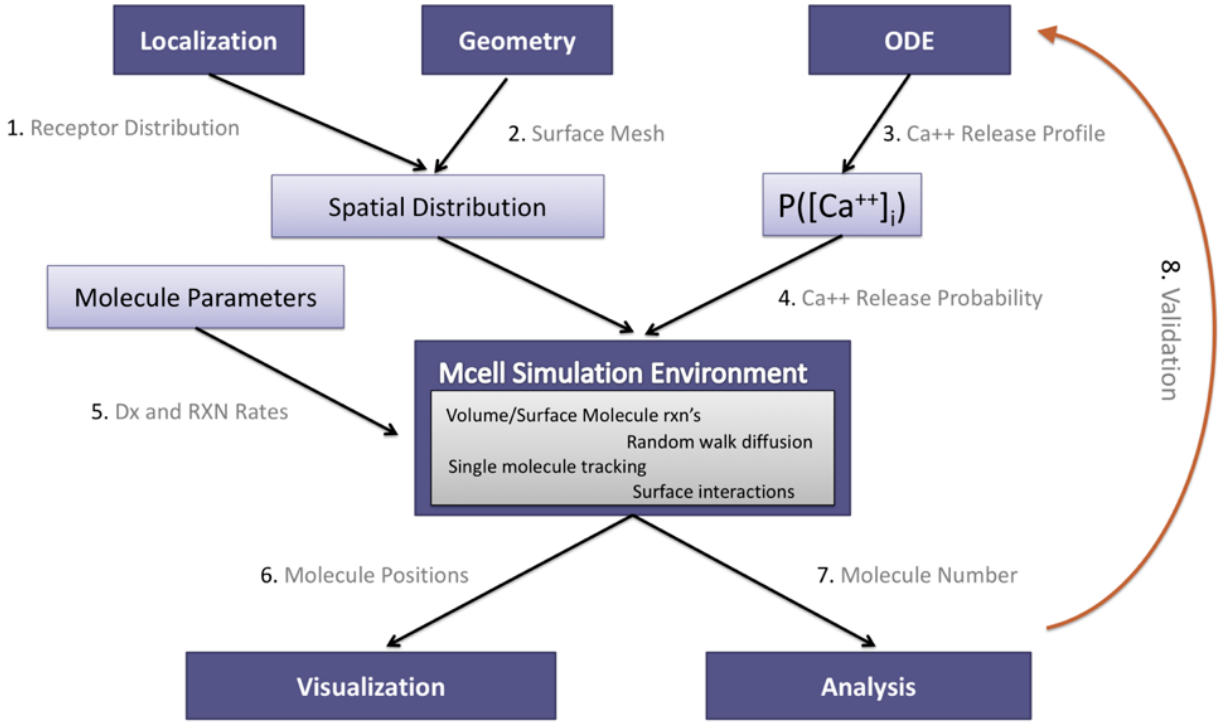

Figure A3: **MCell model pipeline.** Model inputs are obtained from multiple experimental and computational sources to provide a functional set. Physiologic NMDAR and VSCC surface distributions[1] are incorporated into pre-defined regions of a mesh[2] modeled from the post-synaptic density. NMDARand VSCC calcium current contributions are obtained from a deterministic simulation of membrane depolarization following a 1 Hz paired pulse STDP induction protocol[3].The currents are then converted into probabilistic release rates[4] using the given number of channels in the model. Macroscopic diffusion constants and molecular reaction rates are included to complete the model[5]. Following execution, data is piped into visualization software, DReAMM[6] and Matlab[7] for further analysis. Free intracellular calcium is then used as a metric to validate the response of the MCell model against the original deterministic model[8]. Once validated against the simple STDP input, the model will be tested for robustness against the triplet results found experimentally [88].

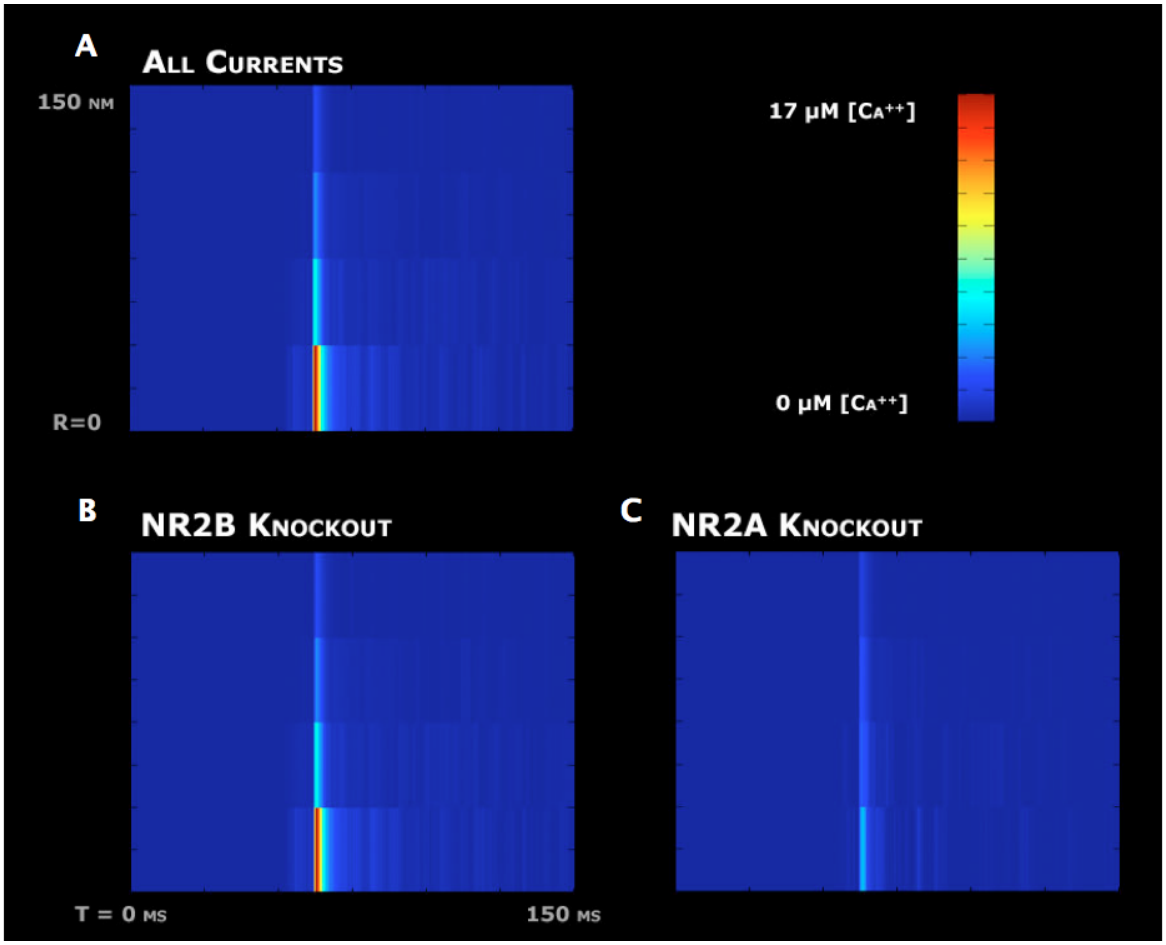

Figure A4: **Spatiotemporal calcium profiles for pre-10-post input conditions.** A pre-10-post stimuli contains a significant amount of NR2a-based calcium current leading to potentiation. A) Spatiotemporal concentration plot of intracellular calcium. Data is plotted with the edge of the PSD at the top of the Y-axis. Peak levels of calcium are observed near the center of the synapse at much greater magnitudes (17 μM) versus the global peak observed (8 μM). B) Matching with experimental results, blockade of the NR2b-dominant NMDA channels has minimal affect on signaling near the central active zone. C) Blockade of the NR2a-dominant NMDA channels, however, produces a pronounced decrease in the levels of intracellular calcium, thought to nullify the LTP effect typically seen.

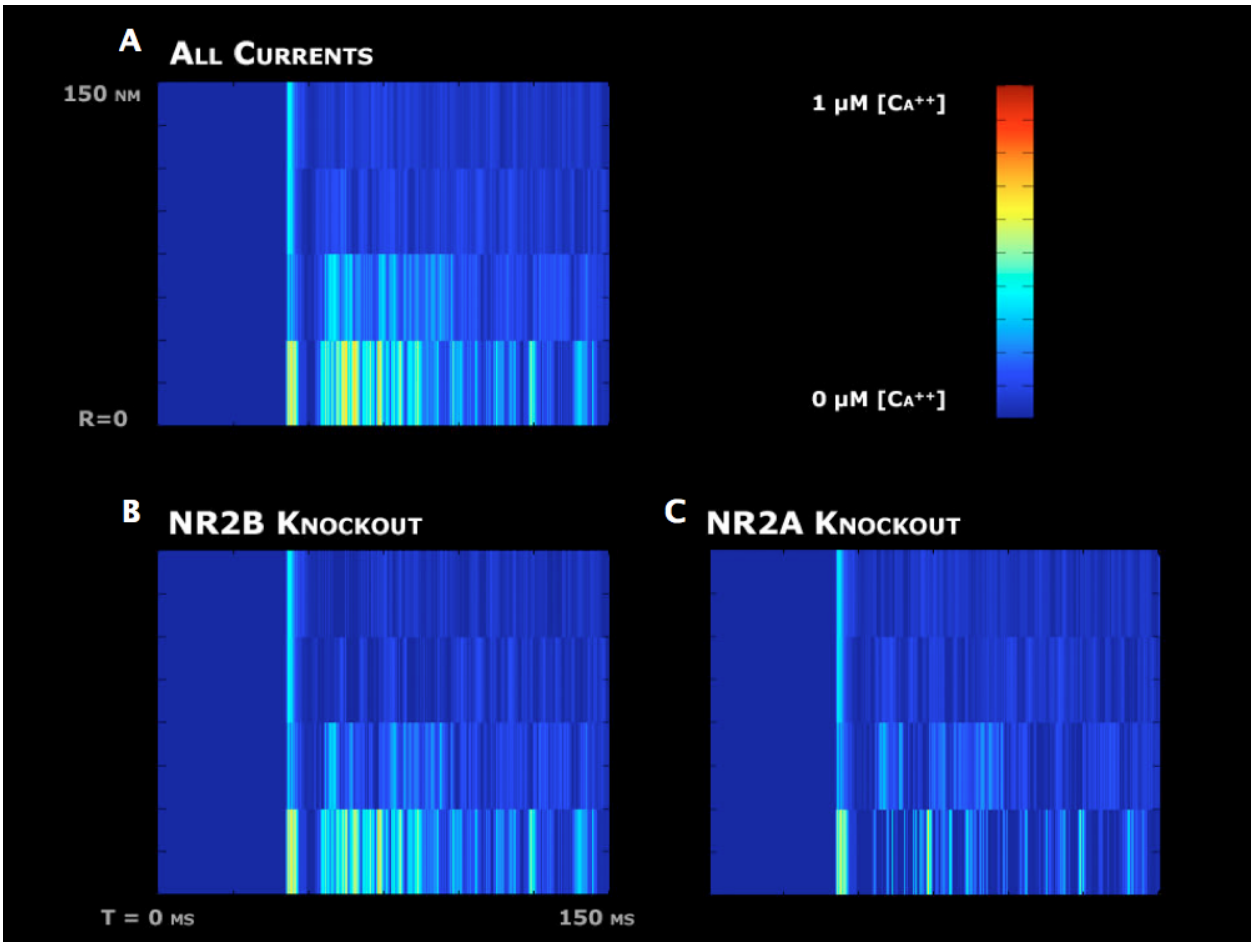

Figure A5: **Spatiotemporal calcium profiles for post-10-pre input conditions.** A post-10-pre stimuli contains a mixed amount of NR2a-based and NR2b-based calcium current leading to depression. A) Spatiotemporal concentration plot of intracellular calcium. Unlike the pre-post protocols, the post-pre protocols yield a more distributed calcium concentration throughout the reaction volume. It is important to note that the color map is arbitrarily scaled with a peak concentration of 1 μM. B and C) Similar NR2b and NR2a blockade simulations did not yield the pronounced results from LTD producing input profiles. Identifying if this deviance is due to a missing model component or simply un-optimized parameters remains an important future goal.

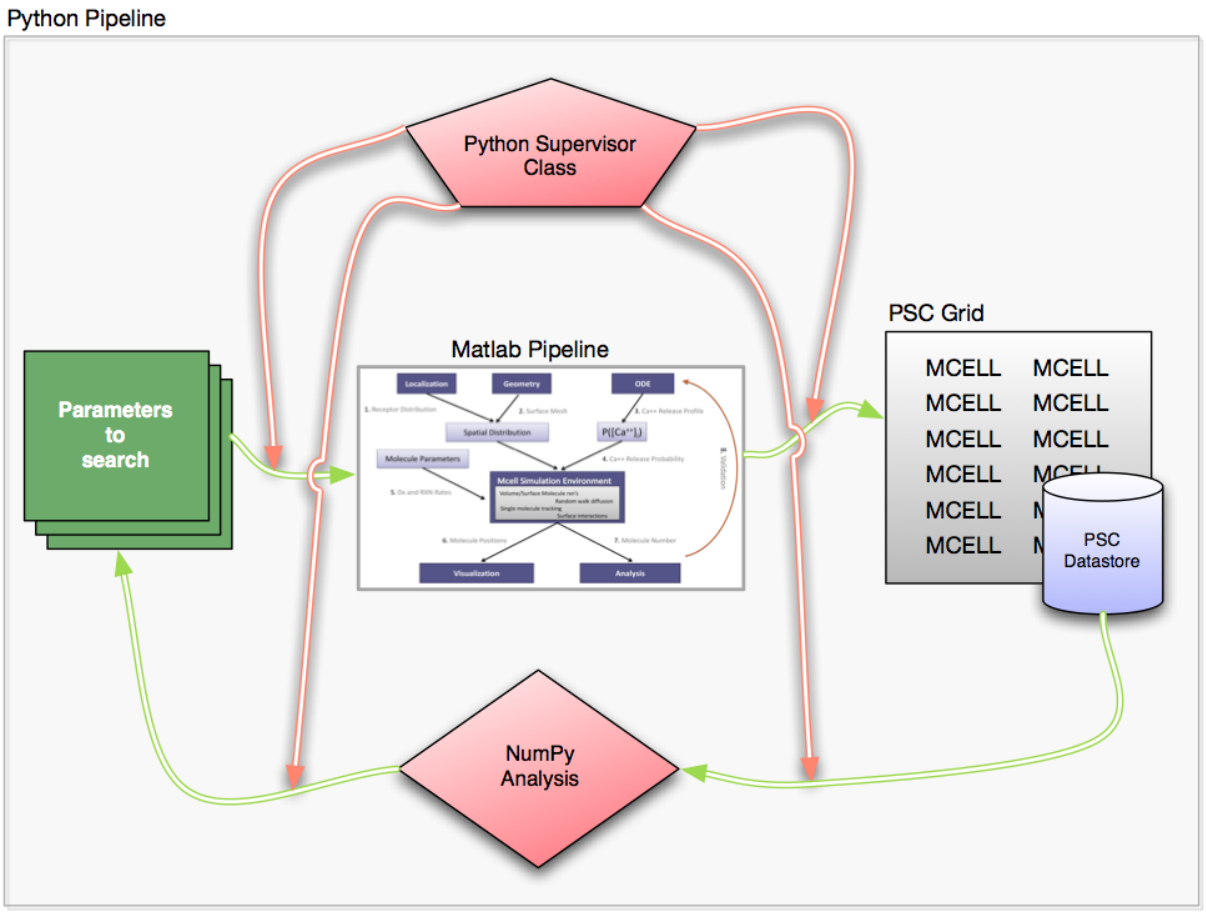

Figure A6: **Future analysis pipeline.** A code rewrite was performed to convert the previous Matlab control code to python. By doing so, it was possible to incorporate dynamic MCELL code generation, distribution to a computational grid, and post-hoc statistical analysis into a single automated code platform.

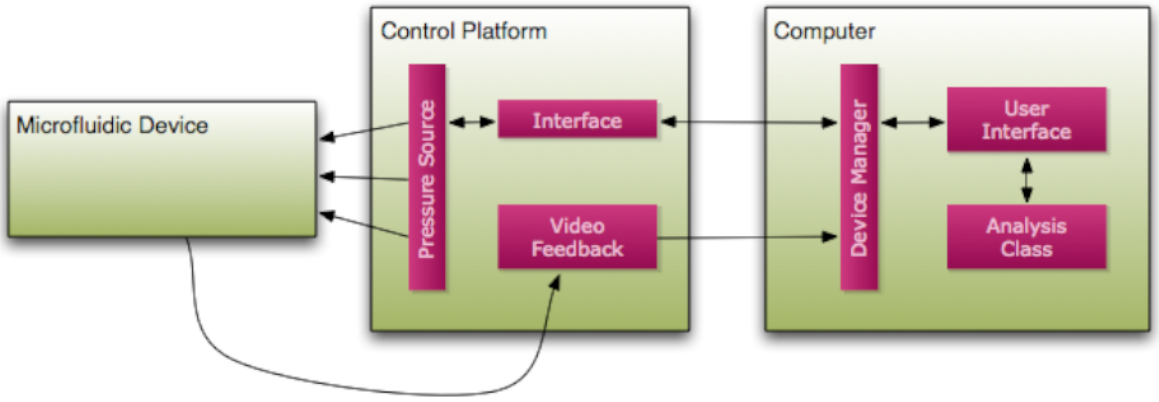

Figure A7: **Hardware overview.** The control platform interacts directly with the microfluidic device using high, low, and dynamic pressure sources. Feedback containing current pressure is passed to a data acquisition source within the platform. Additional video feedback is captured with a firewire camera. Both video and pressure feedback and then transferred independently to a computer running custom software. The data is then passed the user interface where further analysis can be performed. Closed-loop control is available through automated image analysis of the video source prior to delegating instructions back to the pressure controller.

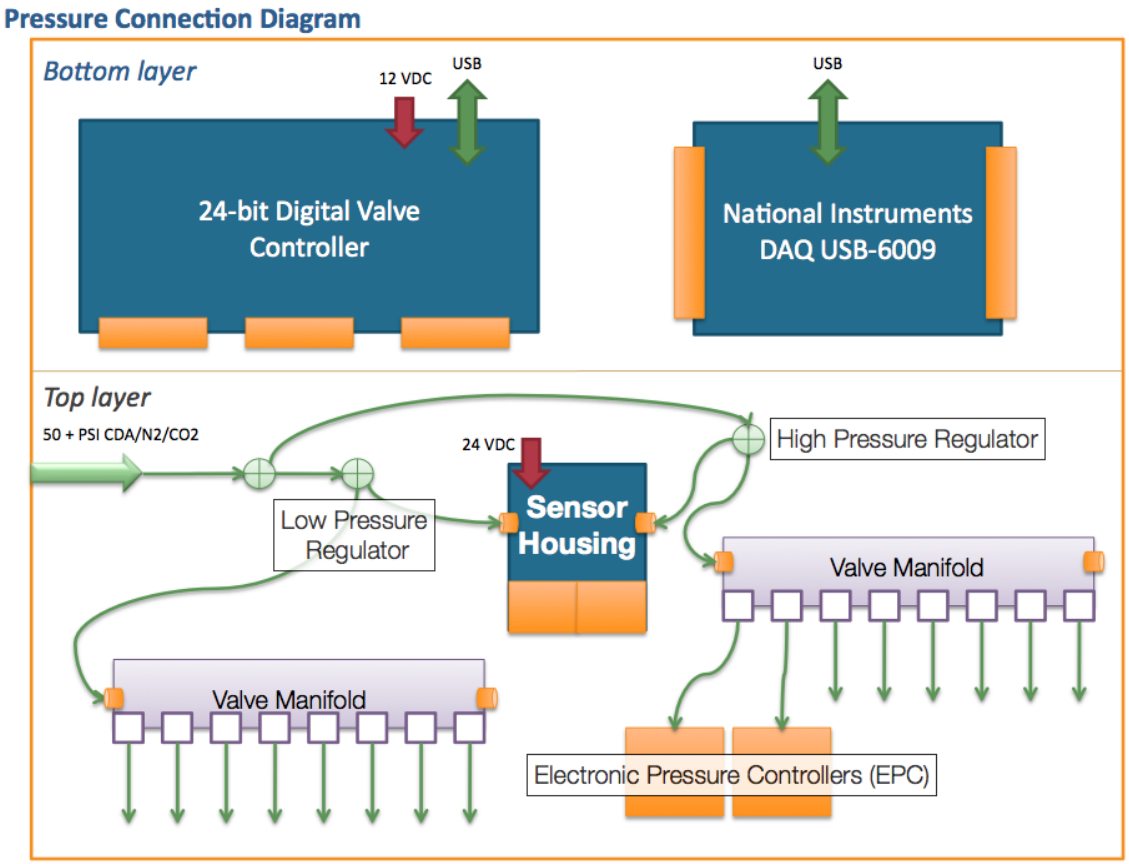

Figure A8: **Pressure Routing.** The platform is based on the original 24-valve Quake controller [103]. A second layer of control hardware consisting of piezoelectric differential pressure sensors and electronic pressure controllers was added to provide for a total of eight low-pressure (8 PSI), six high-pressure (35 PSI), and two dynamic-pressure (0-30 PSI) sources. Hardware control and feedback is provided to a windows-based PC running custom software via USB interface.

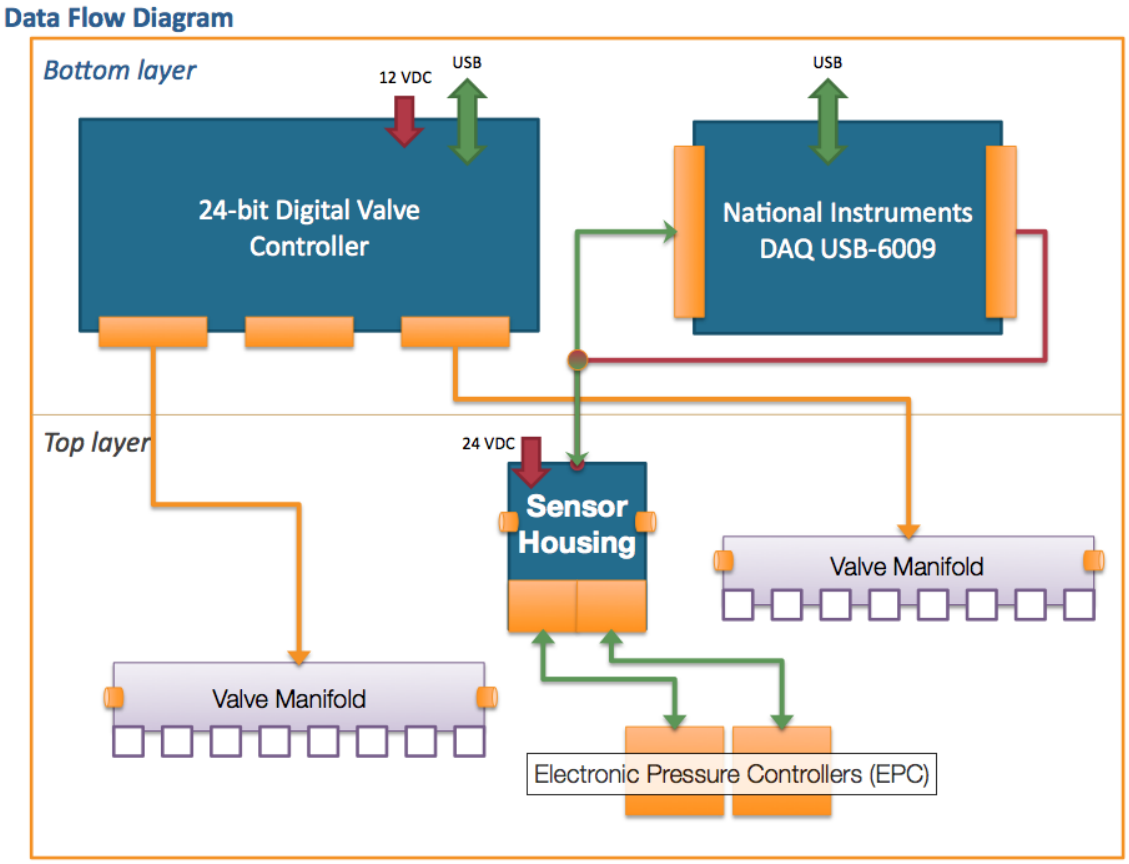

Figure A9: **Pressure Source Control and Feedback.** Signal input and output are routed through virtual com ports and USB connectivity. A conventional power source is supplied and stepped down to 5 volts for the custom PCB needed to interface with the integrated pressure sensors.

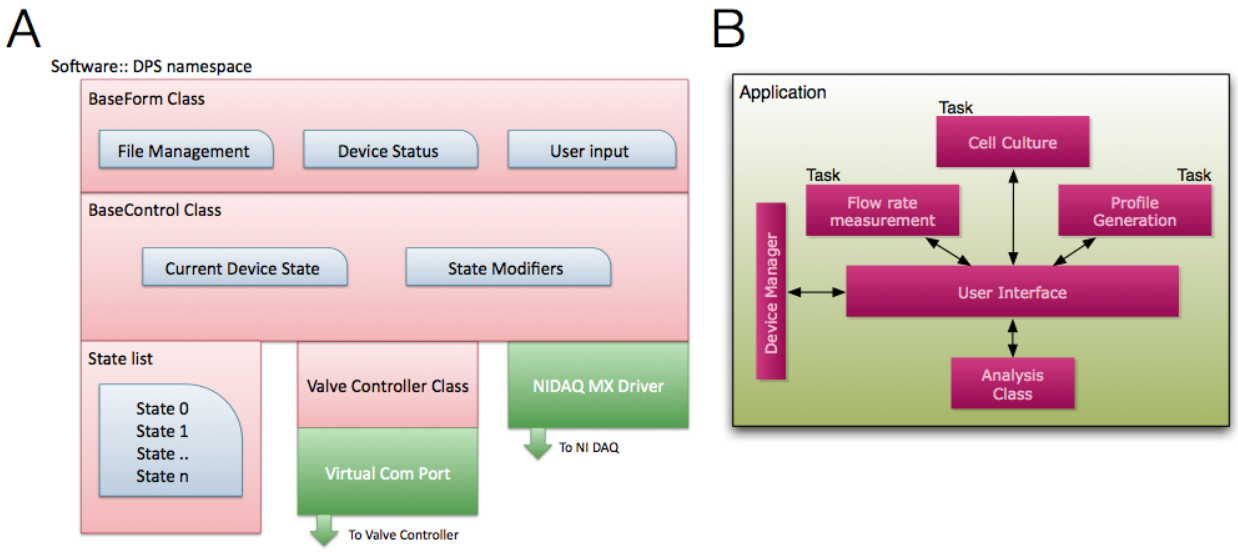

Figure A10: **Valve and Pressure Control Classes.** High-level overview of the software configuration.

BIBLIOGRAPHY

[1] Javier Atencia and David J Beebe. Controlled microfluidic interfaces. *Nature*, 437(7059):648–655, Sep 2005.

[2] D. H. Ballard. Generalizing the hough transform to detect arbitrary shapes. *Pattern recognition*, 13(2):111–122, 1981.

[3] G. Banker and K. Goslin. *Culturing nerve cells*. The MIT Press, 1998.

[4] A. Barria and R. Malinow. Nmda receptor subunit composition controls synaptic plasticity by regulating binding to camkii. *Neuron*, 48(2):289–301, 2005.

[5] MF Bear and RC Malenka. Synaptic plasticity: LTP and LTD. *Current Opinion in Neurobiology*, 4(3):389, 1994.

[6] S. Berberich, P. Punnakkal, V. Jensen, V. Pawlak, P.H. Seeburg, O. Hvalby, and G. Kohr. Lack of nmda receptor subtype selectivity for hippocampal long-term potentiation. *Journal of Neuroscience*, 25(29):6907, 2005.

[7] US Bhalla. Emergent properties of networks of biological signaling pathways. *Science*, 283(5400):381–7, 1999.

[8] B. Bhushan. *Springer handbook of nanotechnology*. Springer Verlag, 2006.

[9] G Bi and M Poo. Distributed synaptic modification in neural networks induced by patterned stimulation. *Nature*, 401(6755):792–796, Oct 1999.

[10] G Q Bi and M M Poo. Synaptic modifications in cultured hippocampal neurons: dependence on spike timing, synaptic strength, and postsynaptic cell type. *J Neurosci*, 18(24):10464–10472, Dec 1998.

[11] T.V.P. Bliss, G.L. Collingridge, et al. A synaptic model of memory: long-term potentiation in the hippocampus. *Nature*, 361(6407):31–39, 1993.

[12] T.V.P. Bliss, GL Collingridge, and R.G.M. Morris. *Long-term potentiation: enhancing neuroscience for 30 years*. Oxford University Press, USA, 2004.

[13] TVP Bliss and T. Lomo. Long-lasting potentiation of synaptic transmission in the dentate area of the anaesthetized rabbit following stimulation of the perforant path. *The Journal of physiology*, 232(2):331, 1973.

[14] H. Casanova, T.M. Bartol Jr, J. Stiles, and F. Berman. Distributing mcell simulations on the grid. *International Journal of High Performance Computing Applications*, 15(3):243, 2001.

[15] H. Casanova, F. Berman, T. Bartol, E. Gokcay, T. Sejnowski, A. Birnbaum, J. Dongarra, M. Miller, M. Ellisman, M. Faerman, et al. The virtual instrument: Support for grid-enabled mcell simulations. *International Journal of High Performance Computing Applications*, 18(1):3, 2004.

[16] Mark G Coulthard, Shannon Duffy, Michelle Down, Betty Evans, Maryanne Power, Fiona Smith, Con Stylianou, Sabine Kleikamp, Andrew Oates, Martin Lackmann, Gordon F Burns, and Andrew W Boyd. The role of the eph-ephrin signalling system in the regulation of developmental patterning. *Int J Dev Biol*, 46(4):375–384, 2002.

[17] J. Czech, M. Dittrich, and J.R. Stiles. Rapid creation, monte carlo simulation, and visualization of realistic 3d cell models. *Methods in molecular biology (Clifton, NJ)*, 500:237, 2009.

[18] Matthew B Dalva, Andrew C McClelland, and Matthew S Kayser. Cell adhesion molecules: signalling functions at the synapse. *Nat Rev Neurosci*, 8(3):206–220, Mar 2007.

[19] Pierre-Gilles de Gennes, Françoise Brochard-Wyart, David Quéré, and Axel Reisinger. *Capillarity and wetting phenomena: drops, bubbles, pearls, wavesâĂŐ*. Springer, Jan 2004.

[20] Stephan K W Dertinger, Xingyu Jiang, Zhiying Li, Venkatesh N Murthy, and George M Whitesides. Gradients of substrate-bound laminin orient axonal specification of neurons. *Proc Natl Acad Sci U S A*, 99(20):12542–12547, Oct 2002.

[21] Barry J Dickson. Molecular mechanisms of axon guidance. *Science*, 298(5600):1959–1964, Dec 2002.

[22] Nicole M. Dingle and Michael T. Harris. A robust algorithm for the simultaneous parameter estimation of interfacial tension and contact angle from sessile drop profiles. *Journal of Colloid and Interface Science*, 286(2):670–680, 2005.

[23] Petra S Dittrich and Andreas Manz. Lab-on-a-chip: microfluidics in drug discovery. *Nat Rev Drug Discov*, 5(3):210–218, Mar 2006.

[24] K. Erreger, S.M. Dravid, T.G. Banke, D.J. Wyllie, and S.F. Traynelis. Subunit-specific gating controls rat NR1/NR2A and NR1/NR2B NMDA channel kinetics and synaptic signalling profiles. *The Journal of physiology*, 563(2):345, 2005.

[25] T Esch, V Lemmon, and G Banker. Local presentation of substrate molecules directs axon specification by cultured hippocampal neurons. *J Neurosci*, 19(15):6417–6426, Aug 1999.

[26] Kevin M Franks, Thomas M Jr Bartol, and Terrence J Sejnowski. A Monte Carlo model reveals independent signaling at central glutamatergic synapses. *Biophys J*, 83(5):2333–2348, Nov 2002.

[27] K.M. Franks, T.M. Bartol, and T.J. Sejnowski. An MCell model of calcium dynamics and frequency-dependence of calmodulin activation in dendritic spines. *Neurocomputing*, 38(40):9–16, 2001.

[28] K.M. Franks and T.J. Sejnowski. Complexity of calcium signaling in synaptic spines. *Bioessays*, 24(12):1130–1144, 2002.

[29] K.M. Franks, C.F. Stevens, and T.J. Sejnowski. Independent sources of quantal variability at single glutamatergic synapses. *Journal of Neuroscience*, 23(8):3186, 2003.

[30] R.C. Froemke, M. Poo, and Y. Dan. Spike-timing-dependent synaptic plasticity depends on dendritic location. *Nature*, 434(7030):221–225, 2005.

[31] Bi G-Q. Spatiotemporal specificity of synaptic plasticity: cellular rules and mechanisms. *Biol. Cybern.*, 87:319–332, 2002.

[32] R.C. Gerkin, G.Q. Bi, and J.E. Rubin. A phenomenological calcium-based model of stdp. *Hippocampal Microcircuits*, pages 571–591, 2010.

[33] Richard C Gerkin, Pak-Ming Lau, David W Nauen, Yu Tian Wang, and Guo-Qiang Bi. Modular competition driven by nmda receptor subtypes in spike-timing-dependent plasticity. *J Neurophysiol*, 97(4):2851–2862, Apr 2007.

[34] M. Graupner and N. Brunel. Stdp in a bistable synapse model based on camkii and associated signaling pathways. *PLoS Comput Biol*, 3(11):e221, 2007.

[35] Michael Graupner and Nicolas Brunel. Mechanisms of induction and maintenance of spike-timing dependent plasticity in biophysical synapse models. *Frontiers in Neuroscience*, 2010.

[36] Pamela G Gross, Emil P Kartalov, Axel Scherer, and Leslie P Weiner. Applications of microfluidics for neuronal studies. *J Neurol Sci*, 252(2):135–143, Jan 2007.

[37] Michael J Hansen, Gerard E Dallal, and John G Flanagan. Retinal axon response to ephrin-as shows a graded, concentration-dependent transition from growth promotion to inhibition. *Neuron*, 42(5):717–730, Jun 2004.

[38] D.O. Hebb. The organization of behavior. new york. *Wiley. Hilgard, ER, & Marquis, DG (1940). Conditioning and learning. New\ brk: Appleton-Century-Crofts. Hoyle, G.(1979). Instrumental conditioning of the leg lift in the locust. Neuroscience Research Program Bulletin*, 17:577–586, 1949.

[39] W.R. Holmes. Models of calmodulin trapping and CaM kinase II activation in a dendritic spine. *Journal of Computational Neuroscience*, 8(1):65–86, 2000.

[40] M. Hoorfar and A. W. Neumann. Recent progress in axisymmetric drop shape analysis (adsa). *Advances in Colloid and Interface Science*, 121(1-3):25–49, 2006.

[41] V H Hopker, D Shewan, M Tessier-Lavigne, M Poo, and C Holt. Growth-cone attraction to netrin-1 is converted to repulsion by laminin-1. *Nature*, 401(6748):69–73, Sep 1999.

[42] Jacques Huot. Ephrin signaling in axon guidance. *Prog Neuropsychopharmacol Biol Psychiatry*, 28(5):813–818, Aug 2004.

[43] M. Hutzler, A. Lambacher, B. Eversmann, M. Jenkner, R. Thewes, and P. Fromherz. High-resolution multitransistor array recording of electrical field potentials in cultured brain slices. *Journal of neurophysiology*, 96(3):1638, 2006.

[44] Daniel Irimia, Dan A Geba, and Mehmet Toner. Universal microfluidic gradient generator. *Anal Chem*, 78(10):3472–3477, May 2006.

[45] A. Ivanov, C. Pellegrino, S. Rama, I. Dumalska, Y. Salyha, Y. Ben-Ari, and I. Medina. Opposing role of synaptic and extrasynaptic nmda receptors in regulation of the extracellular signal-regulated kinases (erk) activity in cultured rat hippocampal neurons. *The Journal of Physiology*, 572(3):789, 2006.

[46] E.M. Izhikevich. Simple model of spiking neurons. *IEEE Transactions on neural networks*, 14(6):1569–1572, 2003.

[47] Lisman J, Schulman H, and Cline H. The molecular basis of CaMKII function in synaptic and behavioural memory. *Nat. Rev. Neurosci.*, 3:175–190, 2002.

[48] C Joanne Wang, Xiong Li, Benjamin Lin, Sangwoo Shim, Guo-Li Ming, and Andre Levchenko. A microfluidics-based turning assay reveals complex growth cone responses to integrated gradients of substrate-bound ecm molecules and diffusible guidance cues. *Lab Chip*, 8(2):227–237, Feb 2008.

[49] E.R. Kandel, J.H. Schwartz, and T.M. Jessell. *Principles of neural science*. McGraw-Hill/Appleton & Lange, 2000.

[50] Thomas M Keenan and Albert Folch. Biomolecular gradients in cell culture systems. *Lab Chip*, 8(1):34–57, Jan 2008.

[51] D.X. Keller, K.M. Franks, T.M. Bartol Jr, and T.J. Sejnowski. Calmodulin activation by calcium transients in the postsynaptic density of dendritic spines. *PLoS ONE*, 3(4), 2008.

[52] Lily Kim, Yi-Chin Toh, Joel Voldman, and Hanry Yu. A practical guide to microfluidic perfusion culture of adherent mammalian cells. *Lab Chip*, 7(6):681–694, Jun 2007.

[53] M.J. Kim, A.W. Dunah, Y.T. Wang, and M. Sheng. Differential roles of nr2a-and nr2b-containing nmda receptors in ras-erk signaling and ampa receptor trafficking. *Neuron*, 46(5):745–760, 2005.

[54] Natanel Korin, Avishay Bransky, Maria Khoury, Uri Dinnar, and Shulamit Levenberg. Design of well and groove microchannel bioreactors for cell culture. *Biotechnol Bioeng*, 102(4):1222–1230, Mar 2009.

[55] G. Krapivinsky, L. Krapivinsky, Y. Manasian, A. Ivanov, R. Tyzio, C. Pellegrino, Y. Ben-Ari, D.E. Clapham, and I. Medina. The nmda receptor is coupled to the erk pathway by a direct interaction between nr2b and rasgrf1. *Neuron*, 40(4):775–784, 2003.

[56] Tobias Kraus, Elisabeth Verpoorte, Vincent Linder, Wendy Franks, Andreas Hierlemann, Flavio Heer, Sadik Hafizovic, Teruo Fujii, Nico F de Rooij, and Sander Koster. Characterization of a microfluidic dispensing system for localised stimulation of cellular networks. *Lab Chip*, 6(2):218–229, Feb 2006.

[57] Brandon Kuczenski, Philip R LeDuc, and William C Messner. Pressure-driven spatiotemporal control of the laminar flow interface in a microfluidic network. *Lab Chip*, 7(5):647–649, May 2007.

[58] Brandon Kuczenski, Warren C Ruder, William C Messner, and Philip R Leduc. Probing cellular dynamics with a chemical signal generator. *PLoS One*, 4(3):e4847, 2009.

[59] E.W. Lam, G.A. Cooksey, B.A. Finlayson, and A. Folch. Microfluidic circuits with tunable flow resistances. *Applied Physics Letters*, 89:164105, 2006.

[60] Grace N Li, Jeffrey Liu, and Diane Hoffman-Kim. Multi-molecular gradients of permissive and inhibitory cues direct neurite outgrowth. *Ann Biomed Eng*, 36(6):889–904, Jun 2008.

[61] J. Lisman. A mechanism for the hebb and the anti-hebb processes underlying learning and memory. *Proceedings of the National Academy of Sciences*, 86(23):9574, 1989.

[62] J E Lisman. Three ca2+ levels affect plasticity differently: the ltp zone, the ltd zone and no man's land. *J Physiol*, 532(Pt 2):285, Apr 2001.

[63] J.E. Lisman and A.M. Zhabotinsky. A model of synaptic memory a camkii/pp1 switch that potentiates transmission by organizing an ampa receptor anchoring assembly. *Neuron*, 31(2):191–201, 2001.

[64] L. Liu, T.P. Wong, M.F. Pozza, K. Lingenhoehl, Y. Wang, M. Sheng, Y.P. Auberson, and Y.T. Wang. Role of nmda receptor subtypes in governing the direction of hippocampal synaptic plasticity. *Science*, 304(5673):1021, 2004.

[65] B. Ludascher, I. Altintas, C. Berkley, D. Higgins, E. Jaeger, M. Jones, E.A. Lee, J. Tao, and Y. Zhao. Scientific workflow management and the Kepler system. *Concurrency and Computation*, 18(10):1039, 2006.

[66] Sheng M and Sala C. PDZ domains and the organization of supramolecular complexes. *Annu. Rev. Neurosci.*, 24:1–29, 2001.

[67] Junyu Mai, Lee Fok, Hongfeng Gao, Xiang Zhang, and Mu-Ming Poo. Axon initiation and growth cone turning on bound protein gradients. *J Neurosci*, 29(23):7450–7458, Jun 2009.

[68] Robert C Malenka and Mark F Bear. Ltp and ltd: an embarrassment of riches. *Neuron*, 44(1):5–21, Sep 2004.

[69] H Markram, J Lubke, M Frotscher, and B Sakmann. Regulation of synaptic efficacy by coincidence of postsynaptic aps and epsps. *Science*, 275(5297):213–215, Jan 1997.

[70] P.V. Massey, B.E. Johnson, P.R. Moult, Y.P. Auberson, M.W. Brown, E. Molnar, G.L. Collingridge, and Z.I. Bashir. Differential roles of nr2a and nr2b-containing nmda receptors in cortical long-term potentiation and long-term depression. *Journal of Neuroscience*, 24(36):7821, 2004.

[71] I. Meyvantsson and D. J. Beebe. Cell culture models in microfluidic systems. *Annual Review of Analytical Chemistry*, 2008.

[72] L.J. Millet, M.E. Stewart, J.V. Sweedler, R.G. Nuzzo, and M.U. Gillette. Microfluidic devices for culturing primary mammalian neurons at low densities. *Lab on a Chip*, 7(8):987–994, 2007.

[73] S.D. Minteer. *Microfluidic techniques: reviews and protocols*. Humana Pr Inc, 2006.

[74] W. Morishita, W. Lu, G.B. Smith, R.A. Nicoll, M.F. Bear, and R.C. Malenka. Activation of nr2b-containing nmda receptors is not required for nmda receptor-dependent long-term depression. *Neuropharmacology*, 52(1):71–76, 2007.

[75] N. A. Mortensen, F. Okkels, and H. Bruus. Reexamination of hagen-poiseuille flow: Shape dependence of the hydraulic resistance in microchannels. *Physical Review E*, 71(5):57301, 2005.

[76] H. Naoki, Y. Sakumura, and S. Ishii. Local signaling with molecular diffusion as a decoder of ca++ signals in synaptic plasticity. *Molecular Systems Biology*, 1(1), 2005.

[77] T. Nevian and B. Sakmann. Spine ca2+ signaling in spike-timing-dependent plasticity. *Journal of Neuroscience*, 26(43):11001, 2006.

[78] Thomas Nevian and Bert Sakmann. Single spine Ca2+ signals evoked by coincident epsps and backpropagating action potentials in spiny stellate cells of layer 4 in the juvenile rat somatosensory barrel cortex. *J Neurosci*, 24(7):1689–1699, Feb 2004.

[79] E.A. Nimchinsky, B.L. Sabatini, and K. Svoboda. Structure and function of dendritic spines. *Annual review of physiology*, 64(1):313–353, 2002.

[80] Nicole K Noren and Elena B Pasquale. Eph receptor-ephrin bidirectional signals that target ras and rho proteins. *Cell Signal*, 16(6):655–666, Jun 2004.

[81] Anthony A Jr Oliva, Conrad D James, Caroline E Kingman, Harold G Craighead, and Gary A Banker. Patterning axonal guidance molecules using a novel strategy for microcontact printing. *Neurochem Res*, 28(11):1639–1648, Nov 2003.

[82] P.M. Papadopoulos, M.J. Katz, and G. Bruno. Npaci rocks: Tools and techniques for easily deploying manageable linux clusters. *Concurrency and Computation: Practice & Experience*, 15(7):707–725, 2003.

[83] Jeong Won Park, Behrad Vahidi, Anne M Taylor, Seog Woo Rhee, and Noo Li Jeon. Microfluidic culture platform for neuroscience research. *Nat Protoc*, 1(4):2128–2136, 2006.

[84] Y.F. Peng, Y.H. Shiau, and R.R. Hwang. Transition in a 2-D lid-driven cavity flow. *Computers and Fluids*, 32(3):337–352, 2003.

[85] R. Penrose and P. Marcer. Quantum computation, entanglement and state reduction [and discussion]. *Philosophical Transactions: Mathematical, Physical and Engineering Sciences*, 356(1743):1927–1939, 1998.

[86] J.D. Petersen, X. Chen, L. Vinade, A. Dosemeci, J.E. Lisman, and T.S. Reese. Distribution of postsynaptic density (psd)-95 and ca2+/calmodulin-dependent protein kinase ii at the psd. *Journal of Neuroscience*, 23(35):11270, 2003.

[87] D. Plenz and T.C. Thiagarajan. The organizing principles of neuronal avalanches: cell assemblies in the cortex? *Trends in Neurosciences*, 30(3):101–110, 2007.

[88] Jonathan E Rubin, Richard C Gerkin, Guo-Qiang Bi, and Carson C Chow. Calcium time course as a signal for spike-timing-dependent plasticity. *J Neurophysiol*, 93(5):2600–2613, May 2005.

[89] NF Rulkov, I. Timofeev, and M. Bazhenov. Oscillations in large-scale cortical networks: map-based model. *Journal of Computational Neuroscience*, 17(2):203–223, 2004.

[90] J. G. Santiago, S. T. Wereley, C. D. Meinhart, D. J. Beebe, and R. J. Adrian. A particle image velocimetry system for microfluidics. *Experiments in Fluids*, 25(4):316–319, 1998.

[91] D.M. Santucci and S. Raghavachari. The effects of NR2 subunit-dependent NMDA receptor kinetics on synaptic transmission and CaMKII activation. *PLoS Computational Biology*, 4(10), 2008.

[92] Kendra V. Sharp. Experimental investigation of liquid and particle-laden flows in microtubes. Master's thesis, University of Illinois at Urbana Champaign, 2001.

[93] H.Z. Shouval, M.F. Bear, and L.N. Cooper. A unified model of nmda receptor-dependent bidirectional synaptic plasticity. *Proceedings of the National Academy of Sciences of the United States of America*, 99(16):10831, 2002.

[94] A. Sobczyk, V. Scheuss, and K. Svoboda. Nmda receptor subunit-dependent [ca2+] signaling in individual hippocampal dendritic spines. *Journal of Neuroscience*, 25(26):6037, 2005.

[95] T.M. Squires and S.R. Quake. Microfluidics: Fluid physics at the nanoliter scale. *Reviews of modern physics*, 77(3):977–1026, 2005.

[96] P. Tabeling and S. Cheng. *Introduction to microfluidics*. Oxford University Press, USA, 2005.

[97] Shuichi Takayama, Emanuele Ostuni, Philip LeDuc, Keiji Naruse, Donald E Ingber, and George M Whitesides. Selective chemical treatment of cellular microdomains using multiple laminar streams. *Chem Biol*, 10(2):123–130, Feb 2003.

[98] C.G. Thomas, A.J. Miller, and G.L. Westbrook. Synaptic and extrasynaptic nmda receptor nr2 subunits in cultured hippocampal neurons. *Journal of neurophysiology*, 95(3):1727, 2006.

[99] Todd Thorsen, Sebastian J Maerkl, and Stephen R Quake. Microfluidic large-scale integration. *Science*, 298(5593):580–584, Oct 2002.

[100] Anna Tourovskaia, Xavier Figueroa-Masot, and Albert Folch. Long-term micropatterned cell cultures in heterogeneous microfluidic environments. *Conf Proc IEEE Eng Med Biol Soc*, 4:2675–2678, 2004.

[101] Anna Tourovskaia, Xavier Figueroa-Masot, and Albert Folch. Differentiation-on-a-chip: a microfluidic platform for long-term cell culture studies. *Lab Chip*, 5(1):14–19, Jan 2005.

[102] Anna Tourovskaia, Xavier Figueroa-Masot, and Albert Folch. Long-term microfluidic cultures of myotube microarrays for high-throughput focal stimulation. *Nat Protoc*, 1(3):1092–1104, 2006.

[103] M A Unger, H P Chou, T Thorsen, A Scherer, and S R Quake. Monolithic microfabricated valves and pumps by multilayer soft lithography. *Science*, 288(5463):113–116, Apr 2000.

[104] H. Urakubo, M. Honda, R.C. Froemke, and S. Kuroda. Requirement of an allosteric kinetics of NMDA receptors for spike timing-dependent plasticity. *Journal of Neuroscience*, 28(13):3310, 2008.

[105] N S Veselovsky, F Engert, and H D Lux. Fast local superfusion technique. *Pflugers Arch*, 432(2):351–354, Jun 1996.

[106] Vladislav Volman, Richard C Gerkin, Pak-Ming Lau, Eshel Ben-Jacob, and Guo-Qiang Bi. Calcium and synaptic dynamics underlying reverberatory activity in neuronal networks. *Phys Biol*, 4(2):91–103, Jun 2007.

[107] D.A. Wagenaar, Z. Nadasdy, and S.M. Potter. Persistent dynamic attractors in activity patterns of cultured neuronal networks. *Physical Review E*, 73(5):51907, 2006.

[108] G. M. Walker, H. C. Zeringue, and D. J. Beebe. Microenvironment design considerations for cellular scale studies. *Lab Chip*, 4(2):91–7, Apr 2004.

[109] Fen Wang, Hao Wang, Jun Wang, Hsiang-Yu Wang, Peter L Rummel, Suresh V Garimella, and Chang Lu. Microfluidic delivery of small molecules into mammalian cells based on hydrodynamic focusing. *Biotechnol Bioeng*, 100(1):150–158, May 2008.

[110] H.X. Wang, R.C. Gerkin, D.W. Nauen, and G.Q. Bi. Coactivation and timing-dependent integration of synaptic potentiation and depression. *Nature neuroscience*, 8(2):187–193, 2005.

[111] Douglas B Weibel, Piotr Garstecki, and George M Whitesides. Combining microscience and neurobiology. *Curr Opin Neurobiol*, 15(5):560–567, Oct 2005.

[112] C. Weitlauf, Y. Honse, Y.P. Auberson, M. Mishina, D.M. Lovinger, and D.G. Winder. Activation of nr2a-containing nmda receptors is not obligatory for nmda receptor-dependent long-term potentiation. *Journal of Neuroscience*, 25(37):8386, 2005.

[113] Takeshi Yoshimura, Nariko Arimura, and Kozo Kaibuchi. Signaling networks in neuronal polarization. *J Neurosci*, 26(42):10626–10630, Oct 2006.

[114] H. Yu, M. Leeser, G. Tadmor, and S. Siegel. Real-time particle image velocimetry for feedback loops using fpga implementation. *Journal of Aerospace Computing, Information, and Communication 2006*, 2:52–62, 2006.

[115] Hongmei Yu, Caroline M Alexander, and David J Beebe. Understanding microchannel culture: parameters involved in soluble factor signaling. *Lab Chip*, 7(6):726–730, Jun 2007.

[116] Huan-Chang Zeng, Yi-Cheng Ho, Shih-Ta Chen, Huei-In Wu, Hsi-Wen Tung, Wei-Leun Fang, and Yen-Chung Chang. Studying the formation of large cell aggregates in patterned neuronal cultures. *J Neurosci Methods*, 165(1):72–82, Sep 2007.

[117] J. Zhao, Y. Peng, Z. Xu, R. Chen, Q. Gu, Z. Chen, and W. Lu. Synaptic metaplasticity through NMDA receptor lateral diffusion. *Journal of Neuroscience*, 28(12):3060, 2008.